Nonlinear topological edge states, topological gap solitons, and self-induced topological edge states in nonlinear Su-Schrieffer-Heeger circuit lattices

Rujiang Li,[1,*] Wencai Wang,[1] Xiangyu Kong,[1] Ce Shang,[2] Yongtao Jia,[1] Gui-Geng Liu,[3,4,†] Huibin Tao,[5] Ying Liu,[1] and Baile Zhang[6,7,‡]

[1]*National Key Laboratory of Radar Detection and Sensing, School of Electronic Engineering, Xidian University, Xi'an 710071, China*

[2]*Aerospace Information Research Institute, Chinese Academy of Sciences, Beijing 100094, China*

[3]*Research Center for Industries of the Future, Westlake University, Hangzhou 310030, China*

[4]*Department of Electronic and Information Engineering, School of Engineering, Westlake University, Hangzhou 310030, China*

[5]*School of Microelectronics, Xi'an Jiaotong University, Xi'an 710049, China*

[6]*Division of Physics and Applied Physics, School of Physical and Mathematical Sciences, Nanyang Technological University, 21 Nanyang Link, Singapore 637371, Singapore*

[7]*Centre for Disruptive Photonic Technologies, The Photonics Institute, Nanyang Technological University, 50 Nanyang Avenue, Singapore 639798, Singapore*

(Received 6 May 2025; revised 20 April 2026; accepted 28 May 2026; published 11 June 2026)

Topological edge states typically arise at the boundaries of topologically nontrivial structures or at interfaces between regions with different topological invariants. When topological systems are extended into the nonlinear regime, linear topological edge states bifurcate into nonlinear counterparts, and topological gap solitons emerge in the bulk of the structures. Extensive studies of nonlinear topological edge states and topological gap solitons have been carried out. Following recent experimental observations in photonic systems, we leverage the strong and tunable nonlinearity of electric circuits and systematically investigate the localized states in nonlinear Su-Schrieffer-Heeger circuit lattices. Besides revisiting the nonlinear topological edge states and topological gap solitons, we uncover a new type of self-induced topological edge states which exhibit the hallmark features of linear topological edge states, including sublattice polarization, phase jumps, and decaying tails that approach zero. A distinctive feature of these states is the boundary-induced power threshold for existence. Our work unveils new opportunities for exploring novel nonlinear topological states and paves the way for the development of nonlinear topological circuits.

DOI: 10.1103/s4d3-nlz6

I. INTRODUCTION

Topological insulators are physical structures that behave as conventional insulators in the bulk, but conducting on their surfaces due to the existence of topologically protected edge states [1–3]. The realization of topological insulators has been demonstrated in diverse physical platforms, and the immunity of topological edge states to local deformations and disorders are of great significance for the exciting potential applications [4–20]. Extending topological insulators into the nonlinear regime such as by considering the nonlinear response of optical materials under high field intensity [21,22], the interplay between topology and nonlinearity leads to the formation of the nonlinear topological edge states which bifurcate from the linear edge states and inherit topological protection from the linear counterparts [23–36]. In two-dimensional topological systems, due to the modulation instability, the nonlinear edge states develops into the edge solitons where dispersion is balanced with nonlinearity [23–25,37–43]. The bifurcation from the linear topological states to the nonlinear ones is also applicable to the nonlinear higher-order topological systems, where nonlinear topological corner states are proposed [33,44–46].

Topological gap solitons, which are self-localized topological states in the bulk with their spectra lie within the topological band gap, are also discovered in nonlinear topological systems [28,30,36,47–53]. Although the topological gap solitons have no direct linear counterparts, they exhibit the similar proprieties of the linear topological edge states, such as the sublattice polarization [30,48,50] and unidirectional transport [47,52]. In contrast to the conventional lattice solitons which are self-localized due to the balance between coupling (commonly referred as diffraction in photonic systems) and nonlinearity, and thus are topologically trivial [54–56], the topological gap solitons are localized at the nonlinearity-induced topological interfaces and their formation may be interpreted as the Jackiw-Rebbi Dirac boundary modes where mass inversion occurs across the interface [49,50,53].

Following the experimental observations of nonlinear topological edge states and topological gap solitons in photonic systems [30,57], this study investigates localized states in nonlinear Su-Schrieffer-Heeger (SSH) models with onsite nonlinearity using electric circuits [58]. Electric circuits are

*Contact author: rujiangli@xidian.edu.cn
†Contact author: liuguigeng@westlake.edu.cn
‡Contact author: blzhang@ntu.edu.sg

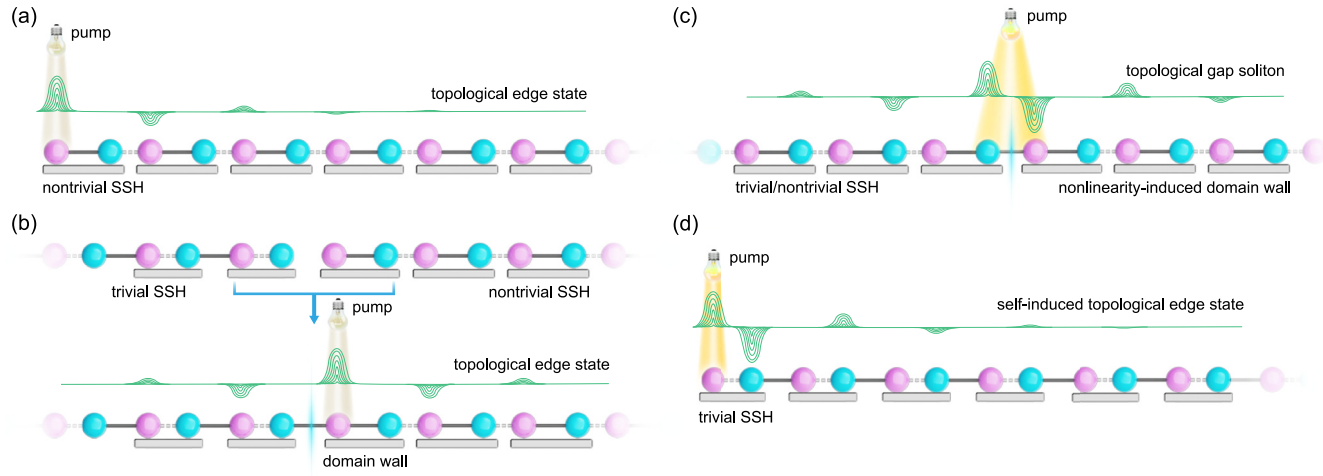

FIG. 1. Schematics of the nonlinear SSH lattices and the corresponding localized states. (a) A topologically nontrivial SSH lattice terminates with a weak bond. When the lattice is excited by a low-intensity pump, i.e., an external continuous source with a small signal, topological edge states appear at the left edge. (b) A structure connected by two SSH lattices with different topological properties. Due to the formation of the domain wall, topological edge state also appears under a low-intensity pump. With the increasing of pump intensity, the topological edge states in panels (a), (b) bifurcate to nonlinear ones. (c) For a topologically trivial or nontrivial SSH lattice, under the excitation from an external pump, a nonlinearity-induced domain wall appears in the bulk and supports the formation of topological gap solitons. (d) A topologically trivial SSH lattice ending with strong bond. Under the action of onsite nonlinearity, self-induced topological edge states appear at the physical termination.

particularly well-suited for probing nonlinear topological physics due to the flexibility in constructing circuit lattices and the capability of phase-resolved measurement techniques [59–64]. We systematically explore the nonlinear topological edge states and topological gap solitons in SSH circuit lattices, providing comprehensive verification of sublattice polarization and phase jumps, as well as observing the full existence curves and the nonlinearity-induced effects on state localization, whether weakening or strengthening it. Such thorough experimental validation is difficult to achieve in other platforms. Moreover, we uncover a novel type of self-induced topological edge states that reside at the edge of a topologically trivial lattice yet exhibit hallmark features of linear topological edge states, including sublattice polarization, phase jumps, and decaying tails approaching zero. A distinctive characteristic of these states is the existence of a boundary-induced power threshold. These self-induced topological edge states have not been reported previously. Our work unveils new opportunities for exploring novel nonlinear topological states. It also paves the way for the development of nonlinear topological circuits.

Our main findings are summarized in Fig. 1. As depicted in Fig. 1(a), under a low-intensity pump, i.e., under excitation from an external continuous source with a small signal, the system operates in the linear limit, and topological edge states appear at the edge of the topologically nontrivial SSH lattice that terminates with a weak bond. With the increasing of pump intensity, we observe the nonlinear topological edge states bifurcated from the linear counterpart. We experimentally validate the inherited properties of sublattice polarization and phase jump, and find that nonlinearity weakens the localization of the topological edge states. We then implement a structure by connecting two SSH lattices with different topological properties, as shown in Fig. 1(b). Due to the formation of the domain wall, under a weak pump topological edge state appears as well. We experimentally reveal the similar state properties under increased pump intensity, because the nonlinear topological edge states have the same physical origin.

Different to the nonlinear topological edge states, topological gap solitons have no direct linear counterparts. For an SSH lattice shown in Fig. 1(c), no matter the lattice is topologically trivial or nontrivial in the linear limit, under the external pump, a nonlinearity-induced domain wall appears in the bulk and supports the formation of topological gap solitons. We experimentally observe that the left and right tails of the topological gap solitons have opposite sublattice polarizations, and reveal that nonlinearity increases the localization of the topological gap solitons. These features are in contrast to those of nonlinear topological edge states because the physical origins are totally different.

Besides the nonlinear topological edge states and topological gap solitons, we discover both theoretically and experimentally a new type of topological states residing at the edge of a semi-infinite lattice ending with a strong bond [Fig. 1(d)]. Although the lattice is topologically trivial in the linear limit, under the action of onsite nonlinearity, it supports the self-induced topological edge states that reside at the physical termination of the structure [65]. These self-induced topological edge states exhibit sublattice polarization and phase jumps starting from the second site close to the edge. They are the variant of the topological gap solitons under the breaking of the discrete translational symmetry at the edge of the structure, along with a boundary-induced power threshold for their existence. Specifically, the self-induced topological edge states can be approximately mapped to the linear topological edge state of a semi-infinite SSH lattice. Unlike the previously reported self-induced topological transitions driven by nonlinear couplings [59], which are conceptually

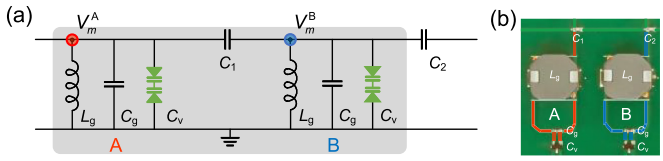

FIG. 2. Schematics of the nonlinear SSH circuit lattices. (a) Circuit implementation of the unit cell of the nonlinear SSH lattices. The back-to-back varactor diodes provides the onsite nonlinearity of the SSH model. (b) Unit cell of the experimentally realized nonlinear SSH circuit lattices.

straightforward but less common in realistic interacting systems, our self-induced topological edge states are realized in a lattice with onsite nonlinearity and feature decaying tails that approach zero, in contrast to the nonlocalized distributions that maintain nonzero plateau levels [59]. Our results are broadly applicable and can be readily extended to photonic and cold atomic systems, where onsite nonlinearities naturally arise from interparticle interactions.

This paper is organized as follows. In Sec. II, we construct a theoretical model based on the Kirchhoff circuit equations. Section III presents the experimental observation of the nonlinear topological edge states, accompanied by the theoretical discussion. In Sec. IV, we focus on the topological gap solitons. In Sec. V, we discuss the results for the newly discovered self-induced topological edge states. Section VI presents a discussion on the topological properties. Finally, Sec. VII is the conclusion.

II. MODEL

All the nonlinear SSH models shown in Fig. 1 can be realized using electric circuit lattices. Figure 2(a) shows the circuit implementation of a unit cell of the nonlinear SSH lattices, where A and B denote the two sublattice sites. For one sublattice, the inductor L_g, capacitor C_g, and back-to-back varactor diode C_v are wired in parallel. The varactor diode acts as a voltage-dependent variable capacitor with $C_v = C_L + C_{NL}$, where the linear part C_L is the capacitance at the zero voltage and the nonlinear part can be phenomenologically written as $C_{NL} = -C_L + \frac{C_L}{(1+|v/v_0|)^M}$ (see Appendix A for the modeling of back-to-back varactor diodes). Here, v_0 and M are constants, and v is the voltage amplitude. The sublattice sites are wired with each other through the intracell coupling capacitor C_1 and intercell coupling capacitor C_2.

For a typical nonlinear SSH circuit that emulates the lattice shown in Fig. 1(a), it can be described by the discretized Gross-Pitaevskii (GP) equation (also called as the discrete nonlinear Schrödinger equation):

$$\mathrm{i}\frac{d}{dt}\begin{bmatrix} V_m^A \\ V_m^B \end{bmatrix} = E_0\begin{bmatrix} V_m^A \\ V_m^B \end{bmatrix} + J_1\begin{bmatrix} V_m^B \\ V_m^A \end{bmatrix} + J_2\begin{bmatrix} V_{m-1}^B \\ V_{m+1}^A \end{bmatrix} + \begin{bmatrix} g(V_m^A)V_m^A \\ g(V_m^B)V_m^B \end{bmatrix}, \tag{1}$$

where $[V_m^A(t), V_m^B(t)]^T$ are the time-dependent voltages on sites A and B in the mth unit cell, $E_0 = \omega_0 + \Delta E$ is equivalent to the constant onsite energy, which includes the resonant frequency of the linear oscillators $\omega_0 = 1/\sqrt{L_g(C_g + C_L)}$ and the frequency shift induced by the coupling capacitors $\Delta E = -\frac{C_1+C_2}{2(C_g+C_L)}\omega_0$, $J_1 = \frac{C_1}{2(C_g+C_L)}\omega_0$ and $J_2 = \frac{C_2}{2(C_g+C_L)}\omega_0$ are the intracell and intercell coupling coefficients, respectively, and $g(V_m^\sigma) = -\frac{C_{NL}(V_m^\sigma)}{2(C_g+C_L)}\omega_0$ $(\sigma = A, B)$ is the voltage-dependent onsite energy. Equation (1) is valid under $C_{1,2} \ll C_g + C_L$ and $C_{NL} \ll C_g + C_L$, where the slowly varying envelope approximation holds (see Appendix B for the derivation from the Kirchhoff circuit equations). Thus, the nonlinear circuit lattice realizes the SSH model with onsite nonlinearity. The four lattice configurations shown in Fig. 1 all can be implemented based on the circuit dimer in Fig. 2(a). Figure 2(b) shows the unit cell of the experimentally realized circuit lattices.

The circuit parameters in the four nonlinear SSH circuits are $C_g = 4.7$ nF, $L_g = 15$ μH, $C_L = 73.48$ pF, $v_0 = 2.1935$, and $M = 0.4548$. For the first lattice shown in Fig. 1(a), the intracell and intercell coupling capacitors are $C_1 = 180$ pF and $C_2 = 560$ pF, respectively. For the second lattice shown in Fig. 1(b), the topologically nontrivial part has $C_1 = 180$ pF and $C_2 = 560$ pF, while the trivial part has $C_1 = 560$ pF and $C_2 = 180$ pF. An additional capacitance $C_2 - C_1$ is added to the grounding capacitance of the interface circuit node. For the third and fourth lattices shown in Figs. 1(c) and 1(d), the intracell and intercell coupling capacitors are $C_1 = 560$ pF and $C_2 = 180$ pF, respectively.

III. NONLINEAR TOPOLOGICAL EDGE STATES

We first study the nonlinear topological edge states in the first SSH lattice [Fig. 1(a)]. The configuration is a typical semi-infinite SSH lattice that ends with a weak bond. In the linear limit, due to the nontrivial topology with the winding number $\mathcal{W} = 1$, topological edge state residing at the left edge exists [58]. Under the action of the onsite nonlinearity, by bifurcating from the linear edge state, nonlinear topological edge states with the topological protection inherited from the linear counterpart appear (see Appendix C for the calculation algorithm and stability analysis of the nonlinear topological edge states). As depicted in Fig. 3(a), with the power increasing (defined as the sum of the squares of all the site voltages), the frequency of the nonlinear edge state exhibits a blue shift due to the decreased grounding capacitance, and the state localization becomes weak with a larger participation ratio defined as $(\sum_{m,\sigma}|v_m^\sigma|^2)^2/\sum_{m,\sigma}|v_m^\sigma|^4$ $(\sigma = A, B)$, particularly when the frequency enters the linear bulk band (denoted by the shaded gray areas). Here, the participation ratio is introduced to measure state localization, with a large participation ratio signifying weak localization. The inset of Fig. 3(a) shows a typical profile of the nonlinear topological edge states. Since the nonlinear edge states are bifurcated from the linear counterpart which satisfies $v_m^A = (-\frac{J_1}{J_2})^{|m|}v_0^A$ and $v_m^B = 0$, their voltages mainly distribute on sublattice site A with the sublattice pseudospin

$$S = \frac{\sum_m\left(|v_m^A|^2 - |v_m^B|^2\right)}{\sum_m\left(|v_m^A|^2 + |v_m^B|^2\right)} \tag{2}$$

nearly equal to 1 and the phase jump of π among the neighboring cells.

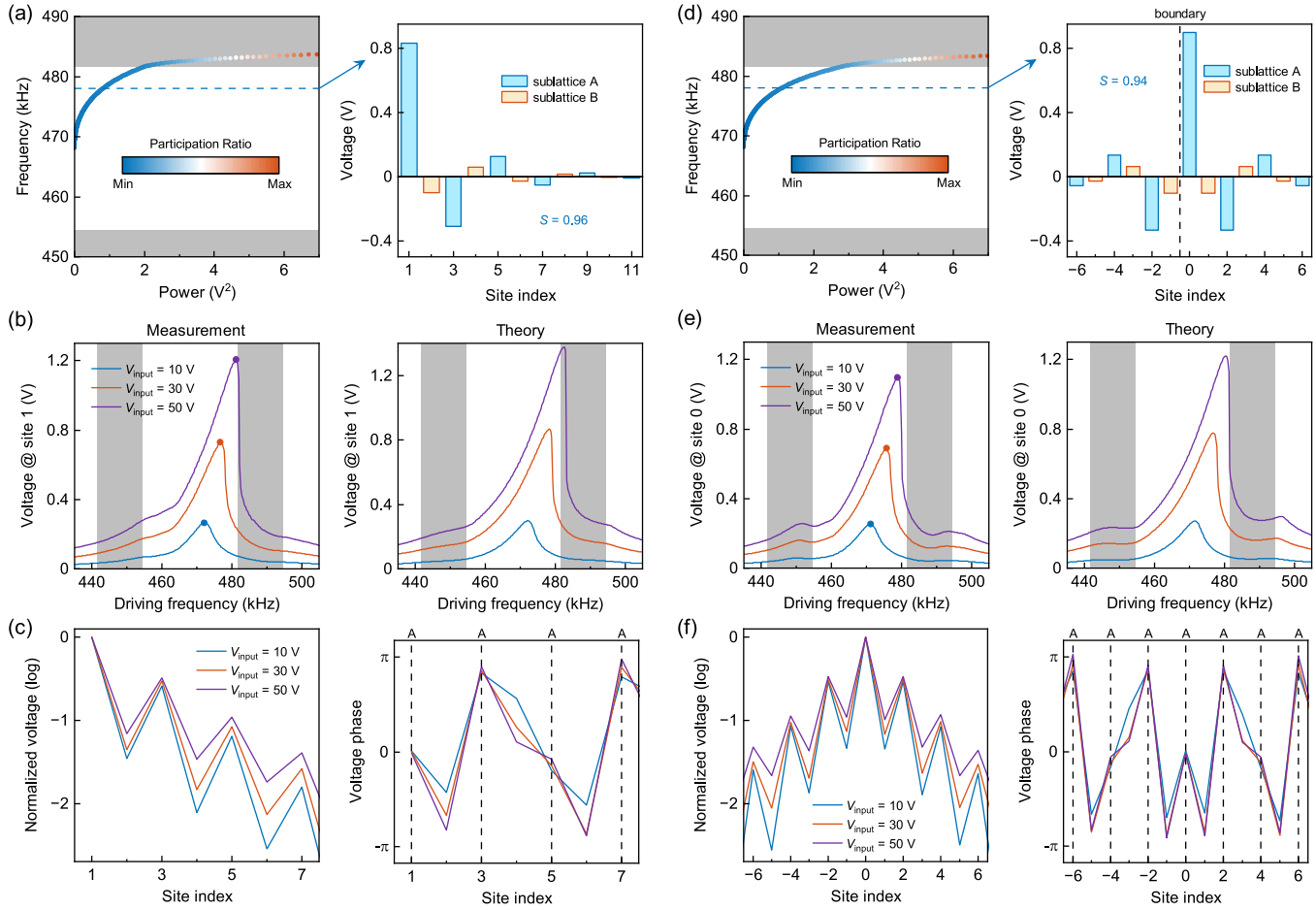

FIG. 3. Nonlinear topological edge states. (a) Nonlinear topological edge states residing at the edge of a semi-infinite SSH lattice that ends with a weak bond [Fig. 1(a)]. Participation ratio measures the state localization, with a large participation ratio signifying weak localization. The inset shows a typical voltage distribution of the nonlinear topological edge states. (b) At different input voltages, the voltage spectra measured experimentally and calculated theoretically. The driving frequency corresponds to the output frequency of the external voltage source. (c) The normalized amplitudes (left) and phases (right) of the experimental voltage distributions at the resonant frequencies indicated by the dots in panel (b). (d–f) Results for the nonlinear topological edge states in a structure formed by connecting two lattices with different topological properties in the linear limit [Fig. 1(b)].

Experimentally, we excite site 1 (i.e., the leftmost site) of the circuit lattice using an external input voltage with frequency sweep to observe the nonlinear topological edge states (see Appendix D for the detailed experimental implementation). The output frequency of the external voltage source corresponds to the driving frequency of the lattice (see further explanations in Appendix B, section 1). From the experimental and theoretical results shown in Fig. 3(b), under a small input voltage, the voltage spectrum exhibits a nearly symmetric peak with respect to the resonant frequency, indicating the presence of the topological edge state in the linear limit. As the input voltage increases, the spectrum peak becomes asymmetric and the resonant frequency exhibits a blue shift (see Fig. 12 in Appendix D for the complete voltage spectra). We further extract the resonant frequencies under different input voltages and measure the voltage distributions in the circuit lattice. The normalized amplitudes and phases of the experimental voltage distributions are shown in Fig. 3(c). At higher input voltages, the localization of the nonlinear edge state decreases, although the characteristics of sublattice polarization and phase jump remain intact (see Fig. 13 and Appendix D for the quantitative analysis). This observation aligns with the theoretical prediction and confirms that nonlinearity weakens the localization of the nonlinear topological edge states.

We then study the second configuration shown in Fig. 1(b). The structure is connected by two lattices with different topological properties defined in the linear limit (winding number $\mathcal{W} = 0$ for the left topologically trivial part and $\mathcal{W} = 1$ for the right nontrivial part [66]). Without nonlinearity, a topological edge state is localized at the boundary between the two parts [67,68]. Similarly, with onsite nonlinearity, nonlinear topological edge states which are bifurcated from the linear edge state appear, as shown in Fig. 3(d) (see Fig. 15 and Appendix E for the stability analysis). Due to the same physical origin, the nonlinear topological edge states in this lattice also exhibit the sublattice polarization and phase jump, and nonlinearity also weakens the state localization. These properties are confirmed by the experimental measurements presented in in Figs. 3(e) and 3(f) (see Appendix F for the experimental implementation, complete voltage spectra, and quantitative analysis). Note that the nonlinear topological edge states are

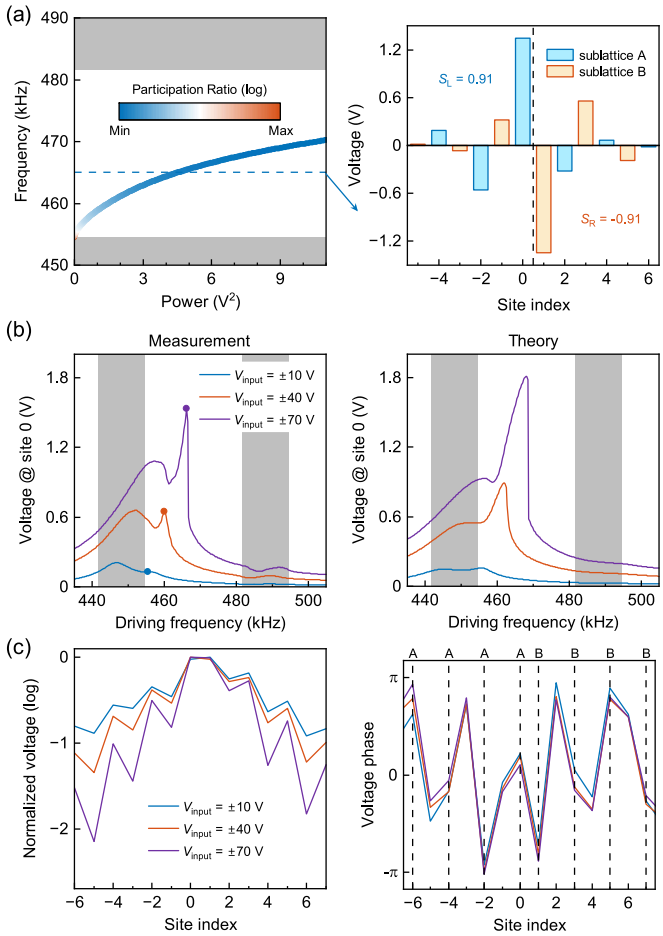

FIG. 4. Topological gap solitons. (a) Frequencies and participation ratios of the topological gap solitons in the nonlinear SSH lattice shown in Fig. 1(c). The inset shows a typical voltage distribution of the topological gap solitons. (b) Voltage spectra measured experimentally and calculated theoretically. (c) The normalized amplitudes (left) and phases (right) of the experimental voltage distributions at the resonant frequencies indicated by the dots in panel (b).

fundamentally different from conventional topologically trivial solitons, which do not exhibit these characteristics (see Fig. 16 and Appendix E for a discussion on topologically trivial edge states).

IV. TOPOLOGICAL GAP SOLITONS

We will now discuss the topological gap solitons in the third kind of the lattice [Fig. 1(c)]. In contrast to the nonlinear topological edge states, the topological gap solitons lack a direct linear counterpart, although they reside spectrally within the SSH gap. From Fig. 4(a), the topological gap solitons bifurcate from the edge of the linear Bloch band and converge to the bulk state in the linear limit (see Figs. 27 and 28 and Appendix G for the bifurcation and stability). Under the influence of onsite nonlinearity, a topological interface can be induced at the center unit cell of the lattice [49,50]. The Dirac mass defined as $m_{\mathrm{Dirac}} = \frac{g(V_m^A) - g(V_m^B)}{2}$ exhibits an inversion ($m_{\mathrm{Dirac}} > 0$ for the left part and $m_{\mathrm{Dirac}} < 0$ for the right part), and the topological gap solitons emerge as the Jackiw-Rebbi-type Dirac boundary modes (see Appendix G for the physical interpretation). The nonlinearity-induced interface can also be interpreted as an impurity potential that splits the the original lattice into two topological regions, and the topological gap soliton represents a combination of the two topological edge states [28].

The global sublattice polarizations of the topological gap solitons vanish because the left and right tails exhibit opposite chiralities [30]. From the inset in Fig. 4(a), the left tail is primarily confined to the sublattice site A, exhibiting a positive local sublattice pseudospin S_{L}, while the right tail displays a negative S_{R}. Experimentally, the topological gap solitons are excited using two out-of-phase input voltages, revealing the properties of both sublattice polarization and phase jumping, as shown in Figs. 4(b) and 4(c) (see Appendix H for the comprehensive analysis and excitation of topologically trivial gap solitons). In Fig. 4(b), the experimental measurement results deviate from the theoretical predictions at higher input voltages, primarily due to increased series resistance of the inductors and decreased driving voltages provided by the voltage source. In Fig. 4(c), the small deviations in the voltage distributions from the perfectly symmetric profiles may result from imperfections in the circuit lattice, discrepancies between actual and set input voltage levels, and the limited temporal resolution in the measurements (see Appendix D). Furthermore, since the topological gap solitons are nonlinearity-induced states, their localization is enhanced under stronger input voltages, provided that the delocalized gap solitons within the linear bulk band are not excited (see Appendix G).

V. SELF-INDUCED TOPOLOGICAL EDGE STATES

The nonlinear topological states we currently implement rely on either the physical edge of a topologically nontrivial lattice or a nonlinearity-induced topological interface between two lattices. In this section, we shift our focus to a semi-infinite lattice terminating with a strong bond and demonstrate the emergence of a new type of nonlinear topological state that resides at the edge of a nonlinear topologically trivial lattice.

Figure 5(a) shows the frequencies and participation ratios of the self-induced topological edge states. Although topological edge states do not exist in the linear limit, above a certain power threshold, localized states with their maxima reside at the leftmost unit cell appear in the SSH gap [see the inset of Fig. 5(a)]. Neglecting the voltage at the first site, the self-induced topological edge state exhibits the similar profile with the nonlinear topological edge state [the inset of Fig. 3(a)] and half of the topological gap soliton [the inset of Fig. 4(a)]. Considering the similarity, the self-induced topological edge states at the left edge can be created by the discrete translational transformation $\mathcal{T} V_m^{\mathrm{A,B}} = V_{m-1}^{\mathrm{A,B}}$, where $\mathcal{T}$ is the translational operator. The power threshold is induced by the breaking of discrete translational symmetry when moving the topological gap solitons toward the edge (see Appendix I 3, for the relation between self-induced topological edge states and topological gap solitons). Since the circuit nonlinearity adds perturbations to the onsite energy, the self-induced topological edge states can be approximated using the solutions of Eq. (1) with $g \neq 0$ for the leftmost unit cell and $g = 0$ for the other sites. When

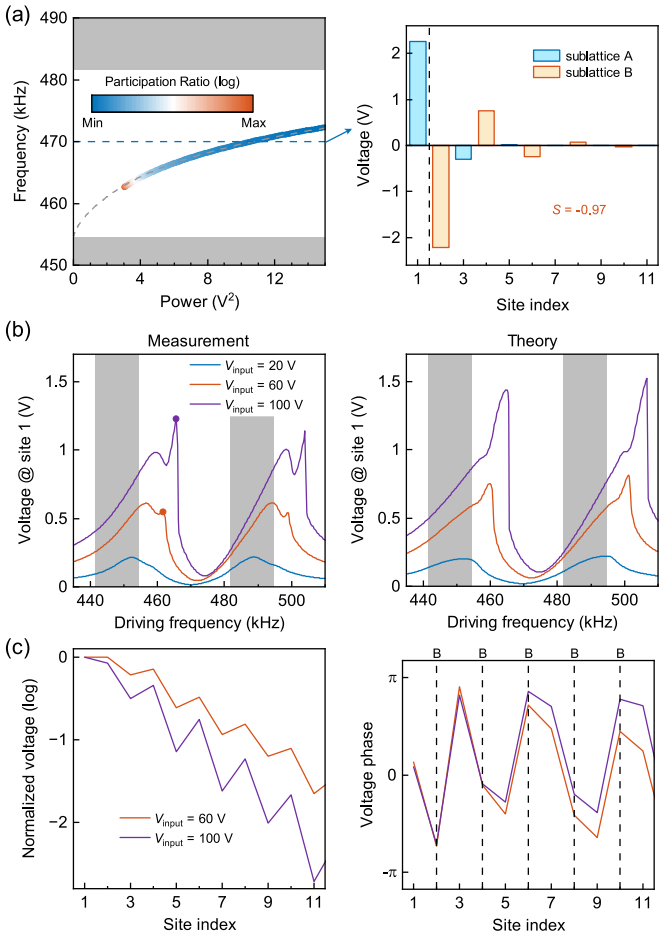

FIG. 5. Self-induced topological edge states. (a) Frequencies and participation ratios of the self-induced topological edge states in the nonlinear SSH lattice shown in Fig. 1(d). For comparison, the frequencies of the topological gap solitons from Fig. 4(a) are also plotted. The inset shows a typical voltage distribution of the self-induced topological edge states. (b) Voltage spectra measured experimentally and calculated theoretically. (c) The normalized amplitudes (left) and phases (right) of the experimental voltage distributions at the resonant frequencies indicated by the dots in panel (b).

the state frequency equals to the constant onsite energy E_0, i.e., the frequency of the linear topological edge state, the Gross-Pitaevskii equation reduces to

$$J_1 v_1^{\mathrm{B}} + g\left(v_1^{\mathrm{A}}\right) v_1^{\mathrm{A}} = 0, \tag{3}$$

$$J_1 v_1^{\mathrm{A}} + g\left(v_1^{\mathrm{B}}\right) v_1^{\mathrm{B}} = 0, \tag{4}$$

with $v_m^{\mathrm{B}} = (-\frac{J_1}{J_2})^{|m|-1} v_1^{\mathrm{B}}$ and $v_m^{\mathrm{A}} = 0$ for $m \geqslant 2$ (see Appendix I). Equations (3) and (4) govern the voltage distributions in a single dimer and allow for an antisymmetric solution: $v_1^{\mathrm{A}} = -v_1^{\mathrm{B}}$ with $g(v_1^{\mathrm{A}}) = J_1$, which is consistent with the profile shown in the inset of Fig. 5(a). The relationship between the voltages at the other sites is precisely analogous to that of a linear topological edge state. Thus, the self-induced topological edge states residing at the edge of a topologically trivial lattice represent a continuation of the antisymmetric state in the anti-continuum limit (see Appendix I 3), and they can be approximately mapped to the linear topological edge state of a semi-infinite SSH lattice.

To experimentally investigate the self-induced topological edge states, we excite the leftmost site, specifically site 1 of the circuit lattice. Figure 5(b) displays the experimental and theoretical voltage spectra. The experimental results show deviations from the theoretical predictions at higher input voltages, primarily due to increased series resistance in the inductors and reduced driving voltages supplied by the voltage source. From Fig. 5(b), no peak is observed in the SSH gap for $V_{\mathrm{input}} = 20$ V, indicating the existence of a power threshold for the self-induced topological edge states. The threshold value obtained from the excitation spectra deviates from the result in Fig. 5(a) possibly due to the excitation of other nonlinear states (see Appendix J). At high input voltages, the voltage distributions in Fig. 5(c) reveal that the self-induced topological edge states exhibit sublattice polarization and phase jump starting from the second site near the physical termination. Meanwhile, similar to the topological gap solitons, nonlinearity can enhance the localization of self-induced topological edge states, unless the resonant frequency is driven into the linear bulk band, which is consistent with the theoretical prediction in Fig. 5(a). Note that the resonant peak in the semi-infinite gap in Fig. 5(b) corresponds to the excitation of topologically trivial conventional solitons (see Appendix J for the discussion on topologically trivial edge solitons).

In comparison to the self-induced topological states reported by Hadad *et al.* [59], our self-induced topological edge states offer two main advantages. First, our self-induced topological edge states feature decaying tails that approach zero, which indicates that the powers of the edge states are finite. In contrast, the self-induced topological states reported by Hadad *et al.* exhibit nonzero plateau levels in the limit of $m \to \infty$ [59]. Such extended modes carry infinite power and are physically unrealizable. Second, our self-induced topological edge states are realized in a lattice with onsite nonlinearity, as opposed to the topological edge states induced by nonlinear couplings. In realistic interacting systems, such as photonic and cold atomic systems, onsite nonlinearity is more readily achievable [54,55,69,70]. For instance, in a cold atomic system, the interaction between particles at the same site is significantly stronger than the interactions between particles at neighboring sites, leading to the emergence of onsite nonlinearity (see further discussions in Appendix B 3). These two advantages imply that our results are physically realizable and broadly applicable.

VI. DISCUSSION ON THE TOPOLOGICAL PROPERTIES

In the previous sections, we studied nonlinear topological edge states, topological gap solitons, and self-induced topological edge states. Here, we aim to address the topological properties of these types of nonlinear states.

In the absence of onsite nonlinearity, a linear SSH model belongs to a one-dimensional (1D) chiral symmetric system in class BDI. The traditional 1D winding number can be well defined as the topological invariant [71], as introduced in Sec. III. For a topologically nontrivial SSH lattice with a winding number of $\mathcal{W} = 1$, topological edge states emerge at the physical termination of an open chain. These topological

edge states can also appear at the domain wall between two chains with $\mathcal{W} = 0$ and $\mathcal{W} = 1$, respectively. The nonlinear topological edge states shown in Figs. 3(a)–3(c) bifurcate from the topological edge state at the physical termination, and those depicted in Figs. 3(d)–3(f) bifurcate from the topological edge state located at the domain wall. In contrast, the topological gap solitons shown in Fig. 4 and the self-induced topological edge states illustrated in Fig. 5 do not have linear counterparts, as they are localized states purely induced by nonlinearity.

When nonlinearity is introduced to the original SSH model, the ability to define a topological invariant depends on the nature of the nonlinearity [33]. If the introduced nonlinearity does not break the symmetry operations associated with the original topological classification—such as in nonlinear SSH models with nonlinear coupling coefficients—then the original definition of the winding number can still be utilized or modified to describe the topological properties of the edge states [59,72–75]. In our study, we add nonlinear onsite energies to the original SSH model. When we consider the contribution from the nonlinear states to the onsite energies, the chiral symmetry, which is one of the symmetry operators in class BDI, is broken. Consequently, the nonlinear SSH model cannot be classified into any of the classes in the periodic table of topological insulators. Although the band structure can still be defined by using the Bloch ansatz, Zak phase is generally not quantized [28]. Even the spectral localizer, a local topological invariant defined in real space, becomes inapplicable in this scenario [76–79]. These previous findings indicate that it remains challenging to identify an appropriate topological invariant that accurately describes a nonlinear system where nonlinearity break the symmetries necessary for topological classification, unless the topological protection of the original linear system does not rely on any symmetry operations, as exemplified by Chern insulators [80].

Considering this ongoing challenge, our study approaches the determination of whether a nonlinear state is topologically nontrivial or trivial from a phenomenological perspective. We assert that the nonlinear edge states shown in Fig. 3 are topologically nontrivial because they bifurcate from their linear counterparts, which are topological edge states residing at the edge of a topologically nontrivial lattice. The term "nonlinear topological edge states" aligns with the terminology used in previous studies [25,26,29–32,36]. The gap solitons depicted in Fig. 4 are classified as topological gap solitons, as they reside in the topological bandgap and represent nonlinearity-induced Jackiw-Rebbi-type Dirac boundary modes [30,48–53]. For the self-induced topological edge state shown in Fig. 5, we argue that it can be considered a topological edge state due to its hallmark features of a linear topological edge state, including sublattice polarization, phase jumps, and a decaying tail that approaches zero. Additionally, it can be regarded as a variant of the topological gap soliton resulting from the breaking of discrete translational symmetry at the edge of the structure. Even so, a precise definition of the topological invariants and the establishment of a general bulk-boundary correspondence are still needed.

Very recently, Sone *et al.* developed an elegant framework for the nonlinear SSH model with onsite Kerr nonlinearity. By applying the Bloch ansatz, they demonstrated that the model preserves space-inversion symmetry in momentum space [81]. Within this setting, the nonlinear Berry phases become quantized, establishing a well-defined bulk-boundary correspondence in the nonlinear regime. Building upon this insightful and highly relevant approach, we performed supplementary calculations for our model with onsite saturable nonlinearity. Our results confirm that the nonlinear topological edge states presented in Fig. 3 can be described within this theoretical framework (see Appendix K for further details).

VII. CONCLUSION

In conclusion, we experimentally and theoretically reveals the existence of the nonlinear topological edge states and topological gap solitons in the nonlinear SSH circuit lattices. Contrary to the conventional understanding of the bulk-boundary correspondence, we demonstrate the formation of the self-induced topological edge states that reside at the physical termination (rather than the nonlinearity-induced interface) of a nonlinear topologically trivial lattice. This exotic type of nonlinear topological states may pave the way to exploring intriguing topological states in more complex nonlinear topological systems, such as high-dimensional or higher-order systems, and the platform of nonlinear electric circuits may be used to explore the interacting topological physics [82].

ACKNOWLEDGMENTS

The authors thank Terry A. Loring, Di Zhou, Meng Xiao, Kai Bai, Weixuan Zhang, and Fengxiao Di for fruitful discussions. The authors also thank Yongle Lou for providing access to the experimental facilities. R.L., W.W., and X.K. were sponsored by the National Key Research and Development Program of China (Grant No. 2022YFA1404902), the National Natural Science Foundation of China (Grant No. 12104353), and the Fundamental Research Funds for the Central Universities (Grant No. QTZX25086). Y.L. was sponsored by the National Natural Science Foundation of China (NSFC) under Grant No. 61871309 and the 111 Project. B.Z. acknowledges support from Singapore National Research Foundation Competitive Research Program Grant No. NRF-CRP23-2019-0007, Singapore Ministry of Education Academic Research Fund Tier 2 Grant No. MOE-T2EP50123-0007, and Tier 1 Grant No. RG81/23.

DATA AVAILABILITY

The data that support the findings of this article are not publicly available upon publication because it is not technically feasible and/or the cost of preparing, depositing, and hosting the data would be prohibitive within the terms of this research project. The data are available from the authors upon reasonable request.

APPENDIX A: MODELING OF BACK-TO-BACK VARACTOR DIODES

We use the back-to-back varactor diodes to provide the onsite nonlinearity of the nonlinear SSH models. Such

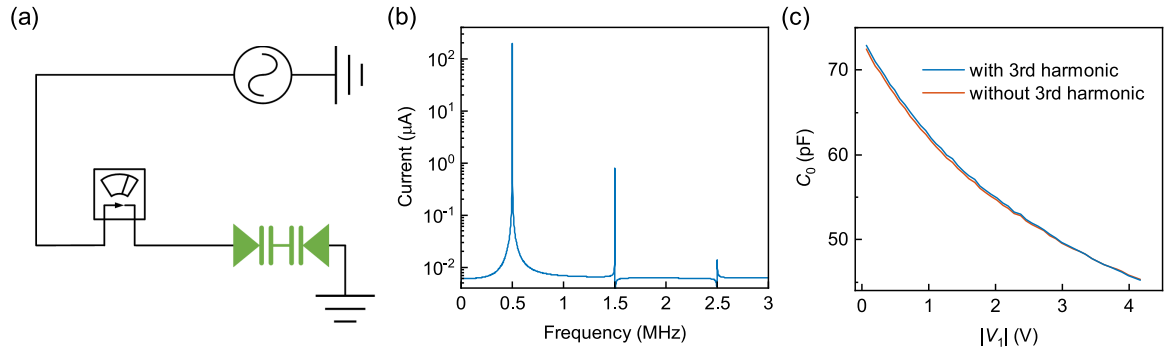

FIG. 6. Modeling of back-to-back varactor diodes. (a) Circuit diagram of the simulation, where the current response of a back-to-back varactor diode under the excitation from a voltage source is probed. (b) The probed current signal displayed in the frequency domain. (c) The experimentally measured capacitance-voltage relation of the back-to-back varactor diode, where the blue and orange curves denote the results calculated with and without the third-harmonic current components.

topology of double diode with a common cathode ensures the same response of the two half-cycles of an AC voltage and avoids the use of a bias voltage [59]. To model the capacitance of the back-to-back varactor diodes, we simulate the current response of a variable capacitance double diode with a common cathode (BB201) under the excitation from a voltage source using Advanced Design System. The circuit diagram is shown in Fig. 6(a) and the parameters for the Spice model are taken from the manufacturer website. The voltage source has an amplitude of 1 V and the frequency is 500 kHz. Note that there is no DC biasing in the simulation. Based on the circuit configuration, after a Fourier transform of the temporal current signal, we find that the current contains the high-harmonic components, as shown in Fig. 6(b). The even-order harmonics are suppressed due to the symmetric configuration of the back-to-back varactor diode [60].

The existence of the high-harmonic currents implies that the capacitance of the back-to-back varactor diode is time-dependent. In this paper, we only consider the first- and third-harmonic current components, and neglect the higher-order harmonics. The voltage and current in the circuit can be written as $V(t) = \frac{1}{2}V_1 e^{-i\omega t} + \text{c.c.}$ and $I(t) = \frac{1}{2}I_1 e^{-i\omega t} + \frac{1}{2}I_3 e^{-3i\omega t} + \text{c.c.}$, respectively, where c.c. denotes the complex conjugates of the terms to the left. From the expressions, V_1 and I_1 are the amplitudes of the first-harmonic components, and I_3 is the amplitude of the third-harmonic current. Then the capacitance of the back-to-back varactor diode can be expressed as

$$C(t) = C_0 + \tfrac{1}{2}C_2 e^{-2i\omega t} + \text{c.c.}, \tag{A1}$$

where

$$C_0 = \frac{I_1 + I_3 \frac{V_1^*}{V_1}}{-i\omega V_1}, \tag{A2}$$

$$C_2 = \frac{2I_3}{-i\omega V_1}. \tag{A3}$$

Specifically, the capacitance of the back-to-back varactor diode further reduces to

$$C = C_0 = \frac{I_1}{-i\omega V_1}, \tag{A4}$$

when the third-harmonic current component is also neglected. To characterize the capacitance-voltage relation of the back-to-back varactor diode, we experimentally measure the voltage and current using an oscilloscope, and calculate the value of C_0 when considering or neglecting the third-harmonic current component, respectively. The capacitance-voltage relationship of the back-to-back varactor diode is symmetric with respect to $V_1 = 0$, as shown in Fig. 6(c). The two curves for C_0 calculated with and without the third harmonics agree well with each other within the whole voltage range. The small discrepancy near the zero voltage is due to the inaccuracy in measuring the small voltage signals. The result implies that the third-harmonic current component can be neglected in our study, and Eq. (A4) is sufficient to characterize the capacitance of the back-to-back varactor diodes. To facilitate the theoretical modeling, we fit the experimental capacitance-voltage curve with the formula

$$C(v) = \frac{C_L}{\left(1 + \left|\frac{v}{v_0}\right|\right)^M}, \tag{A5}$$

where C_L is the capacitance at the zero voltage, v_0 and M are constants, and v is the amplitude of the applied voltage. Thus, the back-to-back varactor diode acts as a variable capacitor, whose capacitance depends on the voltage amplitude. We have also measured the back-to-back varactor diode at other frequencies experimentally and Eq. (A5) is valid within the whole parameter range of our study. Extending the above conclusion, when the applied voltage is quasimonochromatic with $V(t) = \frac{1}{2}v(t)e^{-i\omega t} + \text{c.c.}$, the capacitance of the back-to-back varactor diode can be written as

$$C(v) = \frac{C_L}{\left[1 + \left|\frac{v(t)}{v_0}\right|\right]^M}, \tag{A6}$$

where $v(t)$ is the slowly varying amplitude envelope. In this case, the capacitance of the varactor diode varies with the voltage envelope. This formula will be used to study the localized states in the nonlinear SSH circuit lattices. Specifically, when the applied voltage is near zero, Eq. (A6) can be approximated as

$$C(v) = C_L\left(1 - M\left|\frac{v}{v_0}\right|\right). \tag{A7}$$

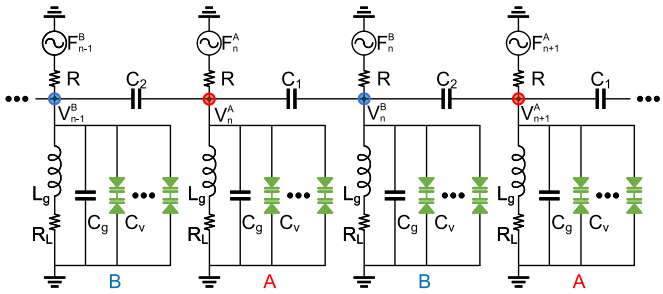

FIG. 7. Diagram of the nonlinear SSH circuit lattice. For generality, we show the schematic of the driven-dissipative nonlinear SSH circuit, where the voltage sources $F_n^{\mathrm{A,B}}$ with the shunt resistors R are connected to the circuit nodes and the series resistance of the inductors R_L is considered. To enhance the onsite nonlinearity, η varactor diodes are wired in parallel.

Based on the discussion above, for a fixed type of back-to-back varactor diodes, we can determine the parameters C_{L}, v_0, and M by fitting the experimental capacitance-voltage relationship. For our specific type (BB201), we measured the capacitance-voltage relationship at different frequencies and found that the parameter values remain unchanged within the range of 100 kHz to 1 MHz.

APPENDIX B: DERIVATION OF GP EQUATION FROM KIRCHHOFF CIRCUIT EQUATIONS

This Appendix is organized as follows. First, we give the derivation of the GP equation from the Kirchhoff circuit equations, and discuss the applicable conditions of the GP equation. In the second subsection, we prove the validity of the GP equation by developing an accurate nonlinear circuit model. Finally, in the last subsection, we show that the nonlinear electric circuit lattices can be used to explore the many-body interacting topological physics.

1. Derivation of GP equation

For generality, we derive the GP equation of a nonlinear SSH circuit lattice with the external driving sources and circuit dissipations. As shown in Fig. 7, the circuit lattice is composed of the coupled nonlinear LC oscillators. There are two sublattice sites A and B in one unit cell. For one sublattice, the inductor L_{g}, capacitor C_{g}, and back-to-back varactor diode C_{v} are wired in parallel. The varactor diode acts as a voltage-dependent variable capacitor with $C_{\mathrm{v}} = C_{\mathrm{L}} + C_{\mathrm{NL}}$, where the linear part C_{L} is the capacitance at the zero voltage and the nonlinear part can be usually phenomenologically written as $C_{\mathrm{NL}} = -C_{\mathrm{L}} + \frac{C_{\mathrm{L}}}{(1+|v/v_0|)^M}$. Here, v_0 and M are constants, and v is the amplitude of the applied voltage. The sublattice sites are wired with each other through the intracell coupling capacitor C_1 and intercell coupling capacitor C_2. Experimentally, we need to add voltage sources to excite the circuit lattice and the Ohmic losses of the circuit components should be considered. From Fig. 7, the circuit lattice is driven by the external continuous voltage sources with $F_m^{\sigma} = \frac{1}{2} f_m^{\sigma} e^{-\mathrm{i}\omega t} + \mathrm{c.c.}$ through the shunt resistors R, where f_m and ω are the voltage amplitude and output angular frequency of the voltage source, respectively. Under such excitation, the frequency of the voltages at the circuit nodes is always equal to the frequency of the external voltage sources, because here we neglect the small high-harmonic components induced by the varactor diodes. We assume that the shunt resistors are large enough such that the circuit lattice is excited by the equivalent current sources (please refer to the additional discussion in Appendix F 1). For the Ohmic losses of the circuit components, here we only consider the series resistance of inductors R_L because the varactor diodes that we use have very low series resistance. Besides, to enhance the nonlinearity of the circuit we use η varactor diodes which are wired in parallel.

In this circuit, the nonlinear part of the varactor diode C_{NL} is usually small, and the total grounding capacitance can be approximated as $C_{\mathrm{g}} + \eta C_{\mathrm{L}}$. We require that the coupling capacitances are much smaller than the grounding capacitance, i.e., $C_{1,2} \ll C_{\mathrm{g}} + \eta C_{\mathrm{L}}$, then the voltages at the lattice sites of the mth cell can be written as $V_m^{\sigma}(t) = \frac{1}{2} v_m^{\sigma}(t) e^{-\mathrm{i}\omega_0 t} + \mathrm{c.c.}$ with $\sigma = \mathrm{A}, \mathrm{B}$, where v_m^{σ} are the amplitude envelopes (slowly varying complex amplitudes), $\omega_0 = 1/\sqrt{L_{\mathrm{g}}(C_{\mathrm{g}} + \eta C_{\mathrm{L}})}$ is the carrier frequency of the voltages, and c.c. denotes the complex conjugate of the term to the left. Using this expression, we have separated the slowly varying and fast-varying parts. Accordingly, the capacitance of the varactor diode in the mth cell varies with the voltage envelope and we have $C_{\mathrm{NL},m}^{\sigma} = -C_{\mathrm{L}} + \frac{C_{\mathrm{L}}}{(1+|v_m^{\sigma}/v_0|)^M}$. For the mth unit cell, at node A where the voltage is V_m^{A}, we have the following relations:

$$L_{\mathrm{g}} \frac{dI_{L_{\mathrm{g}}}(t)}{dt} = V_m^{\mathrm{A}}(t) - V_{R,L}(t), \tag{B1}$$

$$I_{L_{\mathrm{g}}}(t) R_L = V_{R,L}(t), \tag{B2}$$

$$C_{\mathrm{g}} \frac{dV_m^{\mathrm{A}}(t)}{dt} = I_{C_{\mathrm{g}}}(t), \tag{B3}$$

$$C_{\mathrm{v}}\left[v_m^{\mathrm{A}}(t)\right] \frac{dV_m^{\mathrm{A}}(t)}{dt} = I_{C_{\mathrm{v}}}(t), \tag{B4}$$

$$C_2 \frac{d\left[V_m^{\mathrm{A}}(t) - V_{m-1}^{\mathrm{B}}(t)\right]}{dt} = I_{C_2}(t), \tag{B5}$$

$$C_1 \frac{d\left[V_m^{\mathrm{A}}(t) - V_m^{\mathrm{B}}(t)\right]}{dt} = I_{C_1}(t). \tag{B6}$$

Considering the Kirchhoff's current law with

$$I_{C_1}(t) + I_{C_2}(t) + I_{C_{\mathrm{g}}}(t) + I_{L_{\mathrm{g}}}(t) + \eta I_{C_{\mathrm{v}}}(t) = \frac{F_m^{\mathrm{A}}(t) - V_m^{\mathrm{A}}(t)}{R}, \tag{B7}$$

we have

$$\left[C_1 + C_2 + C_{\mathrm{g}} + \eta C_{\mathrm{v}}\left(v_m^{\mathrm{A}}\right)\right] \frac{dV_m^{\mathrm{A}}}{dt} - C_1 \frac{dV_m^{\mathrm{B}}}{dt} - C_2 \frac{dV_{m-1}^{\mathrm{B}}}{dt} + \frac{V_{R,L}}{R_{L_{\mathrm{g}}}} = \frac{1}{R} F_m^{\mathrm{A}} - \frac{1}{R} V_m^{\mathrm{A}}, \tag{B8}$$

$$\left[C_1 + C_2 + C_{\mathrm{g}} + \eta C_{\mathrm{v}}\left(v_m^{\mathrm{A}}\right)\right] \frac{d^2 V_m^{\mathrm{A}}}{dt^2} - C_1 \frac{d^2 V_m^{\mathrm{B}}}{dt^2} - C_2 \frac{d^2 V_{m-1}^{\mathrm{B}}}{dt^2} + \frac{V_m^{\mathrm{A}} - V_{R,L}}{L_{\mathrm{g}}} = \frac{1}{R} \frac{dF_m^{\mathrm{A}}}{dt} - \frac{1}{R} \frac{dV_m^{\mathrm{A}}}{dt}, \tag{B9}$$

where the approximation $dv_m^{\mathrm{A}}/dt = 0$ is used since v_m^{A} is slowly varying against time. From Eqs. (B8) and (B9), we get the following relation:

$$L_{\mathrm{g}}(C_{\mathrm{g}}+\eta C_L)\frac{d^2V_m^{\mathrm{A}}}{dt^2}+L_{\mathrm{g}}\big[C_1+C_2+\eta C_{\mathrm{NL}}\big(v_m^{\mathrm{A}}\big)\big]\frac{d^2V_m^{\mathrm{A}}}{dt^2}-L_{\mathrm{g}}C_1\frac{d^2V_m^{\mathrm{B}}}{dt^2}-L_{\mathrm{g}}C_2\frac{d^2V_{m-1}^{\mathrm{B}}}{dt^2}+R_{L_{\mathrm{g}}}(C_{\mathrm{g}}+\eta C_{\mathrm{L}})\frac{dV_m^{\mathrm{A}}}{dt}$$
$$+R_L\big[C_1+C_2+\eta C_{\mathrm{NL}}\big(v_m^{\mathrm{A}}\big)\big]\frac{dV_m^{\mathrm{A}}}{dt}+\frac{L_{\mathrm{g}}}{R}\frac{dV_m^{\mathrm{A}}}{dt}-R_LC_1\frac{dV_m^{\mathrm{B}}}{dt}-R_LC_2\frac{dV_{m-1}^{\mathrm{B}}}{dt}+V_m^{\mathrm{A}}+\frac{R_L}{R}V_m^{\mathrm{A}}=\frac{L_{\mathrm{g}}}{R}\frac{dF_m^{\mathrm{A}}}{dt}+\frac{R_L}{R}F_m^{\mathrm{A}}. \quad \text{(B10)}$$

From the expressions for the voltages $V_m^{\mathrm{A,B}}(t)$, we can get their first and second derivatives. Considering that $C_{\mathrm{g}}+\eta C_{\mathrm{L}} \gg C_{1,2,\mathrm{NL}}$ and $R \gg R_{\mathrm{L}}$, we adopt the slowly varying envelop approximation. In the first line of Eq. (B10), we use

$$\frac{d^2V_m^{\mathrm{A,B}}}{dt^2}=-\mathrm{i}\omega_0\frac{dv_m^{\mathrm{A,B}}}{dt}e^{-\mathrm{i}\omega_0 t}-\frac{\omega_0^2}{2}v_m^{\mathrm{A,B}}e^{-\mathrm{i}\omega_0 t}+\mathrm{c.c.} \quad \text{(B11)}$$

for the first term and

$$\frac{d^2V_m^{\mathrm{A,B}}}{dt^2}=-\frac{\omega_0^2}{2}v_m^{\mathrm{A,B}}e^{-\mathrm{i}\omega_0 t}+\mathrm{c.c.} \quad \text{(B12)}$$

for the other terms. In the second line, we use

$$\frac{dV_m^{\mathrm{A,B}}}{dt}=-\frac{\mathrm{i}\omega_0}{2}v_m^{\mathrm{A,B}}e^{-\mathrm{i}\omega_0 t}+\mathrm{c.c.} \quad \text{(B13)}$$

for the first and third terms, and the other terms are directly omitted. In the third line, the second term is also omitted. Similarly, in the last line we omit the second term. Thus, Eq. (B10) reduces to

$$\mathrm{i}\frac{dv_m^{\mathrm{A}}}{dt}=-\frac{C_1+C_2+\eta C_{\mathrm{NL}}\big(v_m^{\mathrm{A}}\big)}{2(C_{\mathrm{g}}+\eta C_{\mathrm{L}})}\omega_0 v_n^{\mathrm{A}}-\mathrm{i}\left[\frac{R_L}{2L_{\mathrm{g}}}+\frac{1}{2R(C_{\mathrm{g}}+\eta C_{\mathrm{L}})}\right]v_m^{\mathrm{A}}$$
$$+\frac{C_1}{2\big(C_{\mathrm{g}}+\eta C_L\big)}\omega_0 v_m^{\mathrm{B}}+\frac{C_2}{2(C_{\mathrm{g}}+\eta C_{\mathrm{L}})}\omega_0 v_{m-1}^{\mathrm{B}}+\mathrm{i}\frac{\omega}{2R(C_{\mathrm{g}}+\eta C_{\mathrm{L}})\omega_0}f_m^{\mathrm{A}}e^{-\mathrm{i}(\omega-\omega_0)t}. \quad \text{(B14)}$$

The slowly varying envelope approximation simplifies the second-order differential equations into the first-order ones. We define $v_m^{\mathrm{A,B}}(t)=V_m^{\mathrm{A,B}}(t)\exp(\mathrm{i}\omega_0 t)$ and $f_m^{\mathrm{A,B}}(t)=F_m^{\mathrm{A,B}}(t)\exp(\mathrm{i}\omega t)$, where ω is the external driving frequency. Substituting the two expressions into Eq. (B14), we get

$$\mathrm{i}\frac{dV_m^{\mathrm{A}}}{dt}=\left[1-\frac{C_1+C_2+\eta C_{\mathrm{NL}}\big(V_m^{\mathrm{A}}\big)}{2(C_{\mathrm{g}}+\eta C_{\mathrm{L}})}\right]\omega_0 V_m^{\mathrm{A}}-\mathrm{i}\left[\frac{R_L}{2L_{\mathrm{g}}}+\frac{1}{2R(C_{\mathrm{g}}+\eta C_{\mathrm{L}})}\right]V_m^{\mathrm{A}}$$
$$+\frac{C_1}{2(C_{\mathrm{g}}+\eta C_{\mathrm{L}})}\omega_0 V_m^{\mathrm{B}}+\frac{C_2}{2(C_{\mathrm{g}}+\eta C_{\mathrm{L}})}\omega_0 V_{m-1}^{\mathrm{B}}+\mathrm{i}\frac{\omega}{2R(C_{\mathrm{g}}+\eta C_{\mathrm{L}})\omega_0}F_m^{\mathrm{A}}. \quad \text{(B15)}$$

For the convenience of theoretical calculation, we introduce the frequency ω_n which is a constant with an arbitrary value. We normalize t by defining $T=\omega_n t$ and get

$$\mathrm{i}\frac{dV_m^{\mathrm{A}}}{dT}=\left[1-\frac{C_1+C_2+\eta C_{\mathrm{NL}}\big(V_m^{\mathrm{A}}\big)}{2(C_{\mathrm{g}}+\eta C_{\mathrm{L}})}\right]\frac{\omega_0}{\omega_n}V_m^{\mathrm{A}}-\mathrm{i}\left[\frac{R_L}{2\omega_n L_{\mathrm{g}}}+\frac{1}{2R\omega_n(C_{\mathrm{g}}+\eta C_{\mathrm{L}})}\right]V_m^{\mathrm{A}}$$
$$+\frac{C_1}{2(C_{\mathrm{g}}+\eta C_{\mathrm{L}})}\frac{\omega_0}{\omega_n}V_m^{\mathrm{B}}+\frac{C_2}{2(C_{\mathrm{g}}+\eta C_{\mathrm{L}})}\frac{\omega_0}{\omega_n}V_{m-1}^{\mathrm{B}}+\mathrm{i}\frac{1}{2R\omega_0(C_{\mathrm{g}}+\eta C_{\mathrm{L}})}\bar{\omega}F_m^{\mathrm{A}}, \quad \text{(B16)}$$

where $\bar{\omega}=\omega/\omega_n$ is the normalized external driving frequency. This equation can be rewritten as

$$\mathrm{i}\frac{dV_m^{\mathrm{A}}}{dT}=(E_0-\mathrm{i}\gamma)V_m^{\mathrm{A}}+g\big(V_m^{\mathrm{A}}\big)V_m^{\mathrm{A}}+J_1V_m^{\mathrm{B}}+J_2V_{m-1}^{\mathrm{B}}+\mathrm{i}dF_m^{\mathrm{A}}, \quad \text{(B17)}$$

where

$$E_0=\left[1-\frac{C_1+C_2}{2(C_{\mathrm{g}}+\eta C_{\mathrm{L}})}\right]\frac{\omega_0}{\omega_n} \quad \text{(B18)}$$

is the constant onsite energy,

$$\gamma=\gamma_L+\gamma_R=\frac{R_L}{2\omega_n L_{\mathrm{g}}}+\frac{1}{2R\omega_n(C_{\mathrm{g}}+\eta C_{\mathrm{L}})} \quad \text{(B19)}$$

is the dissipation coefficient,

$$J_1 = \frac{C_1}{2(C_g + \eta C_L)} \frac{\omega_0}{\omega_n} \tag{B20}$$

and

$$J_2 = \frac{C_2}{2(C_g + \eta C_L)} \frac{\omega_0}{\omega_n} \tag{B21}$$

are the intracell and intercell coupling coefficients, respectively,

$$g\left(V_m^A\right) = -\frac{\eta C_{NL}\left(V_m^A\right)}{2(C_g + \eta C_L)} \frac{\omega_0}{\omega_n} \tag{B22}$$

is the voltage-dependent onsite energy, and

$$d = \frac{1}{2R\omega_0(C_g + \eta C_L)} \bar{\omega} \tag{B23}$$

is the coupling coefficient between the excitation source and circuit node. Note that γ_L and γ_R denote the dissipations induced by the series resistance of the inductors and shunt resistors, respectively. Following the similar procedure, the equation for V_m^B is written as

$$\begin{aligned} i\frac{dV_m^B}{dT} &= (E_0 - i\gamma)V_m^B + g\left(V_m^B\right)V_m^B + J_1 V_m^A \\ &\quad + J_2 V_{m+1}^A + i dF_m^B, \end{aligned} \tag{B24}$$

where

$$g\left(V_m^B\right) = -\frac{\eta C_{NL}\left(V_m^B\right)}{2(C_g + \eta C_L)} \frac{\omega_0}{\omega_n}. \tag{B25}$$

Thus, starting from the Kirchhoff circuit equations, we have analytically derived the discretized GP equation. Due to the external driving and circuit dissipation, Eqs. (B17) and (B24) contain the driven and dissipative terms. If we are interested in the mode properties of the nonlinear topological states in the SSH circuit, then we can disconnect the voltage sources and shunt resisters, and neglect the series resistance of the inductors. With $R = \infty$ and $R_L = 0$, Eqs. (B17) and (B24) reduce to

$$i\frac{dV_m^A}{dT} = E_0 V_m^A + g\left(V_m^A\right)V_m^A + J_1 V_m^B + J_2 V_{m-1}^B, \tag{B26}$$

$$i\frac{dV_m^B}{dT} = E_0 V_m^B + g\left(V_m^B\right)V_m^B + J_1 V_m^A + J_2 V_{m+1}^A, \tag{B27}$$

with the parameters the same as those defined in Eqs. (B18), (B20)–(B22), and (B25). Equations (B26) and (B27) are exactly the discretized GP equation introduced in the main text.

We note that the coupling coefficients J_1 and J_2 in Eqs. (B17) and (B24) are both positive. However, the coupling phases can be tuned by changing the coupling capacitors. For instance, J_1 and J_2 would be negative if we use the negative capacitors. Figure 8 shows the circuit diagram of the negative capacitor. It is composed of two parallelly connected negative impedance converters (NICs) [83]. The upper NIC creates the negative capacitance $-C_A$ at the left side and positive capacitance C_B at the right side. Reversely, the lower NIC creates the positive capacitance C_B at the left side and negative capacitance $-C_A$ at the right side. Thus, we have $C = C_A + C_B$, and the total capacitance is negative if $|C_A| > |C_B|$.

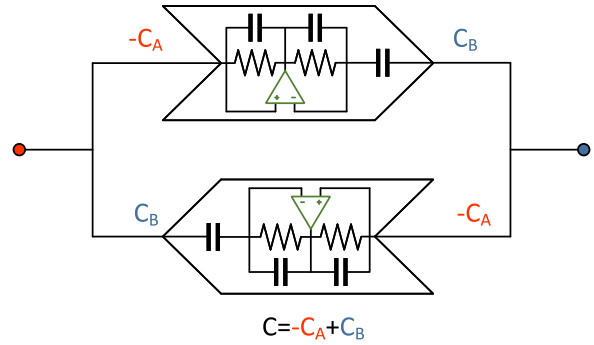

FIG. 8. Circuit diagram of the negative capacitor. The upper component has a negative capacitance $-C_A$ at the left side and positive capacitance C_B at the right side. While the lower component has a positive capacitance C_B at the left side and negative capacitance $-C_A$ at the right side. Under such configuration, the total capacitance C is negative if $|C_A| > |C_B|$.

The validity of Eqs. (B17) and (B24), as well as Eqs. (B26) and (B27), require that $C_g + \eta C_L \gg C_{1,2,NL}$ and $R \gg R_L$. These conditions can be easily satisfied by properly determining the component values. Thus, considering the realistic experimental realization, the circuit lattice is captured by the discretized GP equation. Besides, we note that Eqs. (B17) and (B24) can also be treated as the temporal coupled-mode equations in the circuit lattices [84].

2. Validity of GP equation

To validate the correctness of the GP equation, we have also developed an accurate nonlinear circuit model which can be used to study the steady states in the circuits. We study the SSH circuit lattice shown in Fig. 7 and consider the case where the external excitation is monochromatic. For the mth unit cell, at node A where the voltage is $V_m^A(t)$, Eqs. (B1)–(B6) are still valid when the circuit reaches the steady state, and the only difference is that v_m^A in Eq. (B4) is now time independent. Transforming the relations into the frequency domain, we have

$$-i\omega L_g i_{L_g} = v_m^A - v_{R,L}, \tag{B28}$$

$$i_{L_g} R_L = v_{R,L}, \tag{B29}$$

$$-i\omega C_g v_m^A = i_{C_g}, \tag{B30}$$

$$-i\omega C_v\left(v_m^A\right)v_m^A = i_{C_v}, \tag{B31}$$

$$-i\omega C_2\left(v_m^A - v_{m-1}^B\right) = i_{C_2}, \tag{B32}$$

$$-i\omega C_1\left(v_m^A - v_m^B\right) = i_{C_1}. \tag{B33}$$

The Kirchhoff's current law is also valid in the frequency domain with $i_{C_1} + i_{C_2} + i_{C_g} + i_{L_g} + \eta i_{C_v} = \frac{f_m^A - v_n^A}{R}$. Then we have

$$\begin{aligned} &-i\omega C_1\left(v_m^A - v_m^B\right) - i\omega C_2\left(v_m^A - v_{m-1}^B\right) - i\omega C_g v_m^A \\ &+ \frac{v_m^A}{-i\omega L_g + R_L} - i\omega\eta C_v\left(v_m^A\right)v_m^A = \frac{f_m^A - v_m^A}{R}, \end{aligned} \tag{B34}$$

and the equation can be rewritten as

$$-\mathrm{i}\omega\left[C_1+C_2+C_\mathrm{g}+\eta C_v\left(v_m^\mathrm{A}\right)\right]v_m^\mathrm{A}+\frac{v_m^\mathrm{A}}{-\mathrm{i}\omega L_\mathrm{g}+R_L}+\frac{v_m^\mathrm{A}}{R}+\mathrm{i}\omega C_1 v_m^\mathrm{B}+\mathrm{i}\omega C_2 v_{m-1}^\mathrm{B}=\frac{f_m^\mathrm{A}}{R}. \tag{B35}$$

Similarly, the equation for v_m^B is

$$-\mathrm{i}\omega\left[C_1+C_2+C_\mathrm{g}+\eta C_v\left(v_m^\mathrm{B}\right)\right]v_m^\mathrm{B}+\frac{v_m^\mathrm{B}}{-\mathrm{i}\omega L_\mathrm{g}+R_L}+\frac{v_m^\mathrm{B}}{R}+\mathrm{i}\omega C_1 v_m^\mathrm{A}+\mathrm{i}\omega C_2 v_{m+1}^\mathrm{A}=\frac{f_m^\mathrm{B}}{R}. \tag{B36}$$

The circuit equations can be further rewritten as

$$\omega\left[C_1+C_2+C_\mathrm{g}+\eta C_v\left(v_m^\mathrm{A}\right)\right]v_m^\mathrm{A}-\frac{\omega L_g}{\omega^2L_\mathrm{g}^2+R_L^2}v_m^\mathrm{A}+\mathrm{i}\frac{R_L}{\omega^2L_\mathrm{g}^2+R_L^2}v_m^\mathrm{A}+\frac{\mathrm{i}}{R}v_m^\mathrm{A}-\omega C_1 v_m^\mathrm{B}-\omega C_2 v_{m-1}^\mathrm{B}=\frac{\mathrm{i}}{R}f_m^\mathrm{A}, \tag{B37}$$

$$\omega\left[C_1+C_2+C_\mathrm{g}+\eta C_v\left(v_m^\mathrm{B}\right)\right]v_m^\mathrm{B}-\frac{\omega L_\mathrm{g}}{\omega^2L_\mathrm{g}^2+R_L^2}v_m^\mathrm{B}+\mathrm{i}\frac{R_L}{\omega^2L_\mathrm{g}^2+R_L^2}v_m^\mathrm{B}+\frac{\mathrm{i}}{R}v_m^\mathrm{B}-\omega C_1 v_m^\mathrm{A}-\omega C_2 v_{m+1}^\mathrm{A}=\frac{\mathrm{i}}{R}f_m^\mathrm{B}. \tag{B38}$$

To normalize the equations, we multiply the above equations with ωL_g. The resulting new equations are

$$\omega^2L_\mathrm{g}(C_\mathrm{g}+\eta C_\mathrm{L}+C_1+C_2)v_m^\mathrm{A}+\omega^2L_\mathrm{g}\eta C_\mathrm{NL}\left(v_m^\mathrm{A}\right)v_m^\mathrm{A}-\frac{\omega^2L_\mathrm{g}^2}{\omega^2L_\mathrm{g}^2+R_L^2}v_m^\mathrm{A}+\mathrm{i}\frac{\omega L_\mathrm{g}R_L}{\omega^2L_\mathrm{g}^2+R_L^2}v_m^\mathrm{A}+\mathrm{i}\frac{\omega L_\mathrm{g}}{R}v_m^\mathrm{A}-\omega^2L_\mathrm{g}C_1v_m^\mathrm{B}-\omega^2L_\mathrm{g}C_2v_{m-1}^\mathrm{B}-\mathrm{i}\frac{\omega L_\mathrm{g}}{R}f_m^\mathrm{A}=0, \tag{B39}$$

$$\omega^2L_\mathrm{g}(C_\mathrm{g}+\eta C_\mathrm{L}+C_1+C_2)v_m^\mathrm{B}+\omega^2L_\mathrm{g}\eta C_\mathrm{NL}\left(v_m^\mathrm{B}\right)v_m^\mathrm{B}-\frac{\omega^2L_\mathrm{g}^2}{\omega^2L_\mathrm{g}^2+R_L^2}v_m^\mathrm{B}+\mathrm{i}\frac{\omega L_\mathrm{g}R_L}{\omega^2L_\mathrm{g}^2+R_L^2}v_m^\mathrm{B}+\mathrm{i}\frac{\omega L_\mathrm{g}}{R}v_m^\mathrm{B}-\omega^2L_\mathrm{g}C_1v_m^\mathrm{A}-\omega^2L_\mathrm{g}C_2v_{m+1}^\mathrm{A}-\mathrm{i}\frac{\omega L_\mathrm{g}}{R}f_m^\mathrm{B}=0. \tag{B40}$$

Similarly, we can also introduce the normalized frequency $\bar{\omega}=\omega/\omega_n$ into the circuit equations. From Eqs. (B39) and (B40), the first and second terms are related to the grounding capacitors, coupling capacitors, and varactor diodes. The third and fourth terms are related to the inductors, which includes both the inductance and series resistance of the inductors. The fifth term is related to the shunt resistors which are wired to the driving voltage sources. The sixth and seventh terms are related to the coupling capacitors. And the last term at the left of the equal sign is related to the driving voltage sources. Note that Eqs. (B39) and (B40) can also be used to study the mode properties of the nonlinear topological states, as long as we let $R=\infty$ and $R_L=0$. Thus, Eqs. (B39) and (B40) governs the steady states in the circuit lattices without any approximation and we can validate the results from the GP equation using the accurate nonlinear circuit model. In this paper, we primarily utilize the GP equation to investigate the nonlinear topological states, including the mode properties and excitations, because the mathematical form of GP equation is simple and GP equation has be widely studied in the field of nonlinear physics.

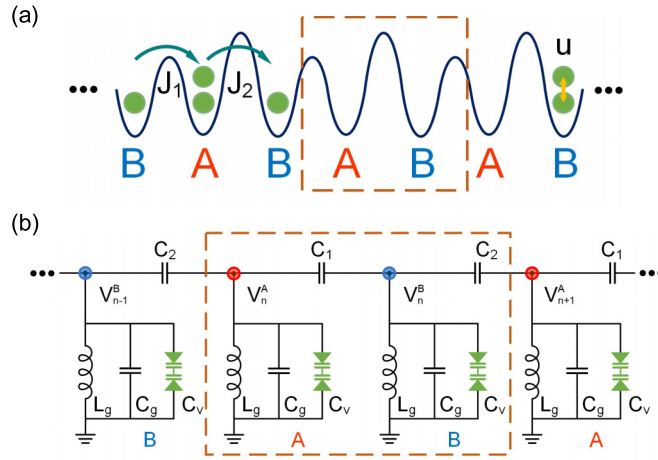

FIG. 9. Implementation of the interacting SSH lattice. (a) Many interacting bosons in an SSH lattice with the chemical potential E_0, tunneling coefficients $J_{1,2}$, and onsite interaction strength u. The red rectangle denotes one unit cell in the lattice. (b) Schematic of a nonlinear electric circuit lattice that emulates the interacting SSH lattice.

3. Interacting topological physics

Electric circuits have been proposed as a versatile platform to study the various topological phases in the noninteracting systems and few-body interacting systems. Due to the flexibility of constructing the circuit lattices and the site-resolved, phase-resolved, time-resolved, and frequency-resolved measurement techniques, electric circuits have shown significant values in exploring the high-dimensional, higher-order, non-Hermitian, non-Abelian and nonlinear topological physics. Specifically, by mapping the physical dimension to the particle number, electric circuits have been used to reveal the novel topological phases in few-body interacting systems [85]. This mapping faces a great challenge when the number of the interacting particles is large. However, the derivation of the GP equation provides a direct link between the many-body interacting systems and nonlinear electric circuits, and it is feasible to explore the many-body interacting topological physics in nonlinear circuit lattices.

As a minimal model featuring the interacting topological physics, we consider many interacting bosons in a dimerized SSH lattice, illustrated in Fig. 9(a). Each minimum of the potential corresponds to an individual site, which is called A or B. The bosons at sites A and B experience the same chemical potential E_0. Since the barriers between the sites have the different heights, the tunneling coefficients J_1 and J_2 are also different. A pair of particles occupying the same site experience an onsite interaction strength u, and the weak interactions between the particles from the neighbor sites are neglected. The Hamiltonian describing this system

reads

$$\begin{aligned}\hat{H} = & -J_1 \sum_m \left(c_m^{\mathrm{B}\dagger} c_m^{\mathrm{A}} + \mathrm{H.c.}\right) - J_2 \sum_m \left(c_{m+1}^{\mathrm{A}\dagger} c_m^{\mathrm{B}} + \mathrm{H.c}\right) \\ & + \frac{u}{2} \sum_m \left[n_m^{\mathrm{A}}\left(n_m^{\mathrm{A}} - 1\right) + n_m^{\mathrm{B}}\left(n_m^{\mathrm{B}} - 1\right)\right] \\ & + E_0 \sum_m \left(n_m^{\mathrm{A}} + n_m^{\mathrm{B}}\right), \end{aligned} \tag{B41}$$

where $c_m^{\sigma\dagger}$ and c_m^{σ} are the creation and annihilation operators for the particles at the site A ($\sigma = \mathrm{A}$) or B ($\sigma = \mathrm{B}$) of the lattice cell m, the summation enumerated with the index m is performed over all the cells in the lattice, H.c. denotes the Hermitian conjugate of the term to the left, and $n_m^{\sigma} = c_m^{\sigma\dagger} c_m^{\sigma}$ are the particle number operators. This Hamiltonian is the extended version of the Bose-Hubbard Hamiltonian [86]. Under the mean-field approximation, the macrooccupied state $|\Phi\rangle$ is chosen as the tensor product of the Glauber coherent states [87]. With $H = \langle\Phi|\hat{H}|\Phi\rangle$, the semiclassical Hamiltonian is

$$\begin{aligned} H = & -J_1 \sum_m \left(\psi_m^{\mathrm{B}*} \psi_m^{\mathrm{A}} + \mathrm{H.c.}\right) - J_2 \sum_m \left(\psi_{m+1}^{\mathrm{A}*} \psi_m^{\mathrm{B}} + \mathrm{H.c.}\right) \\ & + \frac{u}{2} \sum_m \left(\left|\psi_m^{\mathrm{A}}\right|^4 + \left|\psi_m^{\mathrm{B}}\right|^4\right) + E_0 \sum_m \left(\left|\psi_m^{\mathrm{A}}\right|^2 + \left|\psi_m^{\mathrm{B}}\right|^2\right). \end{aligned} \tag{B42}$$

Using the Hamiltonian's equation $\mathrm{i}\hbar\dot{\psi}_m^{\sigma} = \delta H/\delta\psi_m^{\sigma*}$, we get the discretized GP equation:

$$\begin{aligned} \mathrm{i}\hbar\frac{d}{dt}\begin{bmatrix}\psi_m^{\mathrm{A}} \\ \psi_m^{\mathrm{B}}\end{bmatrix} = & E_0\begin{bmatrix}\psi_m^{\mathrm{A}} \\ \psi_m^{\mathrm{B}}\end{bmatrix} - J_1\begin{bmatrix}\psi_m^{\mathrm{B}} \\ \psi_m^{\mathrm{A}}\end{bmatrix} - J_2\begin{bmatrix}\psi_{m-1}^{\mathrm{B}} \\ \psi_{m+1}^{\mathrm{A}}\end{bmatrix} \\ & + u\begin{bmatrix}\left|\psi_m^{\mathrm{A}}\right|^2\psi_m^{\mathrm{A}} \\ \left|\psi_m^{\mathrm{B}}\right|^2\psi_m^{\mathrm{B}}\end{bmatrix}. \end{aligned} \tag{B43}$$

This approach reduces a many-body interacting problem to the single-particle nonlinear one. The GP equation, also known as the nonlinear Schrödinger equation, provides a simplified treatment of the complex many-body systems.

Considering the GP equation for the nonlinear electric circuit lattices, Eqs. (B26) and (B27) can be rewritten as

$$\mathrm{i}\frac{d}{dt}\begin{bmatrix}V_m^{\mathrm{A}} \\ V_m^{\mathrm{B}}\end{bmatrix} = E_0\begin{bmatrix}V_m^{\mathrm{A}} \\ V_m^{\mathrm{B}}\end{bmatrix} + J_1\begin{bmatrix}V_m^{\mathrm{B}} \\ V_m^{\mathrm{A}}\end{bmatrix} + J_2\begin{bmatrix}V_{m-1}^{\mathrm{B}} \\ V_{m+1}^{\mathrm{A}}\end{bmatrix} + \begin{bmatrix}gV_m^{\mathrm{A}} \\ gV_m^{\mathrm{B}}\end{bmatrix}. \tag{B44}$$

Since Eq. (B43) describes the many interacting bosons in an SSH lattice and Eq. (B44) is mathematically equivalent to Eq. (B43), we can use the nonlinear circuit lattice shown in Fig. 9(b) to explore the many-body interacting topological physics in an SSH lattice. By comparing the two equations, the voltage at a circuit node corresponds to the wavefunction of the particles occupied at a lattice site. In Eq. (B44), the first term on the right side of the equal sign corresponds to the onsite potential term in Eq. (B43), and it only introduces an offset to the band structure. The coupling terms in Eq. (B44) correspond to the tunneling terms in Eq. (B43), and the coupling phases can be tuned by changing the coupling capacitors. The last term, which is a nonlinear term, is equivalent to the onsite interaction term in Eq. (B43). Although the nonlinear term for a circuit lattice exhibits the saturable nonlinearity, which is different to the cubic Kerr nonlinearity in Eq. (B43), this difference does not affect the topological physics that we study here. For an interacting system, the particle interaction leads to the increase or decrease of the effective onsite energy, depending on whether the particle interaction is attractive or repulsive [88]. While for the circuit lattice in Fig. 9(b), the interaction term always increases the onsite energy since the capacitance of the varactor diode decreases with an increasing voltage. Besides, in an interacting system the total particle number $N = \sum_m (n_m^A + n_m^B)$ is preserved but the interaction strength u may change, e.g., through the Feshbach resonance [89]. In a circuit lattice, the parameters C_{L}, ν_0, and M are fixed, but we can change the nonlinearity strength by tuning the voltages [59]. Consequently, under the slowly varying envelope approximation, the voltages for a circuit lattice composed of the coupled nonlinear LC oscillators are also governed by the GP equation. Due to the mathematical correspondence, it is feasible to explorer the many-body interacting topological physics in nonlinear electric circuits.

APPENDIX C: THEORETICAL RESULTS OF THE NONLINEAR TOPOLOGICAL EDGE STATES

In this Appendix, we give more theoretical results of the nonlinear topological edge states in the typical semi-infinite SSH lattice that ends with a weak bond [Fig. 1(a)].

Generally speaking, to calculate the frequencies and voltage distributions of the localized states in the nonlinear SSH circuit lattices, we solve the GP equation [i.e., Eq. (B44)] using the ansatz $V_m^{\mathrm{A,B}} = v_m^{\mathrm{A,B}} \exp(-\mathrm{i}\omega t)$. We employ Newton's method to solve the eigenvalue equation for each ω. Open boundary conditions are used to truncate the nonlinear circuit lattice. For the calculation of the nonlinear topological edge states, the linear topological edge states with scaling factors are taken as initial guesses. To calculate the topological gap solitons, self-induced topological edge states, and other topologically trivial solitons, we employ the anti-continuum (AC) approach. Once we obtain the soliton solution at a given ω, solutions at other frequencies can be obtained iteratively. The stability of the nonlinear states is analyzed using the standard linear stability technique and subsequently confirmed through temporal evolution based on the Runge-Kutta algorithm.

The excitation spectra are calculated by solving the driven-dissipative GP equaiton [i.e., Eqs. (B17) and (B24)]. Dissipation is characterized by γ at the input node and γ_L at the other nodes. Newton's method is employed to find the complex solutions. We calculate the voltage distributions at two frequencies away from the resonant frequencies, and use these solutions as initial guesses to obtain the entire spectrum. Finally, for a fixed driving voltage, we obtain two voltage spectra: one curve is obtained by increasing the driving frequency, while the other corresponds to a frequency sweep in the opposite direction. The bistable response can be observed by comparing the two voltage spectra.

In the theoretical calculation of the mode properties of the nonlinear topological edge states, we consider an SSH lattice with $N = 120$ unit cells, i.e., 240 sites. In the linear limit, the linear topological edge states residing at the opposite two

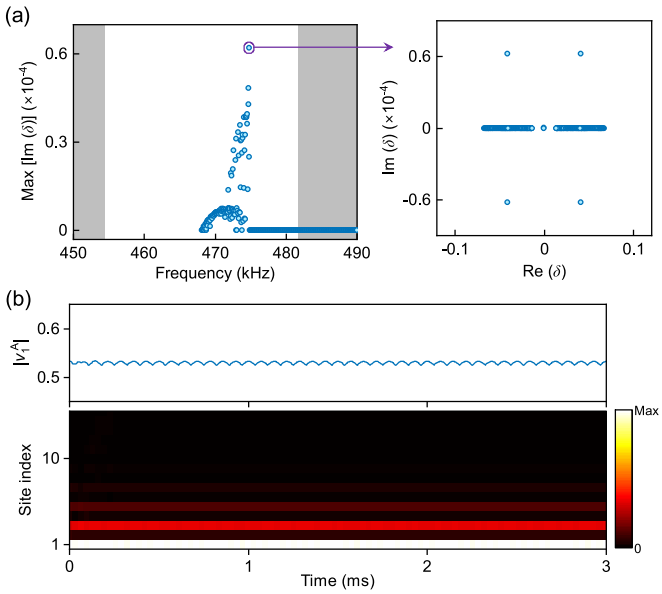

FIG. 10. Stability analysis of the nonlinear topological edge states. (a) The maximum growth rates of the perturbed solutions of the nonlinear topological edge states. The gray areas denote the linear bulk bands. The inset shows the linear stability spectrum at the frequency which has the largest Max[Im(δ)]. (b) The temporal evolution of the nonlinear topological edge state which has the largest Max[Im(δ)] [indicated in panel (a)]. Noises with $\pm 5\%$ random perturbations are added to the initial input.

edges are decoupled, thereby avoiding the finite size effect. For simplicity, we only study the nonlinear topological edge states that reside at the left edge of the lattice.

We then study the stability analysis of the nonlinear topological edge states. Figure 10(a) shows the maximum growth rates at the different frequencies of the nonlinear topological edge states. From the figure, the maximum growth rates are in the order of 10^{-5}, implying that the nonlinear topological edge states can be considered linearly stable. We further find the frequency which has the largest Max[Im(δ)] and plot the linear stability spectrum in the inset of Fig. 10(a). Compared with the real parts of δ, the imaginary parts are negligible. Thus, at least within the experimental measurement period, the nonlinear topological edge states do not exhibit the instability, such as the exponential increase or significant oscillation. To confirm the results from the linear stability analysis, we further add the noises with $\pm 5\%$ random perturbations to the amplitude of the nonlinear topological edge state which has the largest Max[Im(δ)], and study the temporal evolution. From the voltage distribution and edge voltage shown in Fig. 10(b), the nonlinear topological edge state is stable at least up to 3 ms.

APPENDIX D: EXPERIMENTAL MEASUREMENT OF THE NONLINEAR TOPOLOGICAL EDGE STATES

In this Appendix, we give more experimental results of the nonlinear topological edge states in the typical semi-infinite SSH lattice that ends with a weak bond [Fig. 1(a)].

Generally speaking, to ensure the observation of the nonlinear topological states, the circuit components should have minimal parasitic parameters, and their tolerance should be as low as possible. For this purpose, we utilize capacitors with low ESL and $\pm 1\%$ tolerance. We also employ inductors with magnetic shielding and low DCR (SPM12565VT-150M-D), and delicately select the components using an LCR meter (HIOKI IM3536). After performing Monte Carlo simulations, the tolerance for the inductance of the magnetically shielded inductors is set to $\pm 1\%$. Although the series resistance of these inductors increases with higher frequencies, we maintain the tolerances for series resistance at $\pm 2\%$ across all frequencies of interest in our study (see error analysis in Appendix F 3). Our measurements indicate that the average series resistance of the magnetically shielded inductors is approximately 600 mΩ. It is important to note that our measurements were conducted under a fixed current, and the series resistance of the inductors increases with larger currents. To characterize the voltage response of varactor diodes (BB201), we measure the C-V curves and the parameters C_{L}, v_0, and M are obtained by fitting these curves with the phenomenological formula. We use standard PCB techniques to fabricate the lattice, ensuring that the inductors are sufficiently spaced to prevent mutual coupling. The PCB traces have a relatively large width of 0.75 mm to accommodate high currents, and the layouts are carefully optimized to minimize parasitic parameters and coupling with other circuit components.

To excite the circuit lattices, SubMiniature version A (SMA) connectors are soldered onto the PCB for signal injection. Since the output voltage of an arbitrary function generator (Tektronix AFG31022) is typically low, we use a high-voltage amplifier (Aigtek ATA-2022B) to amplify the voltage signals. The amplified voltage signals are then injected into the circuit sample through the SMA connectors. Note that the leakage current of the high-voltage amplifier is negligible compared to the operating current of the circuit sample. Due to bandwidth limitations, the output voltage of the high-voltage amplifier may fall below the preset value at high operating frequencies. Additionally, the two channels of the high-voltage amplifier may not provide strictly equal amplification factors. To detect the voltage signals at the circuit nodes, custom connectors on the PCB are connected to an oscilloscope (Tektronix MDO34). For the excitation spectrum measurement, we fix the input voltage and conduct program-controlled frequency sweeps, during which the voltage signals at the circuit nodes are recorded.

To theoretically demonstrate the excitation and observation of the nonlinear topological edge states, we first solve the driven-dissipative GP equation with the driven terms $F_m^{\mathrm{A}}(t) = \delta_{m,1} f_0^{\mathrm{A}} \exp(-\mathrm{i}\bar{\omega}T)$ and $F_m^{\mathrm{B}}(t) = 0$, i.e., only the edge site is excited. Then the equations are numerically solved by following the same procedure. To experimentally observe the nonlinear topological edge states, we excite the leftmost edge site with the external driving voltage f_1^{A}. Similarly, the dissipations induced both from the series resistance of the inductors and shunt resistors are considered. Figure 11(a) schematically shows the nonlinear SSH lattice with the nearest neighbor couplings $J_{1,2}$, the dissipations γ_L and γ, and the external driving voltage f_1^{A}. In the linear limit, this lattice is a topologically nontrivial lattice since $J_1 < J_2$. Figure 11(b) shows the fabricated PCB of the driven-dissipative nonlinear circuit lattice, and the inset shows the enlarged figure with

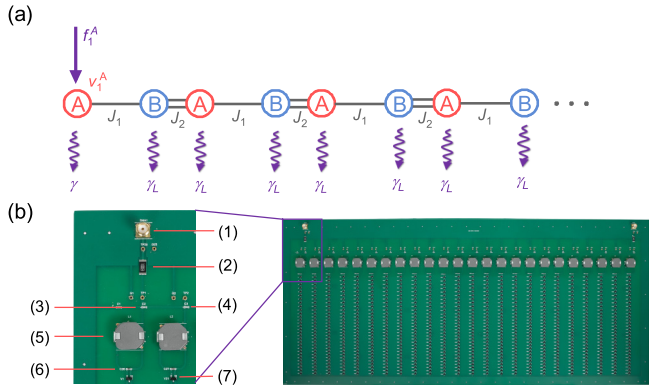

FIG. 11. Experimental implementation of the SSH lattice which is topologically nontrivial in the linear limit [Fig. 1(a)]. (a) Schematic of the nonlinear SSH lattice which is topologically nontrivial in the linear limit. The external driving voltage is f_1^{A} and the voltage at the edge node is v_1^{A}. (b) Fabricated PCB of the driven-dissipative nonlinear circuit lattice with the enlarged figure showing the circuit components: (1) SMA connector, (2) shunt resistor R, (3) coupling capacitor C_1, (4) coupling capacitor C_2, (5) grounding inductor L_{g}, (6) grounding capacitor C_{g}, and (7) varactor diode C_{v}.

the circuit components: (1) SMA connector, (2) shunt resistor R, (3) coupling capacitor C_1, (4) coupling capacitor C_2, (5) grounding inductor L_{g}, (6) grounding capacitor C_{g}, and (7) varactor diode C_{v}. The SMA connector is connected to an external voltage source with the voltage amplitude f_1^{A}. Here, the experimental circuit lattice consists of $N = 12$ unit cells. We determine this value of N by noting that the voltage spectra for lattices with $N = 12$ and $N = 120$ are identical (for example, see the discussion on nonlinear topological interface states in Appendix F 3).

Experimentally, by following the same procedure in the observation of the nonlinear topological interface states (see Appendix F), we excite and observe the nonlinear topological edge states in the SSH lattice which is topologically nontrivial in the linear limit. Figure 12 shows the voltage spectra at the edge node when the circuit is excited with the driving voltage f_1^{A}. The first and second rows show the experimental and theoretical results, respectively. The directions of frequency sweep are denoted by the blue and orange arrows. From the first column, when the driving voltage is small with $f_1^{\mathrm{A}} = 1$ V, the voltage spectra for the frequency sweeps along the two opposite directions coincide with each other. The symmetric peaks exhibited by the voltage spectra are the signature of the excitation of the linear topological edge state in the linear limit. With the increasing of the driving voltage, the spectrum peaks become asymmetric with respect to the resonant frequency and the resonant frequency increases, as shown by the figures in the second and third columns. When the driving voltage is large enough, the spectrum peaks become highly asymmetric and exhibit the bistable response. From the fourth column where the driving voltage is $f_1^{\mathrm{A}} = 90$ V, the voltage spectra for the frequency sweep along the two opposite directions are no longer coincide with each other and we observe the bistable response which is induced by the nonlinear topological edge state in an SSH lattice which is topologically nontrivial in the linear limit [i.e., in the nonlinear SSH lattice shown in Fig. 1(a)]. Note that in the theoretical calculation, we set $N = 120$, indicating that the lattice consists of 120 unit cells.

To quantitatively study the properties of the nonlinear topological edge states, we measure the voltage distributions at the resonant frequencies of the voltage spectra. The nonlinear topological edge states are all mainly confined to the sublattice site A of the unit cells, and the phase jump of π among the neighboring cells still holds. For larger driving voltages, the nonlinear topological edge states exhibit the decreased sublattice pseudospin S, agreeing well with the theoretical prediction. Meanwhile, the localization of the nonlinear topological edge states decreases. These properties are confirmed by the results shown in Fig. 13. From Fig. 13(a), in the linear limit, the frequency of the nonlinear topological edge state resides in the middle of the SSH bandgap. With the increasing of the circuit nonlinearity, the frequency of the nonlinear edge state exhibits a blue shift, similar to the phenomenon observed for the nonlinear topological interface states (see Appendix F). From Fig. 13(b), with the increasing

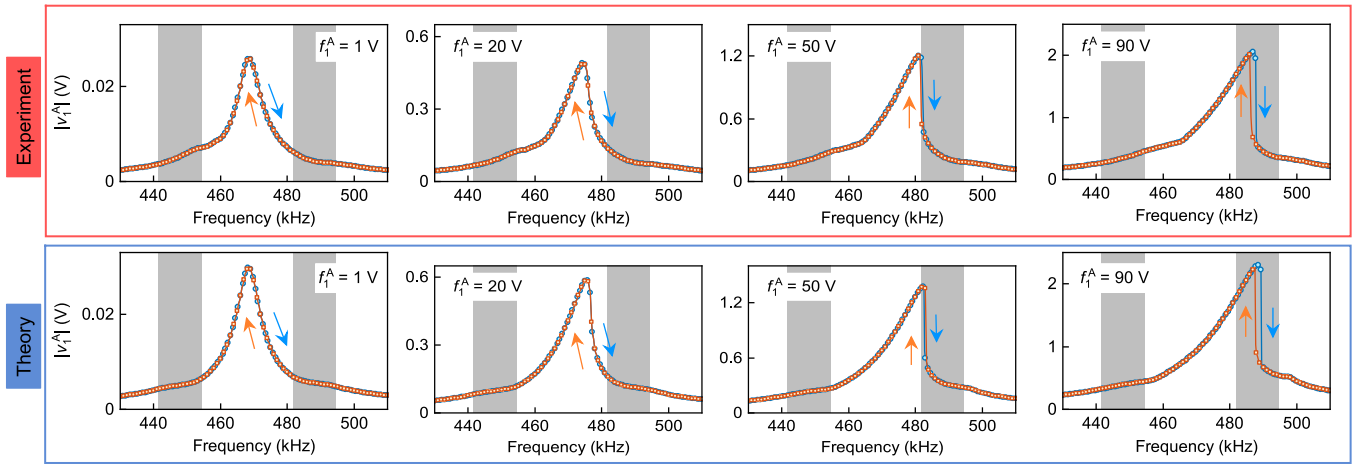

FIG. 12. Voltage spectra at the edge node when the circuit is excited with the driving voltage f_1^{A}. The first and second rows show the results from the experiment and GP equation, respectively. In both rows, the blue and orange curves correspond to the frequency sweeps along the two opposite directions (denoted by the blue and orange arrows). The gray areas correspond to the linear bulk bands.

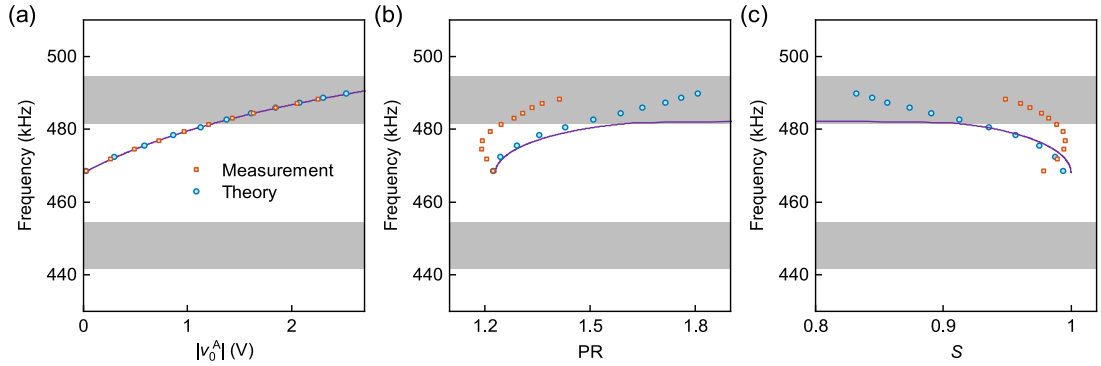

FIG. 13. Edge voltages $|v_1^A|$, participation ratios (PRs), and sublattice polarizations S of the nonlinear topological edge states. The orange squares and blue circles correspond to the experimental and theoretical results, respectively. The purple curves denote the result calculated from the GP equation without the driven-dissipative terms, and the gray areas correspond to the linear bulk bands.

of the onsite nonlinearity, the localization of the nonlinear topological edge state becomes weak. The deviations between the experimental and theoretical values are due to the circuit dissipation and measurement errors. Figure 13(c) shows the dependence between the frequency and sublattice pseudospin of the nonlinear topological edge states. The experimental and theoretical frequencies correspond to the resonant frequencies of the voltage spectra under the external voltage driving. The purple curve denotes the result calculated from the GP equation without the driven-dissipative terms. From the figure, the behaviors of the nonlinear topological edge states are very similar to those of the nonlinear topological interface states (see Appendix F). In the linear limit, we have $S \approx 1$ for both the experimental and theoretical results. These results agree with the prediction from the GP equation without the driven-dissipative terms. For a larger driving voltage, i.e., for a larger frequency, the nonlinear topological edge state exhibits a decreased sublattice pseudospin S. The experimental result deviates from the theoretical data because of the increased circuit dissipation and decreased driving voltage. The small discrepancy near the linear limit is due to the inaccuracy of the measurement data recorded by the oscilloscope.

APPENDIX E: THEORETICAL RESULTS OF THE NONLINEAR TOPOLOGICAL INTERFACE STATES

In this Appendix, we give more theoretical results of the nonlinear topological edge states in the structure connected by two lattices with the different topological properties in the linear limit. Since the nonlinear topological edge states reside at the interface, we simply call them nonlinear topological interface states for clarity. This section is organized as follows. In the first subsection, we introduce the procedure to find the nonlinear topological interface states and discuss their properties. Then we study the stability analysis of the nonlinear topological interface states. In the last subsection, we discuss the nonlinear topological trivial interface states.

1. Existence of the nonlinear topological interface states

We focus on the lattice configuration shown in Fig. 1(b). This configuration can be treated as an SSH lattice with an interface defect at the center. The chain has N unit cells for the left topologically trivial part with the intracell coupling larger than the intercell coupling, and $N + 1/2$ unit cells for the right nontrivial part with the intracell coupling smaller than the intercell coupling. To avoid the finite size effect, here we let $N = 60$ and there are 241 lattice sites (circuit nodes) in total. Based on Eqs. (B26) and (B27), we can get the governing equations of all the lattice sites and solve the equations using Newton's method. For the nonlinear topological interface states which bifurcate from the linear topological interface state, we take the linear topological interface state as the initial guess solution. To find the nonlinear topologically trivial interface states which are conventional lattice solitons localized at the interface, we solve the GP equation using the AC approach. In the AC limit, we have $C_1 = 0$ and Eqs. (B26) and (B27) reduce to

$$E_0 + g\left(v_0^A\right) = \bar{\omega}, \tag{E1}$$

where

$$E_0 = \left[1 - \frac{C_2}{2(C_g + \eta C_L)}\right]\frac{\omega_0}{\omega_n}, \tag{E2}$$

$$g\left(v_0^A\right) = -\frac{\eta C_{NL}\left(v_0^A\right)}{2(C_g + \eta C_L)}\frac{\omega_0}{\omega_n}. \tag{E3}$$

After solving this equation, we get the value of v_0^A. Then we seek for the solutions for the nonlinear topologically trivial interface states by gradually increasing C_1 to the original value. Meanwhile, since the GP equation is derived under the slowly varying approximation, to validate the existence of the nonlinear topologically trivial interface states, we also seek for the solutions for the nonlinear topologically nontrivial and trivial interface states based on the accurate nonlinear circuit model. Equations (B39) and (B40) with $R = \infty$ and $R_L = 0$ are numerically solved using Newton's method with the suitable initial guess solutions. The calculation results from the GP equation and circuit model are shown in Fig. 14.

Figure 14(a) shows the frequencies of the nonlinear topological interface states. The blue and red curves correspond to the results calculated from the GP equation and circuit model, respectively, and the shaded regions denote the linear bulk bands. We define $P = \sum_m (|v_m^A|^2 + |v_m^B|^2)$ as the equivalent power in the circuit lattice to measure the strength of nonlinearity. From the figure, the results from the GP equation and

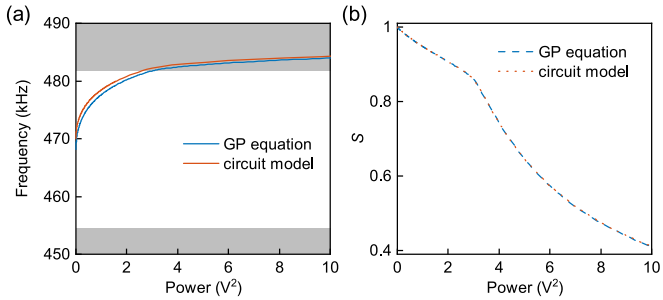

FIG. 14. Nonlinear topological interface states. (a) Eigenfrequencies of the nonlinear topological interface states calculated from the GP equation and circuit model. The gray areas correspond to the linear bulk bands. (b) Sublattice pseudospin of of the nonlinear topological interface states indicated in panel (a).

circuit model agree well with each other. Figure 14(b) further shows the sublattice pseudospin of the nonlinear topological interface states. In the linear limit, the topological interface states are perfectly localized on the sublattice site A with $S = 1$. This property can be revealed from the solution of the GP equation. With $g = 0$ and $V_m^{\mathrm{A,B}}(T) = v_m^{\mathrm{A,B}} e^{-i\bar{\omega}T}$, the governing equations reduce to

$$\ldots, \tag{E4}$$

$$\bar{\omega} v_{-1}^{\mathrm{B}} = E_0 v_{-1}^{\mathrm{B}} + J_2 v_{-1}^{\mathrm{A}} + J_1 v_0^{\mathrm{A}}, \tag{E5}$$

$$\bar{\omega} v_0^{\mathrm{A}} = E_0 v_0^{\mathrm{A}} + J_1 v_0^{\mathrm{B}} + J_1 v_{-1}^{\mathrm{B}}, \tag{E6}$$

$$\bar{\omega} v_0^{\mathrm{B}} = E_0 v_0^{\mathrm{B}} + J_1 v_0^{\mathrm{A}} + J_2 v_1^{\mathrm{A}}, \tag{E7}$$

$$\ldots, \tag{E8}$$

where the interface defect is located at the site A of the 0th cell. Since the linear topological interface state has $\bar{\omega} = E_0$, the voltage distribution satisfies $v_m^{\mathrm{A}} = (-\frac{J_1}{J_2})^{|m|} v_0^{\mathrm{A}}$ and $v_m^{\mathrm{B}} = 0$. With the increasing of the power, S decreases implying that the site B has the nonzero voltages. Besides, the results from the GP equation and circuit model shown in Fig. 14(b) again agree well with each other.

2. Stability analysis of the nonlinear topological interface states

We study the dynamical stability/instability of the nonlinear topological interface states. The stability or instability of nonlinear states and solitons is crucial. Typically, under initial excitation, only stable solitons can be effectively excited and observed after a period of temporal evolution. For a general nonlinear SSH circuit lattice, the linear stability/instability of the nonlinear states can be evaluated by substituting the following perturbed solutions

$$V_m^{\mathrm{A}} = e^{-i\bar{\omega}T}\left(v_m^{\mathrm{A}} + \varepsilon_m^{\mathrm{A}} e^{-i\delta T} + \mu_m^{\mathrm{A}*} e^{i\delta^* T}\right), \tag{E9}$$

$$V_m^{\mathrm{B}} = e^{-i\bar{\omega}T}\left(v_m^{\mathrm{B}} + \varepsilon_m^{\mathrm{B}} e^{-i\delta T} + \mu_m^{\mathrm{B}*} e^{i\delta^* T}\right), \tag{E10}$$

into Eqs. (B26) and (B27) and performing a standard linearization procedure. In Eqs. (E9) and (E10), $v_m^{\mathrm{A,B}} e^{-i\bar{\omega}T}$ are the unperturbed solutions of the nonlinear topological interface states, $\varepsilon_m^{\mathrm{A,B}}$ and $\mu_m^{\mathrm{A,B}}$ are the infinitesimal amplitudes of the perturbations, and δ is the eigenfrequency. Obviously, the nonlinear topological interface states are linearly stable if δ is real, and they are linearly unstable if the imaginary part of δ, namely the growth rate, is positive. After solving the linearized equations regarding to $\varepsilon_m^{\mathrm{A,B}}$ and $\mu_m^{\mathrm{A,B}}$, we can get the maximum growth rates, i.e., Max[Im(δ)], at the different powers or frequencies. For simplicity, we let $\omega_n = \omega_0$ in the calculations and the growth rates are thus normalized. Figure 15(a) shows the maximum growth rates at the different frequencies of the nonlinear topological interface states. From the figure, the maximum growth rates are in the order of 10^{-4}, implying that the nonlinear topological interface states can be considered linearly stable. We further find the frequency which has the largest Max[Im(δ)] and plot the linear stability spectrum in the inset of Fig. 15(a). Compared with the real parts of δ, the imaginary parts are negligible. Thus, at least within the experimental measurement period, the nonlinear topological interface states do not exhibit the instability, such as the exponential increase or significant oscillation. To confirm the results from the linear stability analysis, we further add the noises with ±5% random perturbations to the amplitude of the nonlinear topological interface state which has the largest Max[Im(δ)], and study the temporal evolution. From the voltage distribution and interface voltage shown in Fig. 15(b), the nonlinear topological interface state is stable at least up to 3 ms.

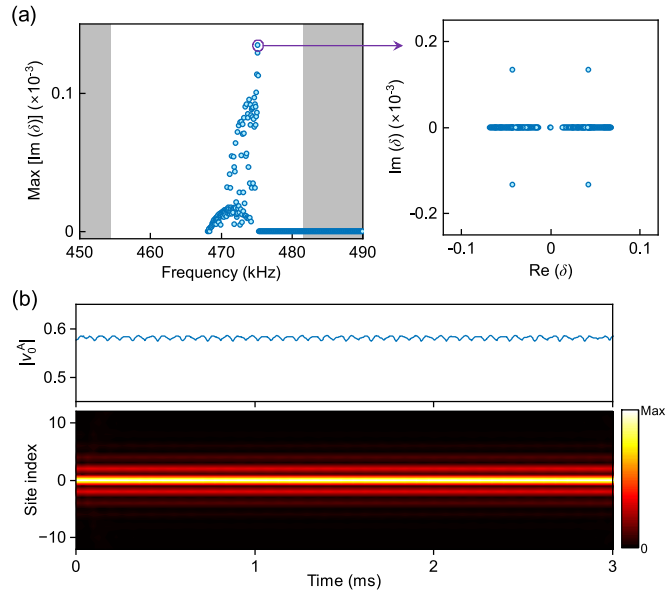

FIG. 15. Stability analysis of the nonlinear topological interface states. (a) The maximum growth rates of the perturbed solutions of the nonlinear topological interface states. The gray areas denote the linear bulk bands. The inset shows the linear stability spectrum at the frequency which has the largest Max[Im(δ)]. (b) The temporal evolution of the nonlinear topological interface state which has the largest Max[Im(δ)] [indicated in panel (a)]. Noises with ±5% random perturbations are added to the initial input.

3. Nonlinear topologically trivial interface states

Here we discuss the nonlinear topologically trivial interface states. Usually, when the nonlinearity dominates the intracell and intercell couplings, the conventional lattice solitons appear. However, in this circuit lattice such kind of

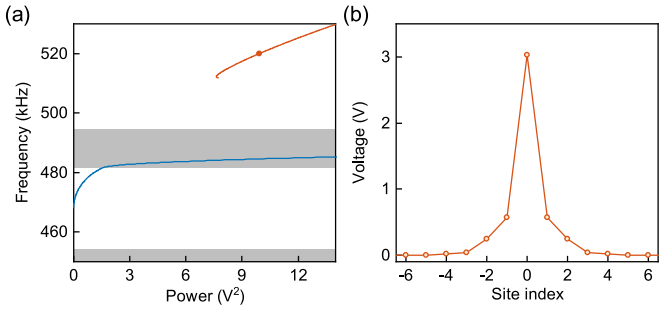

FIG. 16. Nonlinear interface states in a circuit lattice with the nonsaturable nonlinearity. (a) Frequencies of the nonlinear interface states, where the topologically nontrivial and trivial states are denoted by the blue and red curves, respectively. The gray areas correspond to the linear bulk bands. (b) Voltage distribution of the nonlinear topologically trivial interface state with its frequency at 520 kHz [marked by the dot in panel (a)].

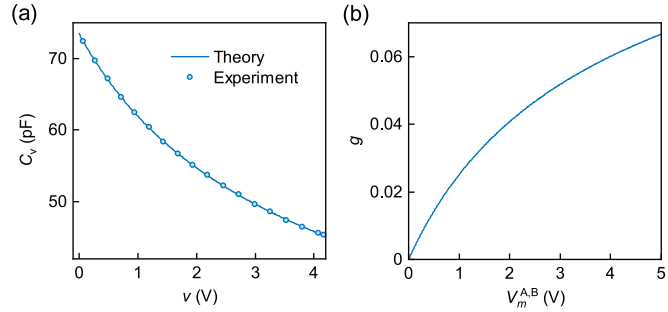

FIG. 17. Nonlinearity of the circuit lattice. (a) The capacitance of a back-to-back varactor diode, where the circles are the experimental measurement data and the solid curve is calculated from the theoretical formula with the fitting parameters. (b) The voltage dependent onsite energy.

nonlinear topologically trivial interface states do not exist, because the capacitance of the varactor diodes saturates and the circuit lattice can not provide enough nonlinearity to support the existence of such states. For comparison, we calculate the nonlinear interface states of a nonsaturable circuit model where the capacitance of the varactor diodes is characterized by Eq. (A7), and the results are shown in Fig. 16. From Fig. 16(a), the nonlinear topological interface states exist as well (blue curve), and their frequencies exhibit the blue shift more obviously than the frequencies of the nonlinear topological interface states in the circuit lattice with the saturable nonlinearity. Besides, in the nonsaturable model, the nonlinear topologically trivial interface states emerge in the upper semi-infinite gap (denoted as red curve). In Fig. 16(b), we plot the voltage distribution of the nonlinear topologically trivial interface state with its frequency at 520 kHz. Since the nonlinear topologically trivial interface state is an self-sustained state and emerges when the nonlinearity dominates the couplings, the state is confined to both the sublattice sites A and B, and there is no phase jump among the neighboring cells or sites.

APPENDIX F: EXPERIMENTAL MEASUREMENT OF THE NONLINEAR TOPOLOGICAL INTERFACE STATES

In this Appendix, we give more experimental results of the nonlinear topological edge states in the structure connected by two lattices with different topological properties in the linear limit [Fig. 1(b)]. Since the nonlinear edge states reside at the interface, we simply call them nonlinear topological interface states for clarity. This section is organized as follows. In the first two subsections, we introduce the experimental principle and show the experimental result for the linear SSH lattice, respectively. Then we discuss the experimental measurement of the nonlinear topological interface states in the third subsection.

1. Experimental principle

The GP equations [Eq. (1) or Eqs. (B26) and (B27)] describe the circuit lattices without the external sources and circuit dissipation. However, in the realistic experiments, the circuit lattice has to be excited by an external source and the circuit itself is inherently lossy. For a linear topological circuit, we usually excite the circuit using a continuous voltage source and measure the voltage distributions at the circuit nodes. The band structure and topological states can be obtained using this measurement technique [90]. However, this technique can not be directed extended to study the nonlinear topological states in the nonlinear topological circuits because of the two reasons. First, the response of a nonlinear system is sensitive to the external excitation and the complicated bistable behavior may emerge in the nonlinear system. Second, when a nonlinear system is driven by a continuous source, the dissipation of the system has to be considered, otherwise the steady states are not supported. Taking these factors into account, we use the discretized driven-dissipative GP equation, i.e., Eqs. (B17) and (B24), to study the excitation of the nonlinear topological states and compare the theoretical results with the experimental ones.

In this study, for the typical SSH lattice with the intracell coupling smaller than the intercell coupling [Fig. 1(a)], the circuit parameters are $L_g = 15$ μH, $C_g = 4.7$ nF, $C_1 = 180$ pF, and $C_2 = 560$ pF. The parameters of the varactor diodes are $C_L = 73.48$ pF, $v_0 = 2.1935$, and $M = 0.4548$, which are obtained by fitting the experimental measurement results. Under these parameters, we have $J_1 < J_2$. Figure 17(a) shows the capacitance-voltage curve of a back-to-back varactor diode, where the measurement frequency is 500 kHz. Since the capacitance decreases with an increasing voltage, the onsite nonlinearity g increases for large voltages at the circuit nodes [Fig. 17(b)]. Here we use 30 back-to-back varactor diodes, i.e., $\eta = 30$. Although the varactor diodes exhibit the saturable nonlinearity, the capacitance does not reach saturation within our experimental voltage range. Besides, the shunt resistors connected to the external voltage sources are $R = 100$ kΩ, and the series resistance of the inductors are $R_L = 600$ mΩ. These parameters ensure the validity of the GP equations, both with and without the driven-dissipative terms. Meanwhile, for all circuit samples, our experimental measurements indicate that the maximum impedance between the excitation node and ground is 2.8 kΩ. Therefore, the voltage source, combined with the shunt resistor, can be treated as an equivalent current source. Note that to quantitatively

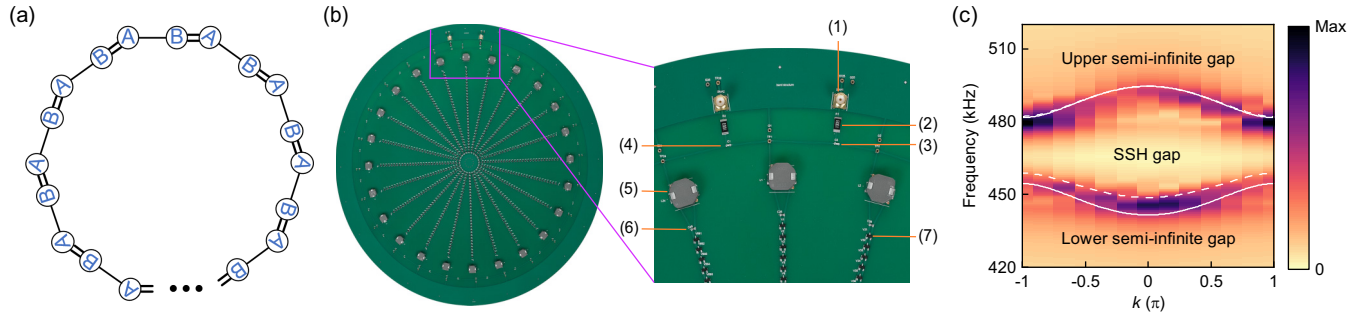

FIG. 18. Band structure for a linear SSH circuit lattice. (a) Schematic of the linear SSH lattice with the periodic boundary condition. (b) Fabricated PCB of the circuit lattice. The inset shows the enlarged figure with the circuit components: (1) SMA connector, (2) shunt resistor R, (3) coupling capacitor C_1, (4) coupling capacitor C_2, (5) grounding inductor L_g, (6) grounding capacitor C_g, and (7) varactor diode C_v. (c) Experimentally measured band structure. For comparison, the band structures calculated from the GP equation and circuit model are also plotted in sold and dashed white curves, respectively.

test the validity of the GP equations, we have also checked the results using the accurate nonlinear circuit model without the slowly varying envelope approximation. The comparison shows that the nonlinear topological states in the nonlinear topological circuit lattices can be effectively captured by the GP equation.

2. Linear SSH lattice

Before we study the nonlinear topological states, we implement an SSH circuit lattice with the periodic boundary condition and measure the linear band structure. The study of the linear SSH lattice is important because of the two reasons. First, we validate the GP equation by comparing the theoretical result with the experimental data. If the results from the GP equation, nonlinear circuit model, and experimental measurement agree with each other, then the validity of the GP equation is well proved, at least in the linear limit. Second, we need to get the experimental frequency gap in the linear limit before we study the nonlinear topological states. Due to the experimental errors, there may be a frequency offset between the experimental gap and theoretically predicted range. The prior knowledge of the experimental result in the linear limit is helpful for the physical explanation of the nonlinear states, including both the topologically nontrivial and trivial ones.

The nonlinear SSH circuit lattice reduces to the linear limit when the external driving voltage is small. In this limit, the varactor diodes act as the normal capacitors, and the circuit lattice is described by the single-particle SSH Hamiltonian which leads to two bulk bands with a topological bandgap between them [58]. We start from Eqs. (B26) and (B27) with $g = 0$. Under the periodic boundary condition, the solutions are in the form of the Bloch functions $V_m^{\mathrm{A,B}} = \phi_{\mathrm{A,B}} \exp(\mathrm{i}km - \mathrm{i}\bar{\omega}T)$ and the normalized frequencies are calculated as

$$\bar{\omega} = E_0 \pm \sqrt{J^2 + J'^2 + 2JJ' \cos k}. \tag{F1}$$

Then we calculate the band structure based on the circuit model. Under the periodic boundary condition, Eqs. (B39) and (B40) with $g = 0$ can be written as

$$\begin{bmatrix} L_g(C_1 + C_2 + C_g + \eta C_L) & -L_g\,(C_1 + C_2 e^{-ik}) \\ -L_g(C_1 + C_2 e^{ik}) & L_g(C_1 + C_2 + C_g + \eta C_L) \end{bmatrix} \begin{bmatrix} \phi_A \\ \phi_B \end{bmatrix} = \frac{1}{\omega^2} \begin{bmatrix} \phi_A \\ \phi_B \end{bmatrix}, \tag{F2}$$

and the eigenfrequencies are

$$\omega = \Big[L_g(C_1 + C_2 + C_g + \eta C_L) \pm L_g \sqrt{C_1^2 + C_2^2 + 2C_1 C_2 \cos k} \Big]^{-\frac{1}{2}}. \tag{F3}$$

Equation (F3) reduces to Eq. (F1) under the approximation $C_{1,2} \ll C_g + \eta C_L$, and this implies that the GP equation is valid as long as the coupling capacitance is much smaller than the grounding capacitance.

To experimentally probe the band structure for a linear SSH lattice, we fabricate an end-to-end circuit lattice which satisfies the periodic boundary condition, as shown in Fig. 18(a). Since the circuit structure contains N unit cells (N is an even number and $N = 12$ is our experiment), k has N discrete values with $k = -\pi, -\frac{N-2}{N}\pi, \ldots, 0, \frac{N-2}{N}\pi$. The fabricated circuit sample is shown in Fig. 18(b). From the inset, two circuit nodes are wired to the shunt resistors R. In the experiment, we excite the circuit with $f_1^{\mathrm{A}} = 1$ V and $f_N^{\mathrm{B}} = 1$ V, respectively, by connecting the two SMA connectors to an arbitrary function generator. The complex voltages at all the circuit nodes are measured using an oscilloscope. Then by applying a Fourier transform and taking an average between the results from the sites A and B, we get the voltage distribution in k space, i.e., the band structure. The experimental band structure is shown in Fig. 18(c). For comparison, the theoretical band structure calculated from the GP equation and circuit model are also plotted in sold and dashed white curves, respectively. From the figure, besides the middle SSH gap, the band structure exhibits two semi-infinite gaps, one above the top band and the other one below the bottom band. The existence of the semi-infinite gaps are ensured because the LC oscillators are single mode and such property of topological

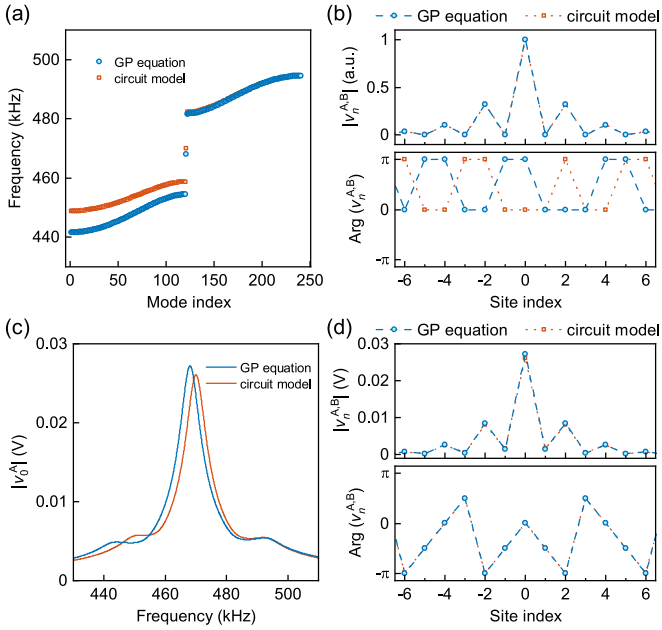

FIG. 19. Linear topological interface states. (a) Eigenfrequencies of the states in the linear SSH lattice, where the blue and orange symbols correspond to the results from the GP equation and circuit model, respectively. The middle frequencies correspond to the liner topological interface states. (b) The voltage amplitudes and phases of the linear topological interface states. (c) Voltage spectra of the linear SSH lattice when the driving voltage is $f_0^{\mathrm{A}} = 1$ V. The blue and orange curves correspond to the results from the GP equation and circuit model, respectively. (d) Amplitudes and phases of the voltage distributions at the respective resonant frequencies in panel (c).

circuits has be used in the observation of the complicated band degeneracies [90].

From Fig. 18(c), the theoretical band structure calculated from the GP equation and circuit model agree well with each other. Although there is a small discrepancy between the bottom bands, this discrepancy does not affect the nonlinear topological physics that we study in this paper. Meanwhile, the experimental band structure agrees well with the theoretical one. The comparison between the three results implies that the experimental observation of a linear SSH circuit lattice can be effectively described by the GP equation.

Based on the above result, we discuss the linear topological interface states and show that the linear topological interface states can be excited under the external driving voltage. First, we neglect the external driving and circuit dissipation, and study the linear topological interface state in a linear SSH lattice with $g = 0$. The circuit dissipation is also omitted. The right end of the lattice is truncated with $V_N^{\mathrm{B}} = 0$ to avoid the coupling between the interface state residing at the interface and the edge state residing at the right topologically nontrivial part. Here, we set $N = 60$, i.e., there are 60 unit cells for the left topologically trivial part and 60.5 unit cells for the right nontrivial part. Starting from the GP equation, we seek for the solutions with $V_m^{\mathrm{A,B}} = \psi_m^{\mathrm{A,B}} \exp(-\mathrm{i}\bar{\omega}T)$, and the normalized frequency $\bar{\omega}$ can be directly obtained. Note that it is also possible to study the linear topological interface state using the accurate circuit model. Figure 19(a) shows the eigenfrequencies of the linear SSH lattice, where the blue and orange symbols correspond to the results from the GP equation and circuit model, respectively. The middle frequencies correspond to the liner topological interface states and their voltage distributions are shown in Fig. 19(b). The linear interface states have the well-defined sublattice pseudospin with $S = 1$, and they exhibit the phase jump of π among the neighboring cells. Besides, in Figs. 19(a) and 19(b), the results from the GP equation well agree with the results from the circuit model. Then we study the excitation of the linear topological interface state based on the driven-dissipative GP equation. The dissipation is $\gamma = \gamma_L + \gamma_R$ at the driven node and γ_L at the other nodes. Similarly, we also study the excitation of the linear topological interface state based on the circuit model. Figure 19(c) shows the voltage spectra of the linear SSH lattice when the driving voltage is $f_0^{\mathrm{A}} = 1$ V, where the blue and orange curves correspond to the results from the GP equation and circuit model, respectively. The peaks of the voltage spectra are symmetric with respect to their respective resonant frequencies. We obtain the resonant frequencies from the voltage spectra and plot the voltage distributions at the resonant frequencies. From Fig. 19(d), the voltage distributions from the GP equation and circuit model both exhibit the sublattice pseudospin of $S = 0.99$ and the property of phase jump still holds. These features imply that, under the driving of the external voltage source, the linear topological interface states are excited at the resonant frequencies.

3. Nonlinear topological interface states

To theoretically demonstrate the excitation and observation of the nonlinear topological interface states, we first solve the driven-dissipative GP equation with the driven terms $F_m^{\mathrm{A}}(t) = \delta_{m,0} f_0^{\mathrm{A}} \exp(-\mathrm{i}\bar{\omega}T)$ and $F_m^{\mathrm{B}}(t) = 0$, i.e., only the interface site is excited. Since the solutions are generally complex-valued, we separate the real and imaginary parts of the solutions, and the new equations are solved using Newton's method. We then study the nonlinear circuit model with the driven-dissipative terms. Equations (B39) and (B40) can be rewritten as

$$(E_0 - i\gamma)v_m^{\mathrm{A}} + g\big(v_m^{\mathrm{A}}\big)v_m^{\mathrm{A}} + Jv_m^{\mathrm{B}} + J'v_{m-1}^{\mathrm{B}} + idf_m^{\mathrm{A}} = 0, \quad \text{(F4)}$$

$$(E_0 - i\gamma)v_m^{\mathrm{B}} + g\big(v_m^{\mathrm{B}}\big)v_m^{\mathrm{B}} + Jv_m^{\mathrm{A}} + J'v_{m+1}^{\mathrm{A}} + idf_m^{\mathrm{B}} = 0, \quad \text{(F5)}$$

where

$$E_0 = \omega^2 L_{\mathrm{g}}(C_{\mathrm{g}} + \eta C_{\mathrm{L}} + C_1 + C_2) - \frac{\omega^2 L_{\mathrm{g}}^2}{\omega^2 L_{\mathrm{g}}^2 + R_L^2}, \quad \text{(F6)}$$

$$\gamma = -\frac{\omega L_{\mathrm{g}} R_L}{\omega^2 L_{\mathrm{g}}^2 + R_L^2} - \frac{\omega L_{\mathrm{g}}}{R}, \quad \text{(F7)}$$

$$g\big(v_m^{\mathrm{A,B}}\big) = \omega^2 L_{\mathrm{g}} \eta C_{\mathrm{NL}}\big(v_m^{\mathrm{A}}\big), \quad \text{(F8)}$$

$$J = -\omega^2 L_{\mathrm{g}} C_1, \quad \text{(F9)}$$

$$J' = -\omega^2 L_{\mathrm{g}} C_2, \quad \text{(F10)}$$

$$d = -\frac{\omega L_{\mathrm{g}}}{R}. \quad \text{(F11)}$$

These equations can also be solved using Newton's method. Note that, for both the GP equation and the circuit model, we set all lattice sites (including the interface site) to have the

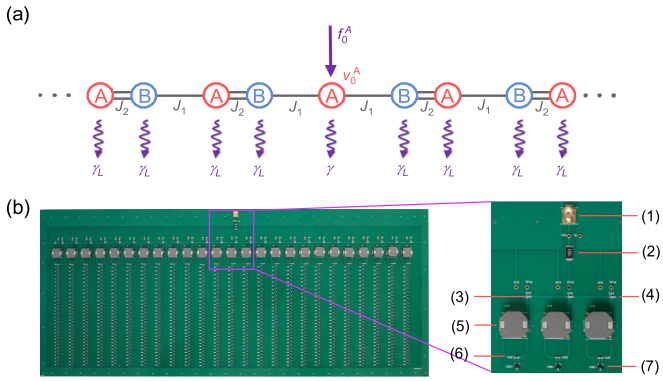

FIG. 20. Experimental implementation of the circuit sample connected by two lattices with the different topological properties in the linear limit [Fig. 1(b)]. (a) Schematic of the nonlinear SSH lattice with the nearest neighbor couplings $J_{1,2}$, the dissipations γ_L and γ, and the external driving voltage f_0^{A}. The voltage at the interface node is v_0^{A}. (b) Fabricated PCB of the nonlinear SSH circuit lattice. The inset shows the enlarged figure with the circuit components: (1) SMA connector, (2) shunt resistor R, (3) coupling capacitor C_1, (4) coupling capacitor C_2, (5) grounding inductor L_{g}, (6) grounding capacitor C_{g}, and (7) varactor diode C_{v}.

same onsite energy E_0 to ensure the chiral symmetry of the linear SSH model. Experimentally, this equal onsite energy can be achieved by adding an additional capacitance $C_2 - C_1$ to the grounding capacitance of the interface circuit node. Furthermore, in the theoretical calculations of both the GP equation and the circuit model, we set $N = 60$.

To experimentally observe the nonlinear topological interface states, we excite the interface circuit node with the external driving voltage f_0^{A}, and consider the dissipations induced both from the series resistance of the inductors and shunt resistors. As schematically shown in Fig. 20(a), the interface circuit node experiences the dissipation γ and the other nodes have the dissipation γ_L. The voltage at the interface node is v_0^{A}. Figure 20(b) shows the fabricated PCB of the nonlinear circuit lattice, and the inset shows the enlarged figure with the circuit components: (1) SMA connector, (2) shunt resistor R, (3) coupling capacitor C_1, (4) coupling capacitor C_2, (5) grounding inductor L_{g}, (6) grounding capacitor C_{g}, and (7) varactor diode C_{v}. The SMA connector is connected to an external voltage source with the voltage amplitude f_0^{A}. Here, the experimental circuit lattice has the parameter $N = 6$, which corresponds to a total of 25 lattice sites.

Experimentally, for each driving voltage f_0^{A}, we measure the voltage at the interface node v_0^{A} when the driving frequency is swept from low to high and from high to low, respectively. Figure 21 shows voltage spectra at the interface node when the circuit is excited with the driving voltage f_0^{A}. The first, second and third rows show the results from the experiment, GP equation and circuit model, respectively. The directions of the frequency sweep are denoted by the blue and orange arrows. From the first column, when the driving voltage is small with $f_0^{\mathrm{A}} = 1$ V, the voltage spectra for the frequency sweep along the two opposite directions coincide with each other. The symmetric peaks exhibited by the voltage spectra are the signature of the excitation of the linear topological interface state in the linear limit. When the driving voltage increases to $f_0^{\mathrm{A}} = 20$ V, the spectrum peaks become asymmetric with respect to the resonant frequency (see the second column). The voltage amplitude $|v_0^{\mathrm{A}}|$ shows faster variations at the higher frequencies and slower variations at the lower

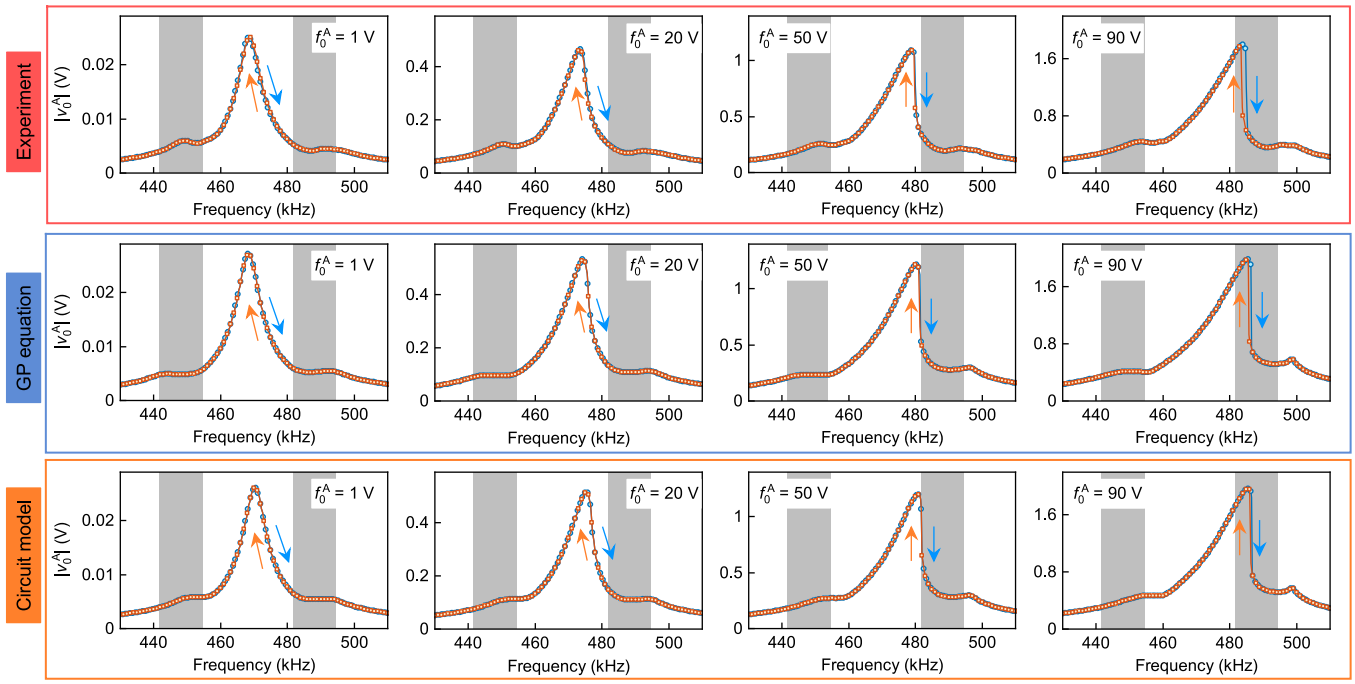

FIG. 21. Voltage spectra at the interface node when the circuit is excited with the driving voltage f_0^{A}. The first, second and third rows show the results from the experiment, GP equation and circuit model, respectively. In all the rows, the blue and orange curves correspond to the frequency sweep along the two opposite directions (denoted by the blue and orange arrows). The gray areas correspond to the linear bulk bands.

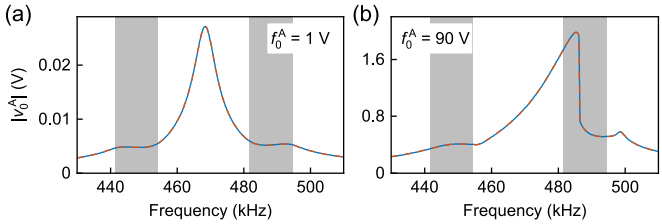

FIG. 22. Voltage spectra calculated from the driven-dissipative GP equation. Panels (a) and (b) correspond to $f_0^A = 1$ V and $f_0^A = 90$ V, respectively. In both panels, the blue and red curves represent the lattices with $N = 6$ and $N = 60$, respectively. For clarity, we present only the results obtained when sweeping the frequency from low to high.

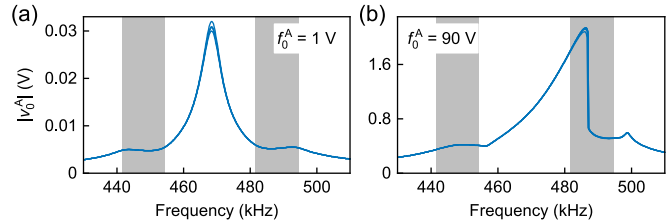

FIG. 23. Voltage spectra calculated from the driven-dissipative GP equation with ±5% variations in the series resistance of inductors. Panels (a) and (b) correspond to $f_0^A = 1$ V and $f_0^A = 90$ V, respectively. For clarity, we present only the results obtained by sweeping the frequency from low to high, and we focus on five random samples to represent this variation.

frequencies. Although the resonant frequency increases due to the enhanced circuit nonlinearity, the voltage spectra for the frequency sweep along the two opposite directions still coincide with each other. When the driving voltage further increases to $f_0^A = 50$ V, the spectrum peaks become highly asymmetric, showing the sudden interface voltage change at the same driving frequency for the frequency sweep along the two opposite directions (see the third column). Above this driving voltage, the voltage spectra exhibit the bistable response. From the last column where the driving voltage is $f_0^A = 90$ V, the voltage spectra for the frequency sweep along the two opposite directions are no longer coincide with each other. A frequency interval exists where one driving frequency corresponds to two interface voltages. The bistable response observed in the nonlinear SSH circuit lattice is a typical phenomenon in the driven-dissipative nonlinear systems. It is worthwhile to note that the voltage spectra from the experiment, GP equation, and circuit model agree well with each other, validating the correctness of the GP equation.

Before proceeding with further analysis, we note that in Fig. 21, the value of $N = 6$ corresponds to the experimental results shown in the first row, while $N = 60$ applies to the theoretical results derived from the GP equation (presented in the second row) and the circuit model (shown in the third row). Experimentally, the circuit lattice with $N = 6$ is sufficiently large for our study. To support this claim, we have also conducted theoretical calculations for a lattice with $N = 6$. Figures 22(a) and 22(b) display the voltage spectra calculated from the driven-dissipative GP equation under $f_0^A = 1$ V and $f_0^A = 90$ V, respectively. For clarity, we only present the results obtained when sweeping the frequency from low to high. The results indicate that the voltage spectra for lattices with $N = 6$ (represented by the blue curves) and $N = 60$ (represented by the red curves) are identical, demonstrating that fabricating a lattice with $N = 6$ is experimentally sufficient.

Furthermore, we conducted an error analysis by considering the variations due to the series resistance of the inductors. In the study of topological circuits, the tolerances for capacitors and inductors are typically set at ±1%. Here, we explain why we set the tolerance for the series resistance of inductors at ±2%. Since the series resistance depends on frequency, we fit the experimental relationship between series resistance and frequency using the formula $R_L = p_1 f + p_2$, where f is the working frequency, and p_1 and p_2 are parameters. Our fitting results indicate that different inductors have nearly equal values of p_1, but varying values of p_2. To determine an appropriate value for the tolerance of series resistance, we theoretically calculated the voltage spectra by introducing ±5% variations to the parameter p_2 under input voltages of $f_0^A = 1$ V and $f_0^A = 90$ V, respectively. Note that, in the theoretical calculations, the average series resistance of the inductors for this circuit sample is not set to 600 mΩ to align with the measurement results. As shown in Fig. 23, the variation in series resistance only weakly perturbs the resonant peaks. Considering that additional variations may arise during the sample fabrication process, we have designated the tolerance for the series resistance of the inductors used in the experiments as ±2%.

From the voltage spectra at different driving voltages, shown in Fig. 21, we extract the resonant frequencies and measure the voltages at all nodes of the nonlinear circuit lattice. When the voltage spectra exhibit the bistable response, the resonant frequency is taken from the spectrum where the driving frequency is swept from low to high. To quantitatively study the properties of the nonlinear topological interface states, Fig. 24 shows the interface voltages, participation ratios (PRs), and sublattice polarizations of the states at the different resonant frequencies. The orange squares and blue circles correspond to the experimental and theoretical results, respectively. The purple curves denote the result calculated from the GP equation without the driven-dissipative terms. And the gray areas correspond to the linear bulk bands. From Fig. 24(a), for a small interface voltage $|v_0^A|$, i.e., in the linear limit, the frequency of the topological interface state reside in the middle of the SSH bandgap. With the increasing of $|v_0^A|$, the nonlinearity in the SSH circuit lattice is enhanced, and the frequency of the topological interface state exhibits the blue shift. Under large nonlinearities, the experimental frequencies deviate from the theoretical data because of the increased series resistance of the inductors and the decreased driving voltage provided by the voltage source. To measure the localization of the nonlinear topological interface states, we introduce PR which is defined as

$$\mathrm{PR} = \frac{\left[\sum_m \left(\left|V_m^A\right|^2 + \left|V_m^B\right|^2\right)\right]^2}{\sum_m \left(\left|V_m^A\right|^4 + \left|V_m^B\right|^4\right)}. \tag{F12}$$

A high PR indicates that the wave function is spread over a large number of lattice sites, suggesting delocalization.

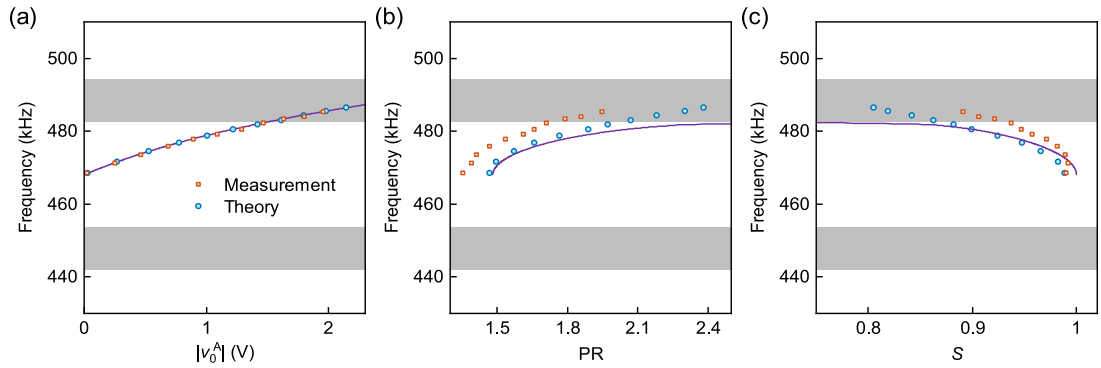

FIG. 24. Interface voltages $|v_0^A|$, participation ratios (PRs), and sublattice polarizations S of the nonlinear topological interface states. The orange squares and blue circles correspond to the experimental and theoretical results, respectively. The purple curves denote the result calculated from the GP equation without the driven-dissipative terms, and the gray areas correspond to the linear bulk bands.

Conversely, a low PR indicates that the wave function is confined to a small number of sites, indicating localization. For instance, when the state is uniformly distributed in an SSH lattice with N unit cells, we have PR $= 2N$. In contrast, PR $= 1$ occurs when the state is strongly localized at a single site. From Fig. 24(b), under the larger input voltages, the localization of the nonlinear topological interface state decreases. Note that the discrepancy between the results is also induced by the circuit dissipation. Since the experimental circuit dissipation is usually larger than the theoretical value, the nonlinear topological interface states observed in our experiment show smaller PRs, i.e., stronger localization. However, the experimental and theoretical results show the same evolutionary trend, validating the fact that the nonlinearity weakens the localization of the nonlinear topological interface states. The topological interface states are chiral which are described by the sublattice pseudospin S. $S = 1$ implies the perfect sublattice localization on the site A and $S = -1$ implies the perfect sublattice localization on the site B. Figure 24(c) shows the dependence between the frequency and sublattice pseudospin of the nonlinear topological interface states. From the figure, in the linear limit, we have $S \approx 1$ for both the experimental and theoretical results. These results agree with the prediction from the GP equation without the driven-dissipative terms. For the larger driving voltages, i.e., for the larger frequencies, the nonlinear topological interface states exhibit a decreased sublattice pseudospin. Again, the experimental result deviates from the theoretical data because of the increased circuit dissipation and decreased driving voltage. The small discrepancy near the linear limit is due to the inaccuracy of the measurement data recorded by the oscilloscope.

To reveal the feature of the bistable response of the nonlinear topological interface states, we experimentally fix the driving frequency to 484 kHz, and measure the voltage at the interface node v_0^A when the driving voltage f_0^A is swept from small to large and from large to small, respectively. Figure 25(a) shows the bistable response between the voltage at the interface node and the external driving voltage. The blue and orange curves correspond to the experimental voltage sweep along the two opposite directions (denoted by the blue and orange arrows). From the the figure, the response curves of the interface voltages for the driving voltage sweeps along the two opposite directions are not coincide with each other. The hysteresis loop shows that there is an interval for the driving voltage where one driving voltage corresponds to two interface voltages. In Fig. 25(b), we show the voltage distributions at the two states of the bistable response where the driving voltage is $f_0^A = 84$ V [indicated by the dashed line in Fig. 25(a)]. Although the two voltage distributions correspond to the same driving voltage, the state at the upper branch shows the larger sublattice pseudospin S and stronger localization (i.e., smaller PR), compared to the state at the lower branch.

APPENDIX G: THEORETICAL RESULTS OF THE TOPOLOGICAL GAP SOLITONS

In this Appendix, we give more theoretical results of the topological gap solitons. For completeness, we also introduce the topologically trivial gap solitons. Since both the topologically nontrivial and trivial gap solitons reside in the bulk of the lattice, to distinguish with the nonlinear edge states, we simply call them bulk solitons for clarity. This section is organized as follows. In the first subsection, we introduce the the bulk solitons in a single dimer with the onsite nonlinearity. Then

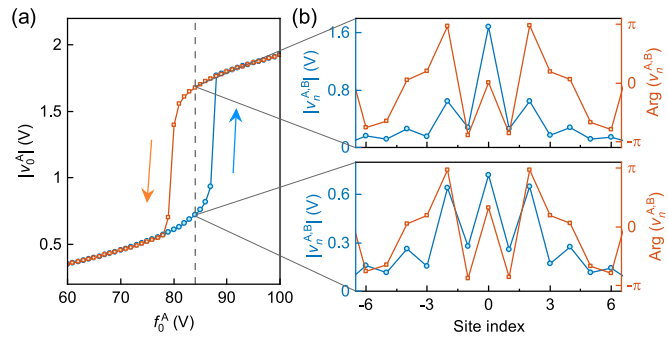

FIG. 25. Experimental bistable response of the nonlinear topological interface states. (a) The bistable response between the voltage at the interface node and the external driving voltage, where the driving frequency is 484 kHz. The blue and orange curves correspond to the experimental voltage sweeps along the two opposite directions (denoted by the blue and orange arrows). (b) The voltage distributions at the two bistable states with the driving voltage indicated by the dashed line in panel (a).

the existence of the bulk solitons in an SSH lattice is studied in the second subsection. In the third subsection, we show the results for the stability analysis of the bulk solitons. Finally, we discuss the physical interpretation of the topological gap solitons in the last subsection.

1. Solitons in a single dimer

In the AC limit, the SSH lattice reduces to a single dimer. Here we only study the dimer with a strong bond because the bulk solitons that we study in this paper are the continuations of the solitons in a circuit dimer with the coupling capacitor $C_2 = 560$ pF. In the case with $C_1 = 0$, the GP equation for the nonlinear modes reduces to

$$E_0\psi_0^{\mathrm{A}} + g\left(\psi_0^{\mathrm{A}}\right)\psi_0^{\mathrm{A}} + J_2\psi_0^{\mathrm{B}} = \bar{\omega}\psi_0^{\mathrm{A}}, \tag{G1}$$

$$E_0\psi_0^{\mathrm{B}} + g\left(\psi_0^{\mathrm{B}}\right)\psi_0^{\mathrm{B}} + J_2\psi_0^{\mathrm{A}} = \bar{\omega}\psi_0^{\mathrm{B}}. \tag{G2}$$

Depending on the parameters, the equations may have the three types of solutions: symmetric, antisymmetric and asymmetric solutions. When the solution is symmetric, i.e., $\psi_1^{\mathrm{A}} = \psi_0^{\mathrm{B}}$, the equations further reduce to

$$E_0 + g\left(\psi_0^{\mathrm{A}}\right) + J_2 = \bar{\omega}, \tag{G3}$$

which implies that the symmetric soliton reside in the upper semi-infinite bandgap. When the solution is antisymmetric, i.e., $\psi_1^{\mathrm{A}} = -\psi_1^{\mathrm{B}}$, the equations reduce to

$$E_0 + g\left(\psi_0^{\mathrm{A}}\right) - J_2 = \bar{\omega}, \tag{G4}$$

which implies that the antisymmetric soliton reside in the middle SSH gap. Specifically, asymmetric solitons may appear due to the linear instability induced by the spontaneous symmetry breaking of the symmetric solitons. To reveal all these features, we use the nonsaturable nonlinearity instead and the results for the solitons in a single dimer with the nonsaturable nonlinearity is shown in Fig. 26.

Figure 26(a) shows the bifurcations of the symmetric, antisymmetric, and asymmetric solitons. In the linear limit, only the symmetric and antisymmetric solitons exist. However, the asymmetric solitons appear by bifurcating from the symmetric solitons. Such bifurcation is induced by the linear instability of the symmetric solitons. From the maximum growth rates shown in Fig. 26(b), the antisymmetric and asymmetric solitons are always linearly stable. The symmetric solitons are linearly stable near the linear limit and become linearly unstable for large nonlinearities. The transition frequency that separates the stable and unstable regions corresponds to the bifurcation frequency of the asymmetric solitons in Fig. 26(a). To prove the stability or instability of the symmetric solitons, we select the two solitons marked in Figs. 26(a) and 26(b) and carry out the temporal evolutions with $\pm 1\%$ noises added to the inputs. To quantitatively measure the stability/instability, we introduce the asymmetry parameter defined as

$$\Theta = \left|\frac{|\psi_1| - |\psi_2|}{|\psi_1| + |\psi_2|}\right|. \tag{G5}$$

For the stable solitons, Θ should equal to zero approximately along the temporal evolution. For the unstable solitons, the symmetry between ψ_1 and ψ_2 is broken, leading to the nonzero asymmetry parameters. Figure 26(c) shows the

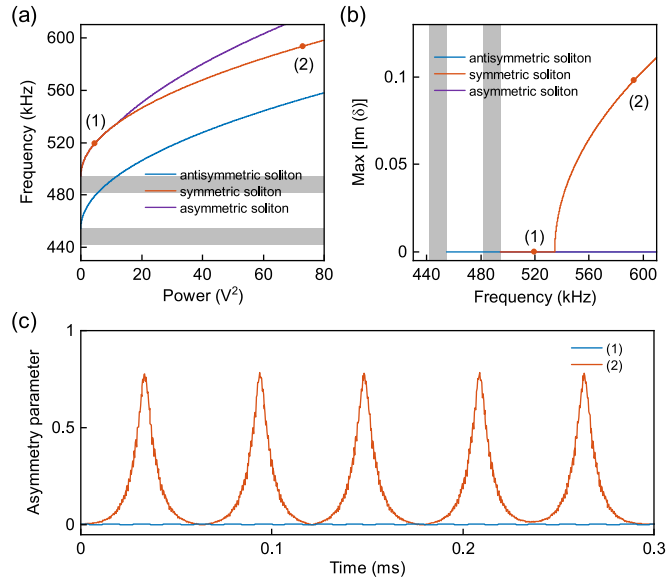

FIG. 26. Solitons in a single dimer with the nonsaturable nonlinearity. (a) The symmetric, antisymmetric, and asymmetric solitons in a single dimer with the nonsaturable nonlinearity. (b) The maximum growth rates of the perturbed solutions of the solitons. The gray areas in panels (a), (b) denote the linear bulk bands. (c) The asymmetry parameters of the stable and unstable symmetric solitons along the temporal evolutions. Noises with $\pm 1\%$ random perturbations are added to the initial input. The frequencies of the stable and unstable solitons are marked in panels (a), (b).

asymmetry parameters of the stable and unstable symmetric solitons. Although noises are added to the input, the stable soliton always has $\Theta \approx 0$ (blue curve). In contrast, the unstable soliton shows the oscillating values of Θ, implying that the voltage oscillates between the two circuit sites (orange curve).

Considering the actual circuit nonlinearity (saturable nonlinearity), the asymmetric solitons do not exist and we only find the symmetric and antisymmetric solitons. The symmetric solitions in a single dimer correspond to the topologically trivial bulk solitons in an SSH lattice, and the antisymmetric solitons in a dimer correspond to the topologically nontrivial bulk solitons, i.e., the topological gap solitons.

2. Existence of the bulk solitons

We again consider an SSH lattice with the intracell hopping J_2 and intercell hopping J_1. In the study of the nonlinear topological edge states, the SSH lattice has an open boundary at the left edge. Here we are interested in the bulk solitons that reside in the bulk of the lattice. The chain also has 120 unit cells, i.e., $N = 120$.

Based on the symmetric and antisymmetric solitons in a single dimer, we get the bulk solitons in an SSH lattice using the AC approach. To distinguish the bulk solitons to the nonlinear bulk states, we also calculate the solutions for the nonlinear bulk states based on the GP equation. We focus on the two linear bulk states that reside at the upper edges of the bulk bands. For a lattice with N unit cells, the linear bulk states that reside at the upper edges of the bulk bands corresponds to the Nth and $2N$th states. We take these linear

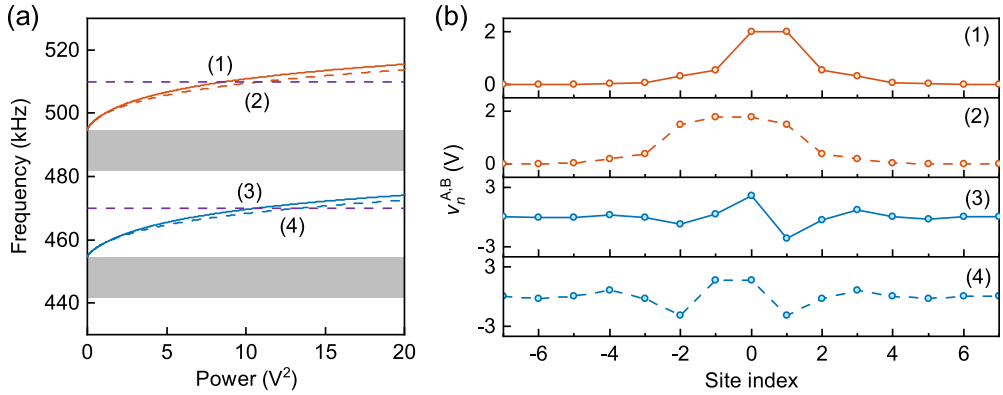

FIG. 27. Bulk solitons and nonlinear bulk states. (a) Frequencies of the bulk solitons (solid curves) and nonlinear bulk states (dashed curves). (b) Voltage distributions of the nonlinear states labeled in panel (a).

bulk states as the initial guess solutions of the GP equation and obtain the nonlinear bulk states when considering the circuit nonlinearity. The results for the bulk solitons and nonlinear bulk states are shown in Fig. 27.

Figure 27(a) shows the frequencies of the bulk solitons (solid curves) and nonlinear bulk states (dashed curves), and Fig. 27(b) shows the voltage distributions of the typical states labeled in Fig. 27(a). The equivalent circuit power P is again used as a measure of the nonlinearity strength. The bulk solitons exhibit two branches, which reside in the middle SSH gap and upper semi-infinite gap, respectively. In Fig. 27(a), the orange and blue curves correspond to the topologically trivial and nontrivial bulk solitons, respectively. The topologically nontrivial and trivial bulk solitons are continuations of the antisymmetric and symmetric solitons in a single dimer, respectively. From the first and third rows in Fig. 27(b), the bulk solitons mainly reside in the middle unit cell which contains the lattice sites 0 and 1. Specifically, for the topologically nontrivial bulk soliton in the first row, when we split the lattice into two parts from the middle of the middle unit cell, the corresponding two parts of the topologically nontrivial bulk soliton have very similar profiles to the nonlinear topological edge states. The emergence of this type of bulk solitons can be understood that the circuit nonlinearity induces an interface at the middle of the middle unit cell and the two newly formed lattices at the two sides are both topologically nontrivial with the intracell hopping J_1 smaller than the intercell hopping J_2. For the left part of the topologically nontrivial bulk soliton, it is mainly confined to the sublattice site A and exhibits a phase jump of π among the neighboring cells. The right part of the topologically nontrivial bulk soliton also exhibits a phase jump but it is mainly confined to the sublattice site B. Such behavior indicates the different chiralities of the two parts of the topologically nontrivial bulk solitons: the left and right parts have the sublattice pseudospins with the different signs. Thus, this type of bulk solitons are the nonlinearity induced topologically nontrivial bulk solitons. While for the the topologically trivial bulk soliton in the third row, the voltages at the two sites of the middle unit cell are in-phase, in contrast to the out-of-phase voltage distribution of the topologically nontrivial bulk soliton. Since the topologically trivial bulk solitons are the nonlinearity induced localization modes, there is no phase jump among the neighboring cells. Note that here only the symmetric topologically trivial bulk solitons are found because of the saturable nonlinearity of the varactor diodes. It is worthwhile to note that, although the bulk solitons bifurcate from the edge of linear Bloch band and converge to the bulk state in the linear limit, the profiles of the bulk solitons are different to those of the nonlinear bulk states. The bulk states are extended in the linear limit, but under the circuit nonlinearity, they become localized with the voltages distributing mainly at the lattice sites -1 and 0, as shown by the second and fourth rows of Fig. 27(b).

3. Stability analysis of the bulk solitons

We then study the stability analysis of both the topologically nontrivial and trivial bulk solitons, i.e., the gap solitons. Figure 28(a) shows the maximum growth rates of the topologically nontrivial gap solitons at the different frequencies. From the figure, the maximum growth rates are in the order of 10^{-3} when the soliton frequencies are near to the lower edge of the top bulk band. This region corresponds to the linearly unstable solitons. However, since we are interested in the localized topologically nontrivial gap solitons and the maximum frequency shifts of the gap solitons are limited by the experimental input voltage, we carry out the temporal evolution of the topological gap soliton at the frequency of 470 kHz. Noises with $\pm 2\%$ random perturbations are added to the input amplitude. To quantitatively measure the mode stability/instability, we also use the asymmetry parameter Θ to characterize the voltage asymmetry between the sites 0 and 1. From the voltage distribution in Fig. 28(b), there are no apparent variations along the temporal evolution. The asymmetry parameters are in the order of 10^{-3}. These results imply that, although the unstable region exists, at least within the experimentally realizable parameter range, the topologically nontrivial gap solitons should be observable because of their weak instabilities.

The results for the stability analysis of the topologically trivial gap solitons are shown in Figs. 28(c) and 28(d). Compared to the topologically nontrivial gap solitons, the topologically trivial gap solitons have much smaller Max[Im(δ)] (in the order of 10^{-9}), implying that they are much more stable. We take the topologically trivial gap soliton at 510 kHz as an example and study its temporal evolution,

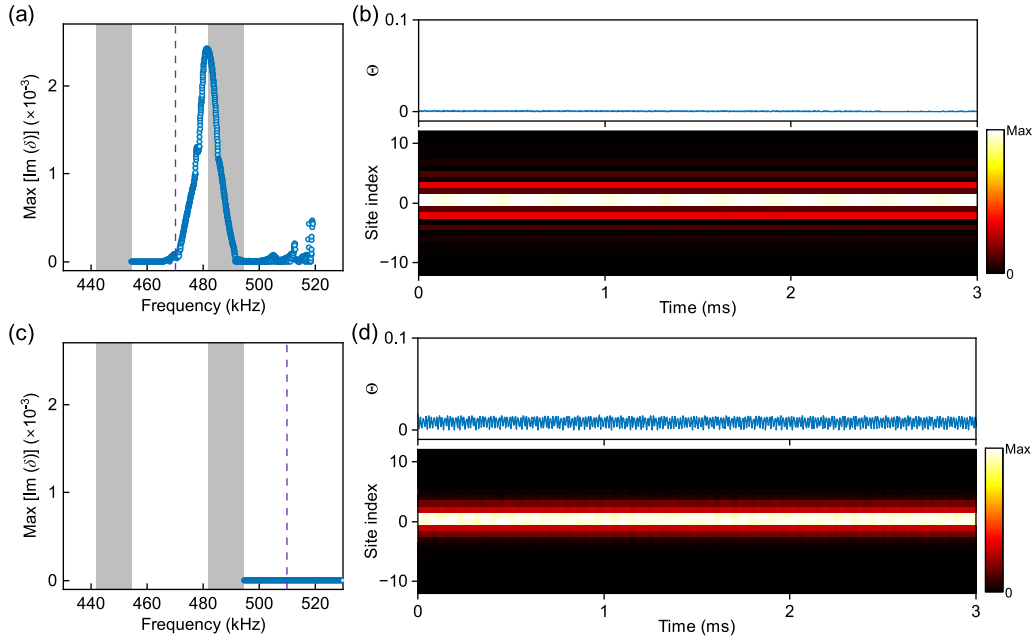

FIG. 28. Stability analysis of the bulk solitons. (a) The maximum growth rates of the perturbed solutions of the topologically nontrivial gap solitons. (b) The temporal evolution of the topologically nontrivial gap soliton at the frequency indicated in panel (a). Noises with ±2% random perturbations are added to the initial input. (c), (d) Results for the topologically trivial gap solitons. In panels (a), (c), the gray areas denote the linear bulk bands.

again with ±2% noises added to the input. From Fig. 28(d), both the voltage distribution and asymmetry parameters confirm that the topologically trivial gap soliton is stable.

4. Physical interpretation of the topological gap solitons

The interface, edge, and bulk solitons are related to the solutions of the linear equations due to the self-consistent effective edges. For the interface solitons, we consider a linear SSH model with an additional impurity potential barrier defined as

$$g_{\mathrm{im}} = \frac{\eta C_{\mathrm{im}}}{2(C_{\mathrm{g}} + \eta C_{\mathrm{L}})} \frac{\omega_0}{\omega_n}, \tag{G6}$$

where C_{im} is the effective capacitance of the impurity potential. The impurity potential is placed only on the interface site, i.e., the site A in the 0th cell (hence playing the role of an effective interface at the interface site). Considering the governing equations, the circuit nonlinearity creates a potential barrier at the interface, while the equations for the other sites are the same to those in the linear limit. For the edge solitons, we again consider a linear SSH model with an additional impurity potential barrier defined in Eq. (G6). However, for the edge solitons in a topologically nontrivial lattice, the impurity potential is placed only on the edge site, i.e., the site A in the 1st cell (hence playing the role of an effective edge at the edge site); for the edge solitons in a topologically trivial lattice, the impurity potential is placed on the two edge sites, i.e., the sites A and B in the 1st cell. Then the governing equations for both the topologically nontrivial and trivial lattices can be obtained and solved similarly. For the bulk solitons, the impurity potential is placed on the two middle sites, i.e., the sites A and B in the 0th cell. As an example, here we only compare the topologically nontrivial bulk soliton solution with the state in a linear model plus an impurity in the bulk, and the results are shown in Fig. 29(a). From the figure, the solution of the linear model (orange curve) is consistent to the solution of the topologically nontrivial gap soliton (blue curve), implying that the onsite nonlinearity creates an impurity potential.

The above property can also be understood from the solution of the GP equation. Since the bulk solitons mainly reside at the middle unit cell, we only consider the circuit nonlinearities at the middle two sites and neglect the nonlinearities at the other sites. With $V_m^{\mathrm{A,B}}(T) = v_m^{\mathrm{A,B}} e^{-i\bar{\omega}T}$, the governing equations reduce to

$$\ldots, \tag{G7}$$

$$\bar{\omega} v_{-1}^{\mathrm{B}} = E_0 v_{-1}^{\mathrm{B}} + J_2 v_{-1}^{\mathrm{A}} + J_1 v_0^{\mathrm{A}}, \tag{G8}$$

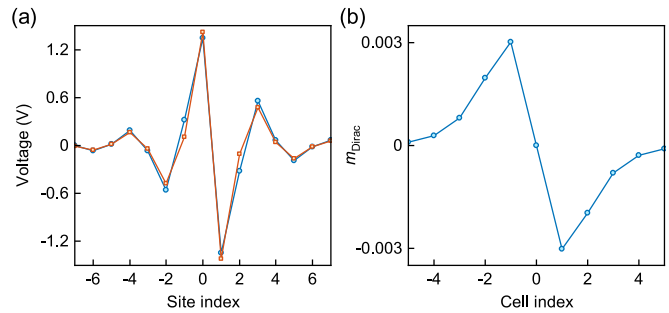

FIG. 29. Physical interpretation of the topologically nontrivial gap solitons. (a) The solution of the topologically nontrivial bulk soliton (blue curve) compared with the state in a linear model plus an impurity potential in the bulk (orange curve). (b) Mass term m_{Dirac} of the 1D Dirac equations.

$$\bar{\omega}v_0^{\mathrm{A}} = E_0 v_0^{\mathrm{A}} + g\left(v_0^{\mathrm{A}}\right)v_0^{\mathrm{A}} + J_2 v_0^{\mathrm{B}} + J_1 v_{-1}^{\mathrm{B}}, \tag{G9}$$

$$\bar{\omega}v_0^{\mathrm{B}} = E_0 v_0^{\mathrm{B}} + g\left(v_0^{\mathrm{B}}\right)v_0^{\mathrm{B}} + J_2 v_0^{\mathrm{A}} + J_1 v_1^{\mathrm{A}}, \tag{G10}$$

$$\bar{\omega}v_1^{\mathrm{A}} = E_0 v_1^{\mathrm{A}} + J_2 v_1^{\mathrm{B}} + J_1 v_0^{\mathrm{B}}, \tag{G11}$$

$$\ldots. \tag{G12}$$

Since the linear topological edge state has $\bar{\omega} = E_0$, the voltage distribution satisfies $v_m^{\mathrm{A}} = (-\frac{J_1}{J_2})^{|m|} v_0^{\mathrm{A}}$ and $v_m^{\mathrm{B}} = 0$ for the left part with $m \leqslant -1$; and $v_m^{\mathrm{B}} = (-\frac{J_1}{J_2})^{|m|} v_0^{\mathrm{B}}$ and $v_m^{\mathrm{A}} = 0$ for the right part with $m \leqslant 1$. The voltages at the middle two sites with $m = 0$ satisfy

$$g\left(v_0^{\mathrm{A}}\right)v_0^{\mathrm{A}} + J_2 v_0^{\mathrm{B}} = 0, \tag{G13}$$

$$g\left(v_0^{\mathrm{B}}\right)v_0^{\mathrm{B}} + J_2 v_0^{\mathrm{A}} = 0. \tag{G14}$$

The topologically nontrivial gap solitons have $v_0^{\mathrm{A}} = -v_0^{\mathrm{B}}$ and the equations reduce to

$$g\left(v_0^{\mathrm{A,B}}\right) = J_2. \tag{G15}$$

Thus, if Eq. (G15) has solutions, then the topologically nontrivial gap solitons can be explained by the solution of the GP equation.

The topologically nontrivial bulk solitons, i.e., the topologically nontrivial gap solitons can also be interpreted as the Jackiw-Rebbi-type Dirac boundary mode. From Eqs. (B26) and (B27), the governing equations can be rewritten as

$$i\frac{dV_m^{\mathrm{A}}}{dT} = \left[E_0 + \frac{g\left(V_m^{\mathrm{A}}\right) + g\left(V_m^{\mathrm{B}}\right)}{2}\right]V_m^{\mathrm{A}} + \frac{g\left(V_m^{\mathrm{A}}\right) - g\left(V_n^{\mathrm{B}}\right)}{2}V_m^{\mathrm{A}} + J_2 V_m^{\mathrm{B}} + J_1 V_{n-1}^{\mathrm{B}}, \tag{G16}$$

$$i\frac{dV_m^{\mathrm{B}}}{dT} = \left[E_0 + \frac{g\left(V_m^{\mathrm{A}}\right) + g\left(V_m^{\mathrm{B}}\right)}{2}\right]V_m^{\mathrm{B}} - \frac{g\left(V_m^{\mathrm{A}}\right) - g\left(V_m^{\mathrm{B}}\right)}{2}V_m^{\mathrm{B}} + J_2 V_m^{\mathrm{A}} + J_1 V_{m+1}^{\mathrm{A}}. \tag{G17}$$

These equations can be transformed to the 1D Dirac equations in the continuum limit [91], where the mass term is defined as

$$m_{\mathrm{Dirac}} = \frac{g\left(V_m^{\mathrm{A}}\right) - g\left(V_m^{\mathrm{B}}\right)}{2}. \tag{G18}$$

From Fig. 29(b), the mass term exhibits an inversion. Thus, the Dirac mass inversion leads to the formation of the Jackiw-Rebbi-type Dirac boundary modes, i.e., the topologically nontrivial bulk solitons.

APPENDIX H: EXPERIMENTAL MEASUREMENT OF THE TOPOLOGICAL GAP SOLITONS

In this Appendix, we give more experimental results of the gap solitons, including both the topologically nontrivial and trivial ones.

Besides the nonlinear topological edge states, in this Appendix we observe the bulk solitons which reside in the bulk of the circuit lattice. According to the theoretical results, both the topologically nontrivial and trivial bulk solitons are mainly localized at the middle unit cell. For the topologically nontrivial bulk solitons, the voltages at the two sites of the middle unit cell are out-of-phase. While for the topologically trivial bulk solitons, the voltages at the sublattice sites A and B are in-phase. Due to the distinct properties of the topologically nontrivial and trivial bulk solitons, experimentally we need to excite the two types of the bulk solitons using the different driving voltages. As shown in Fig. 30(a), the nonlinear SSH lattice has the intracell hopping J_2 and intercell hopping J_1. The two sublattice sites of the middle unit cell are driven by the external voltages f_0^{A} and f_0^{B}, respectively. The lattice also experiences the dissipations induced both from the series resistance of inductors and shunt resistors. Since this lattice is a topologically trivial lattice in the linear limit, the absence of the edge solitons avoids the coupling between the bulk and edge solitons. Figure 30(b) shows the fabricated PCB of the driven-dissipative nonlinear circuit lattice, and the inset shows the enlarged figure with the circuit components: (1), (2) SMA connectors, (3) shunt resistor R, (4) coupling capacitor C_2, (5) coupling capacitor C_1, (6) grounding inductor L_{g}, (7) grounding capacitor C_{g}, and (8) varactor diode C_{v}. Here, the two SMA connectors are connected to the external voltage sources with the voltage amplitude f_0^{A} and f_0^{B}, respectively. The experimental circuit lattice has the parameter $N = 12$, which corresponds to a total of 24 lattice sites. Note that the phase difference between the driving voltages can be tuned arbitrarily. Such flexibility of electrical circuits provides convenience to the observation of the nonlinear topological states. In the theoretical calculations, we also set $N = 120$, indicating that the lattice contains 120 unit cells.

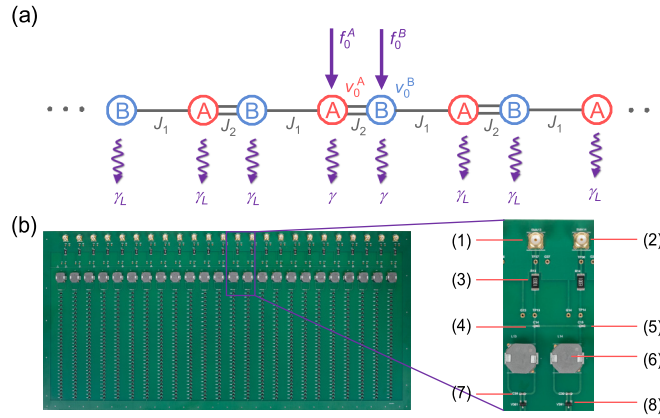

FIG. 30. Experimental implementation of the SSH lattice with onsite nonlinearity that supports the topological gap solitons. (a) Schematic of the nonlinear SSH lattice with the two external driving voltages f_0^{A} and f_0^{B}. (b) Fabricated PCB of the driven-dissipative nonlinear circuit lattice with the enlarged figure showing the circuit components: (1, 2) SMA connectors, (3) shunt resistor R, (4) coupling capacitor C_2, (5) coupling capacitor C_1, (6) grounding inductor L_{g}, (7) grounding capacitor C_{g}, and (8) varactor diode C_{v}. The two SMA connectors are connected to the external voltage sources with the voltage amplitude f_0^{A} and f_0^{B}, respectively.

First, we impose the out-of-phase driving voltages and observe the topologically nontrivial bulk solitons. Figure 31(a) shows the voltage spectra at the sublattice site A in the middle unit cell. The first and second rows show the experimental

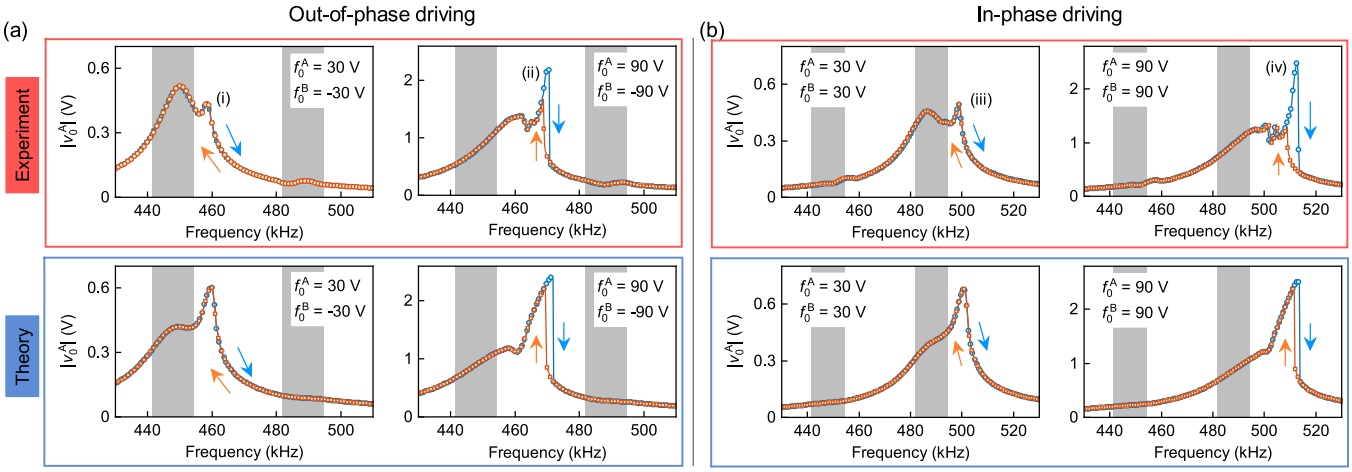

FIG. 31. Voltage spectra at the bulk node when the circuit is excited with the out-of-phase or in-phase driving voltages $f_0^{A,B}$. (a) Voltage spectra at the sublattice site A in the middle unit cell when the circuit is excited with the out-of-phase driving voltages. (b) Voltage spectra under the in-phase driving. In panels (a), (b), the gray areas correspond to the linear bulk bands.

and theoretical results, respectively. The directions of the frequency sweep are denoted by the blue and orange arrows. The first column in Fig. 31(a) shows the voltage spectra when the driving voltages are $f_0^A = 30$ V and $f_0^B = -30$ V. We observe that one peak reside in the middle SSH gap and the voltage spectra for the frequency sweep along the two opposite directions coincide with each other. When the driving voltages are increased to $f_0^A = 90$ V and $f_0^B = -90$ V, the spectrum peaks become highly asymmetric and exhibit the bistable response, as shown in the second column of Fig. 31(a).

To prove that the peaks which reside in the SSH gap are the signatures of the excitation of the topologically nontrivial bulk solitons, we measure the voltage distributions in the nonlinear circuit lattice under the different driving voltages. From Fig. 32(a), the voltage distributions are mainly confined to the middle unit cell which contains the lattice sites 0 and 1. When we split the lattice into the two parts from the middle of the middle unit cell, i.e., the lattice site 0.5, the left part of the voltage distribution is mainly confined to the sublattice site A and exhibits a phase jump of π among the neighboring cells. The right part of the voltage distribution also exhibits a phase jump but it is mainly confined to the sublattice site B. Such phenomenon agrees with the behavior of the topologically nontrivial bulk solitons.

Second, we impose the in-phase driving voltages and observe the topologically trivial bulk solitons. In Fig. 31(b), we observe the phenomenon similar to that shown in Fig. 31(a). When the driving voltages are $f_0^A = 30$ V and $f_0^B = 30$ V, we also observe a peak from the voltage spectra, but this peak reside in the upper semi-infinite gap. When the driving voltages increase to $f_0^A = 90$ V and $f_0^B = 90$ V, the peak in the upper semi-infinite gap exhibits the bistable response, as shown in the second column. From the normalized amplitudes and phases of the voltage distributions shown in Fig. 32(b), the topologically trivial bulk solitons are also mainly localized at the lattice site 0 and 1, but the voltages at the different sites have nearly equal phases, in strong contrast to the phase jump observed for the topologically nontrivial bulk solitons. Since the topologically trivial bulk solitons are the nonlinearity induced localized modes, the topological trivial bulk solitons become more localized with the increasing circuit nonlinearity.

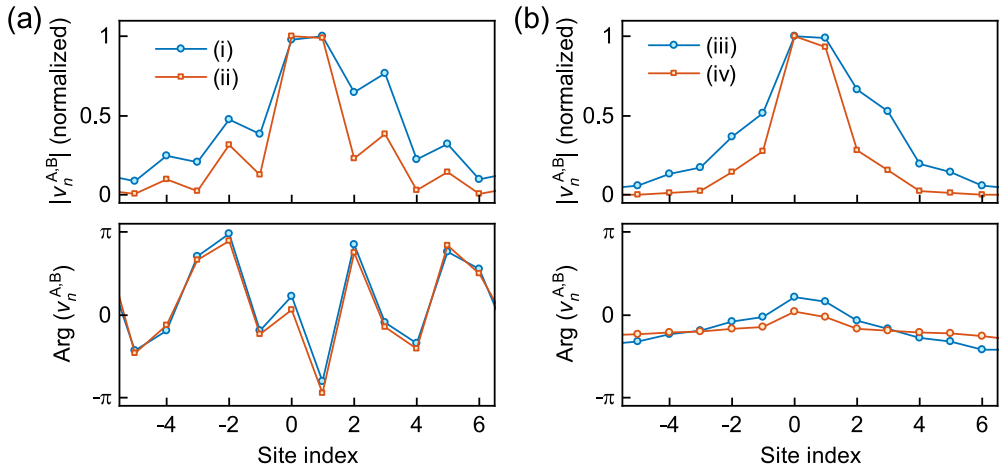

FIG. 32. Experimental voltage distributions at the resonant frequencies labeled in Fig. 31. Panels (a), (b) correspond to the results under the out-of-phase driving and in-phase driving, respectively. The voltage amplitudes are normalized.

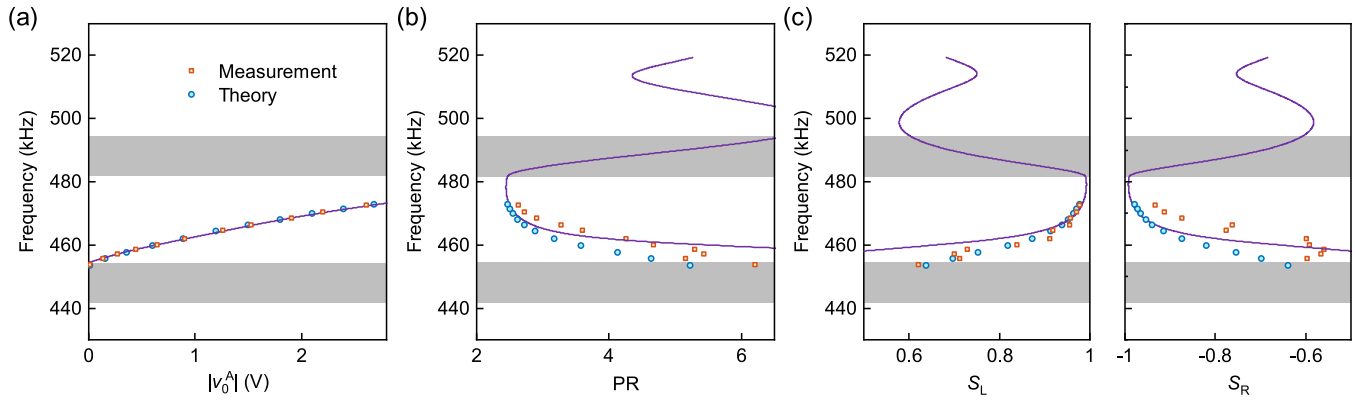

FIG. 33. Bulk voltages $|v_0^A|$, participation ratios (PRs), and local sublattice polarizations $S_{L,R}$ of the topological gap solitons. The orange squares and blue circles correspond to the experimental and theoretical results, respectively. The purple curves denote the result calculated from the GP equation without the driven-dissipative terms, and the gray areas correspond to the linear bulk bands.

We note that, for both the topologically nontrivial and trivial bulk solitons, the experimental measurement results exhibit some deviations from the theoretical predictions. As shown in Fig. 31, these deviations become more pronounced at higher input voltages, primarily due to increased series resistance of the inductors and decreased driving voltages provided by the voltage source under large nonlinearities. Additionally, as illustrated in Fig. 32, the experimental voltage amplitudes deviate from perfectly symmetric profiles, which may arise from three main factors: imperfections in the circuit lattice caused by component errors that result in a lack of symmetry about the center of the unit cell, unequal amplitudes of the two driving voltages, and limitations in the temporal resolution of the oscilloscope, which may contribute to errors in the resonant frequencies we obtained.

To quantitatively compare the experimental and theoretical results of the topologically nontrivial gap solitons, we extract the resonant frequencies from the voltage spectra by following the same procedure. Figure 33(a) shows the dependence between the frequency and voltage v_0^A. The result from the GP equation without the driven-dissipative terms is also plotted for comparison. The experimental result (orange squares) agrees well with the theoretical result (blue circles) and the result from the GP equation without the driven-dissipative terms. This observation validates the fact that the topologically nontrivial gap solitons bifurcate from the edge of the linear Bloch band and converge to the bulk state in the linear limit. Meanwhile, since the topologically nontrivial bulk solitons are nonlinearity induced, with the increasing of the frequency, i.e., with the enhancement of the nonlinearity, the voltage distribution becomes more localized with the smaller PRs, as shown in Fig. 33(b). To quantitatively measure the sublattice pseudospin of the topologically nontrivial bulk solitons, we split the circuit lattice into the two parts from the middle of the middle unit cell, and the local sublattice pseudospins are calculated for the left and right parts, respectively. The result is shown in Fig. 33(c). From the first column, the left parts of the topologically nontrivial bulk solitons are mainly confined to the sublattice site A. While the right parts are mainly confined to the sublattice site B, as shown in the second column. Meanwhile, with the increasing of the frequency, the absolute values of both S_L and S_R approach 1. This implies that, a stronger nonlinearity results in a greater voltage localization on the sublattice site A for the left part and B for the right part. Such property validates that the topologically nontrivial bulk solitons are the nonlinearity induced topological states.

APPENDIX I: THEORETICAL RESULTS OF THE SELF-INDUCED TOPOLOGICAL EDGE STATES

In this Appendix, we give more theoretical results of the self-induced topological edge states. For completeness, we also introduce the topologically trivial edge solitons. The topologically trivial chain consists of 120 unit cells, i.e., $N = 120$. In the linear limit, there are no localized states present at either end of the chain. Conventionally, the topologically trivial edge solitons are called as the surface solitons [54,55]. Here, since both the self-induced topological edge states and topologically trivial edge solitons reside at the edge of the topologically trivial lattice, we simply call them edge solitons for clarity. This section is organized as follows. In the first subsection, we introduce the existence of the edge solitons. Then in the second subsection, we show the results for the stability analysis of the edge solitons. Finally, we discuss the physical interpretation of the self-induced topological edge states in the last subsection.

1. Existence of the edge solitons

We study the edge solitons that reside at the edge of a topologically trivial lattice, where the varactor diodes in the circuit are modeled as the nonsaturable and saturable nonlinearities, respectively. We solve the GP equation without the driven-dissipative terms using Newton's method. In contrast to the nonlinear topological edge states in a topologically nontrivial lattice where the topological edge state in the linear limit can be taken as the initial guess solution, no edge states exist in the linear limit for a topologically trivial lattice and thus soliton solutions have to be found using the AC approach. For simplicity, we only study the two cases with $C_1 = 0$ and $C_2 = 0$, respectively. For the case with $C_2 = 0$, the first site is decoupled from the lattice and the remaining structure becomes the discrete dimers with the intracell coupling governed

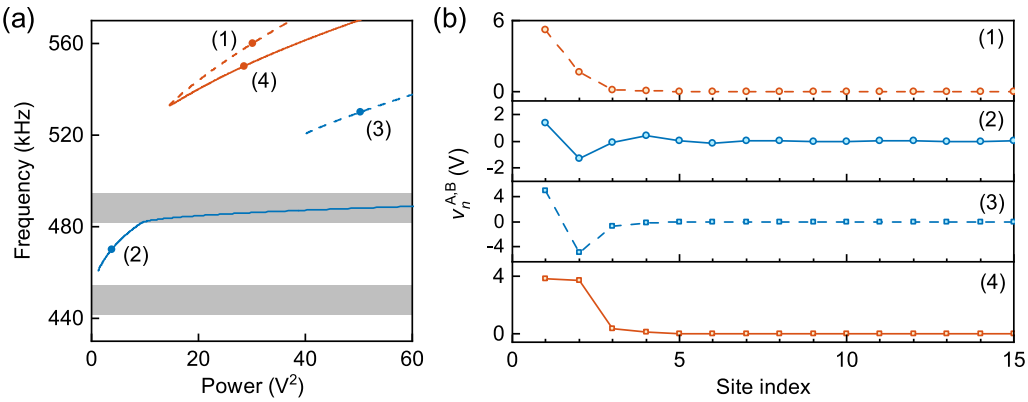

FIG. 34. Edge solitons in a topologically trivial lattice with the nonsaturable nonlinearity. (a) Frequencies of the edge solitons. The solid blue curve denotes the self-induced topological states, and the solid orange, dashed blue, and dashed orange curves correspond to the symmetric, antisymmetric, and asymmetric topologically trivial edge solitons, respectively. (b) Voltage distributions of the edge solitons labeled in panel (a).

by C_1. We are only interested in the solution where the first site has a nonzero value. Starting from the GP equation without the driven-dissipative terms, in the case with $C_2 = 0$ we get the following equation:

$$E_0 + g\left(\psi_1^{\mathrm{A}}\right) = \bar{\omega}. \tag{I1}$$

By solving this equation, we can get the value of ψ_1^{A}. Then the solutions for the edge solitons can be obtained by gradually increasing C_2 to the original value. The case with $C_1 = 0$ is equivalent to the fully dimerized limit and the lattice reduces to the discrete dimers with the intracell coupling governed by C_2. Similarly, we are only interested in the solutions where the first dimer has the nonzero values. The GP equation reduces to

$$E_0\psi_1^{\mathrm{A}} + g\left(\psi_1^{\mathrm{A}}\right)\psi_1^{\mathrm{A}} + J_2\psi_1^{\mathrm{B}} = \bar{\omega}\psi_1^{\mathrm{A}}, \tag{I2}$$

$$E_0\psi_1^{\mathrm{B}} + g\left(\psi_1^{\mathrm{B}}\right)\psi_1^{\mathrm{B}} + J_2\psi_1^{\mathrm{A}} = \bar{\omega}\psi_1^{\mathrm{B}}. \tag{I3}$$

By solving this equation, multiple solutions may exist.

We seek for the soliton solutions in a topologically trivial SSH lattice. When the varactor diodes are modeled as the nonsaturable nonlinearity, we show the frequencies of the edge solitons in Fig. 34(a). In the AC limit, one solution exists in the case with $C_2 = 0$. This solution corresponds to the topologically trivial soliton which reside in the upper semi-infinite gap, as shown by the dashed orange curve in Fig. 34(a). A typical profile of this type of topologically trivial solitons is shown in the first row of Fig. 34(b). Its profile is asymmetric and its voltage mainly distributes on the first leftmost site. In the case with $C_1 = 0$, we find that there are five solutions: two antisymmetric solutions, one symmetric solution, and two asymmetric solutions. One of the two antisymmetric solutions corresponds to the topologically nontrivial soliton which reside in the SSH gap, as shown by the sold blue curve in Fig. 34(a). This type of topologically nontrivial edge solitons is the same to the topological edge solitons discussed in the main text and a typical profile is shown in the second row of Fig. 34(b). Another antisymmetric solution corresponds to the topologically trivial edge soliton which reside in the upper semi-infinite gap, as shown by the dashed blue curve in Fig. 34(a). It has an antisymmetric voltage distribution as shown in the third row of Fig. 34(b). The symmetric solution corresponds to the topologically trivial edge soliton that we discussed in the main text, as shown by the solid orange curve in Fig. 34(a). It has a symmetric profile as shown in the fourth row of Fig. 34(b). While for the asymmetric solutions, one asymmetric solution is equivalent to the solution in the case with $C_2 = 0$, and another asymmetric solution also has an asymmetric profile but its voltage mainly distributes on the second site, i.e., the site B of the leftmost unit cell.

When the varactor diodes are modeled as the saturable nonlinearity, there is no solution in the case with $C_2 = 0$ because of the weak nonlinearity. In the case with $C_1 = 0$, we find two solutions: one symmetric solution and one antisymmetric solution. The symmetric solution corresponds to the topologically trivial edge solitons and the antisymmetric solution corresponds to the topologically nontrivial edge solitons, i.e., the self-induced topological edge states at the edge of a topologically trivial lattice. The frequencies of the edge solitons in a circuit lattice with the saturable nonlinearity are shown in Figs. 35(a) and 35(b). To compare with the theoretical and experimental excitation spectra, we also plot the dependence between the frequency and edge voltage v_1^{A}. From Figs. 35(a) and 35(b), the edge solitons do not exist in the linear limit. However, when the power/voltage is large enough, two branches for the edge solitons emerge where one branch reside in the SSH gap and the other one reside in the upper semi-infinite gap. The soliton profiles are shown in Fig. 35(c). Note that although the topologically trivial edge solitons are the continuations of the symmetric solution in the AC limit, the voltages at the first two sites shown in Fig. 35(c) is slightly asymmetric.

Based on the soliton profiles shown in Fig. 35(c), when we neglect the voltage at the first site, the topological edge soliton exhibits an antisymmetric voltage distribution across the two leftmost sites and resembles the linear topological edge states. Specifically, this topological edge soliton features a phase jump of π between neighboring cells and is primarily confined to the sublattice site B, accompanied by a decaying tail that approaches zero. Physically, this type of edge soliton can be understood as a nonlinearity-induced topological edge soliton in a topologically trivial lattice. The circuit

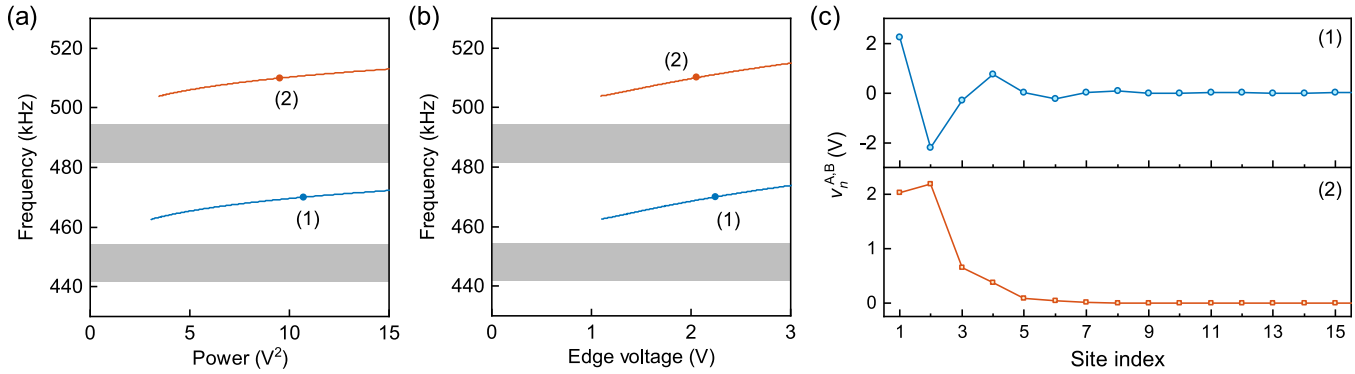

FIG. 35. Edge solitons in a topologically trivial lattice with saturable nonlinearity. (a), (b) Frequencies of the edge solitons, with solid blue curves representing the self-induced topological edge states and solid orange curves corresponding to the topologically trivial edge solitons. (c) Voltage distributions of the edge solitons indicated in panels (a), (b).

nonlinearity introduces a defect at site A of the leftmost unit cell, enabling the newly formed lattice to support the existence of a topological edge state that extends from site B of the leftmost unit cell to the infinite right end. Considering these properties, the antisymmetric solution obtained in the AC limit evolves into the topological edge soliton (for a more detailed discussion, see Appendix I 3). In contrast, for the topologically trivial edge soliton in a topologically trivial lattice, the voltage is predominantly localized on the two sites of the leftmost unit cell, without a phase jump between neighboring cells. These characteristics indicate that this type of edge soliton represents nonlinearity-induced localized modes, and thus, the symmetric solution obtained in the AC limit corresponds to the topologically trivial edge soliton.

2. Stability analysis of the edge solitons

We then study the stability analysis of both the topologically nontrivial and trivial edge solitons. Figure 36(a) shows the maximum growth rates of the self-induced topological edge states at the different frequencies. From the figure, the maximum growth rates are in the order of 10^{-3} when the soliton frequencies are near to the lower edge of the top bulk band. This region corresponds to the linearly unstable solitons. However, since we are interested in the localized self-induced topological edge states and the maximum frequency shifts of the solitons are limited by the experimental input voltage [see Fig. 35(b)], we carry out the temporal evolution of the self-induced topological edge states at the frequency of 470 kHz. Noises with ±2% random perturbations are added

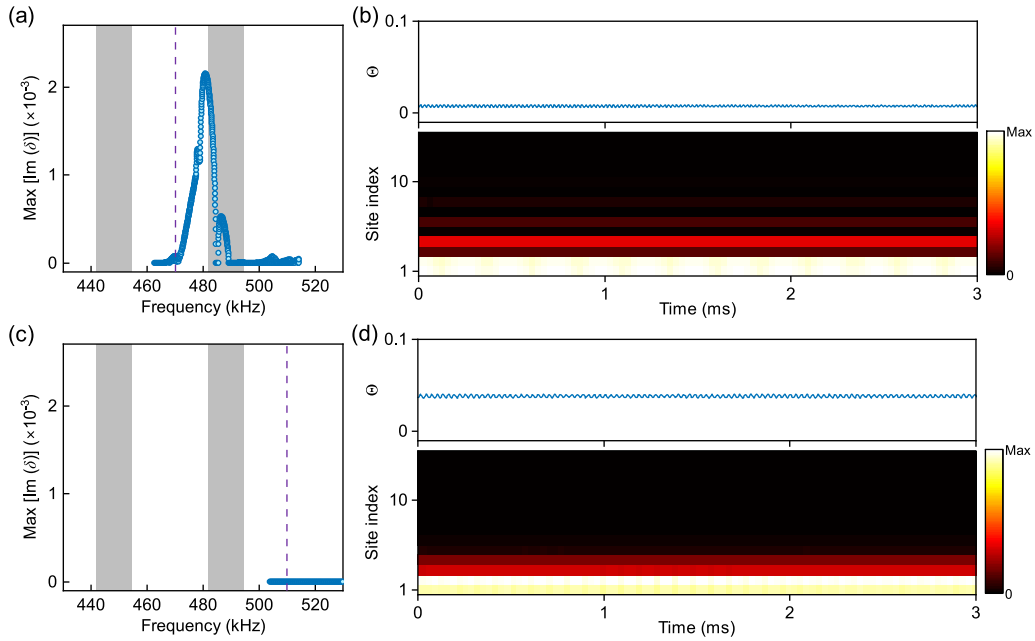

FIG. 36. Stability analysis of the edge solitons. (a) The maximum growth rates of the perturbed solutions of the self-induced topological edge states. (b) The temporal evolution of the self-induced topological edge state at the frequency indicated in panel (a). Noises with ±2% random perturbations are added to the initial input. (c), (d) Results for the topologically trivial edge solitons. In panels (a), (c), the gray areas denote the linear bulk bands.

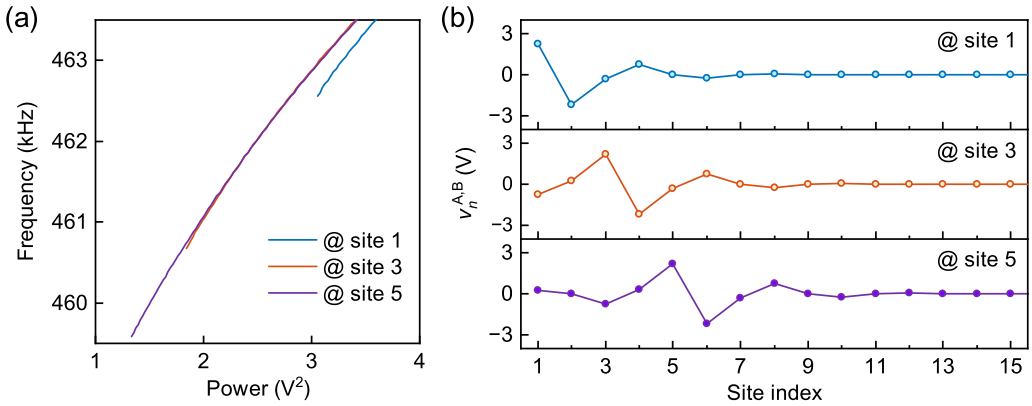

FIG. 37. Relation between the self-induced topological edge states and topological gap solitons. (a) Existence curves (the dependence between the frequency and soliton power) of a series of solitons residing at the different positions. (b) Voltage distributions of the different solitons at 470 kHz.

to the input amplitude. To quantitatively measure the mode stability/instability, we again use the asymmetry parameter Θ to characterize the voltage asymmetry between the sites 1 and 2, i.e., the first two sites of the topologically trivial SSH lattice. From the voltage distribution shown in Fig. 36(b), there are no apparent variations along the temporal evolution. The asymmetry parameters are in the order of 10^{-3}. These results imply that, although the unstable region exists, at least within the experimentally realizable parameter range, the self-induced topological edge states should be observable because of their weak instabilities.

The results for the stability analysis of the topologically trivial edge solitons are shown in Figs. 36(c) and 36(d). Compared to the self-induced topological edge states, the topologically trivial edge solitons have much smaller Max[Im(δ)] (in the order of 10^{-9}), implying that they are much more stable. We take the topologically trivial edge soliton at 510 kHz as an example and study its temporal evolution, again with $\pm 2\%$ noises added to the input. From Fig. 36(d), both the voltage distribution and asymmetry parameters confirm that the topologically trivial edge soliton is stable.

3. Physical interpretation of the self-induced topological edge states

The self-induced topological edge states can also be understood from the solution of the GP equation. Since the edge solitons mainly reside at the two sites of the first unit cell, we only consider the circuit nonlinearities at the leftmost two sites and neglect the nonlinearities at the other sites. With $V_m^{A,B}(T) = v_m^{A,B} e^{-i\bar{\omega}T}$, the governing equations reduce to

$$\bar{\omega} v_1^A = E_0 v_1^A + g\left(v_1^A\right) v_1^A + J_2 v_1^B, \tag{I4}$$

$$\bar{\omega} v_1^B = E_0 v_1^B + g\left(v_1^B\right) v_1^B + J_2 v_1^A + J_1 v_2^A, \tag{I5}$$

$$\bar{\omega} v_2^A = E_0 v_2^A + J_2 v_2^B + J_1 v_1^B, \tag{I6}$$

$$\bar{\omega} v_2^B = E_0 v_2^B + J_2 v_2^A + J_1 v_3^A, \tag{I7}$$

$$\ldots . \tag{I8}$$

We let $\bar{\omega} = E_0$ which implies that the frequency of the self-induced topological edge state equals to the frequency of the linear topological edge state in an SSH lattice, then the equations reduce to

$$g\left(v_1^A\right) v_1^A + J_2 v_1^B = 0, \tag{I9}$$

$$g\left(v_1^B\right) v_1^B + J_2 v_1^A + J_1 v_2^A = 0, \tag{I10}$$

$$J_2 v_2^B + J_1 v_1^B = 0, \tag{I11}$$

$$J_2 v_2^A + J_1 v_3^A = 0, \tag{I12}$$

$$\ldots . \tag{I13}$$

Considering the profile of the self-induced topological edge state, we have $v_m^B = (-\frac{J_1}{J_2})^{|m|-1} v_1^B$ and $v_m^A = 0$ for $m \geqslant 2$, and the equations further reduce to

$$g\left(v_1^A\right) v_1^A + J_2 v_1^B = 0, \tag{I14}$$

$$g\left(v_1^B\right) v_1^B + J_2 v_1^A = 0. \tag{I15}$$

The above two equations govern the voltage distributions at the leftmost two sites. Again considering the profile of the self-induced topological edge state, we have $v_1^A = -v_1^B$ and

$$g\left(v_1^{A,B}\right) = J_2. \tag{I16}$$

Thus, if Eq. (I16) has solutions, then the self-induced topological edge states can be interpreted by the solution of the GP equation. In other words, the self-induced topological edge states that reside at the edge of a topologically trivial lattice can be approximately mapped to the linear topological edge state of a semi-infinite SSH lattice.

To explain the relation between the self-induced topological edge states and topological gap solitons, we select the topological gap soliton at a given frequency and move it from the lattice bulk to the left edge. Due to the discrete translational symmetry, the soliton profile is invariant when the soliton peak is far from the edge. However, the discrete translational symmetry is broken at the lattice edge because the SSH lattice that we study has an open boundary. The soliton profile is changed due to the presence of the edge. Figure 37(a) shows the existence curves (the dependence between the frequency and soliton power) of a series of solitons residing at the different positions, and Fig. 37(b) correspond

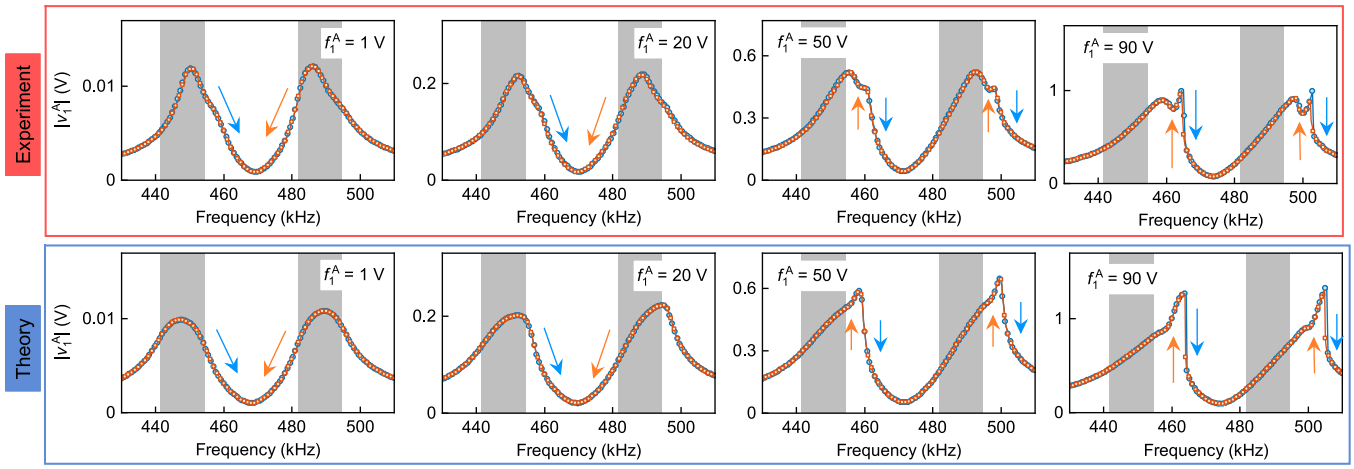

FIG. 38. Voltage spectra at the edge node when the topologically trivial circuit lattice is excited with the driving voltage f_1^A. The first and second rows show the results from the experiment and GP equation, respectively. In all the rows, the blue and orange curves correspond to the frequency sweep along the two opposite directions (denoted by the blue and orange arrows).

to the voltage distributions of the different solitons. From Fig. 37(a), a power threshold is induced when moving the topological gap soliton toward the edge.

APPENDIX J: EXPERIMENTAL MEASUREMENT OF THE SELF-INDUCED TOPOLOGICAL EDGE STATES

In this Appendix, we give more experimental results of the edge solitons in a topologically trivial lattice, particularly the self-induced topological edge states.

Theoretically, we solve the driven-dissipative GP equation with the driven terms $F_m^A(t) = \delta_{m,1} f_0^A \exp(-i\bar{\omega}T)$ and $F_m^B(t) = 0$, i.e., only the edge site is excited. Then the equations are solved by following the same procedure. Note that to have a better comparison with the experimental results, in the topologically trivial lattice, the series resistance of inductors is set as $R_L = 650$ mΩ. In the theoretical calculations, the lattice consists of $N = 120$ unit cells, indicating that it contains an even number of lattice sites.

We fabricate another nonlinear SSH circuit lattice with the intracell hopping J_2 and intercell hopping J_1. The experimental circuit lattice has the parameter $N = 12$, which corresponds to a total of 24 lattice sites. In the linear limit, this lattice is a topologically trivial lattice. Experimentally, we just change the positions of C_1 and C_2, and observe the edge solitons. We plot the experimental and theoretical voltage spectra at the edge node in Fig. 38. From the fist column, when the driving voltage is small with $f_1^A = 1$ V, two spectrum peaks appear in the bulk bands. Since this lattice has no topological edge state in the linear limit, there is no peak in the SSH gap. Meanwhile, since the nonlinearity-induced topologically trivial solitons usually exist above a power threshold, there is also no peak in the upper semi-infinite gap. These results imply that, in the linear limit, only the bulk states are excited under the external driving, in contrast to the spectra for a topologically nontrivial lattice where the topological edge state is excited. When the driving voltage increases to $f_1^A = 20$ V, the resonant frequencies of the two peaks exhibit the blue shift, as shown by the second column of Fig. 38. The resonant frequencies of the two peaks reside near the band edges and there are only two peaks in total.

Then we continue to enhance the circuit nonlinearity by increasing the driving voltage. For $f_1^A = 50$ V, the original two peaks near the band edges shrink and two new peaks appear, as shown in the third column. The peak corresponding to the topologically nontrivial edge soliton (i.e., the self-induced topological edge states) reside in the SSH gap, and the peak corresponding to the topologically trivial edge soliton reside in the upper semi-infinite gap. The small discrepancy between the experimental and theoretical results is due to the circuit component errors. When the driving voltage further increases to $f_1^A = 90$ V, from the last column, the peaks for the edge solitons become more pronounced. Specifically, we observe a clear bistable response for the peak corresponding to the topologically trivial edge soliton. Note that, as shown in Fig. 38, the experimental measurement results exhibit deviations from the theoretical predictions at higher input voltages, primarily due to increased series resistance of the inductors and reduced driving voltages supplied by the voltage source.

According to both the experimental and theoretical results, the edge solitons appear when the driving voltage is approximately larger than 50 V. However, the corresponding voltages at the edge sites are smaller than the theoretically predicted values obtained from the GP equation shown in Fig. 35(b). Only when the driving voltage increases to 80 V, the result from the driven-dissipative system agrees with the prediction from Fig. 35(b). The disagreement for the driving voltage between 50 V to 80 V may be possibly induced by the excitation of the higher order edge solitons, which cannot be derived simply by setting $C_1 = 0$ or $C_2 = 0$ in the AC limit. In our study, we neglect these higher order edge solitons.

To clearly show the emergence of the peak that corresponds to the self-induced topological edge state, Fig. 39 shows the theoretical excitation spectra when the input voltage varies from 20 V to 50 V. The series resistance of inductors is now set as $R_L = 500$ mΩ. For clarity, we only show the spectra when the driving frequency is swept from low to high. From the figure, a new peak is gradually appeared in the SSH gap. Such observation implies the power/voltage

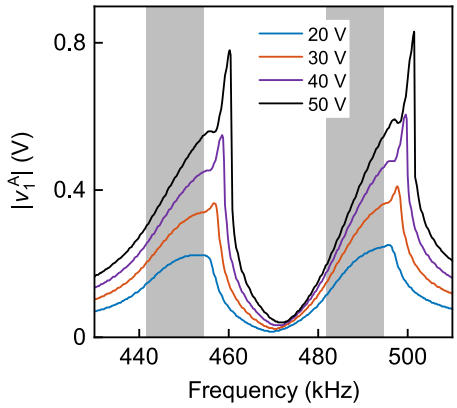

FIG. 39. Theoretical excitation spectra for the self-induced topological edge states. For simplicity, we only show the spectra when the driving frequency is swept from low to high. The gray areas denote the linear bulk bands.

threshold of the existence of the self-induced topological edge states.

To explain the origin of the two peaks, we also measure the voltage distributions at the corresponding resonant frequencies. For the peak in the SSH gap, when we neglect the voltage at the first site, the voltage distribution exhibits a phase jump of π among the neighboring cells and the voltages at the site A (except the site A in the first unit cell) are nearly zero. Thus, this peak corresponds to the self-induced topological edge state in a topologically trivial lattice. For the peak in the upper semi-infinite gap, the voltage is mainly localized on the two sites of the leftmost unit cell with nearly equal amplitudes between the two sites. From the phase distribution, the voltages at the different sites have nearly equal phases, in strong contrast to the phase jump observed for the peak in the SSH gap. Thus, the peak in the semi-infinite gap corresponds to the nonlinearity induced localization mode, i.e., the topologically trivial edge soliton in a topologically trivial lattice. Our experimental observation validates the existence of both the topologically nontrivial and trivial edge solitons in a topologically trivial lattice, confirming the theoretical predication.

Figure 40 shows the edge voltages $|v_1^A|$, PRs, and sublattice polarizations S' of the self-induced topological edge states. From Fig. 40(a), no edge solitons can be excited near the linear limit. Both the topologically nontrivial and trivial edge solitons exist when the edge voltage is above the certain threshold values. This property is totally different to the thresholdless excitation of the nonlinear topological edge states. Since the increased circuit nonlinearity induces the decreased grounding capacitance, the frequencies of the edge solitons in a topologically trivial lattice also exhibit the blue shift. Besides, different to the nonlinear topological edge states where the nonlinearity weakens their localizations, the self-induced topological edge states become more localized with the increased nonlinearity. Since the self-induced topological edge states are nonlinearity induced, a stronger nonlinearity results in the greater voltage localization, as shown in Fig. 40(b). Meanwhile, from Fig. 40(c), with the increasing of the frequency, the sublattice pseudospin S' approaches -1, implying a greater voltage localization on the sublattice site B. Note that here S' is defined by neglecting the voltage at the first site. This observation further validates the origin of the self-induced topological edge states. Considering the fact that a linear topological edge state has $S = -1$, a stronger circuit nonlinearity leads to a larger defect at the site A of the leftmost unit cell, and the self-induced topological edge state is more close to the linear topological edge state distributed from the site B of the leftmost unit cell to the right infinite end. For the topologically trivial edge solitons, both the experimental and theoretical results show that the topologically trivial edge solitons have $S \approx 0$, regardless of the state frequencies. This observation validates that the topologically trivial edge solitons in a topologically trivial lattice are the nonlinearity induced localization modes and they always reside at the two sites of the first unit cell with the equal amplitudes.

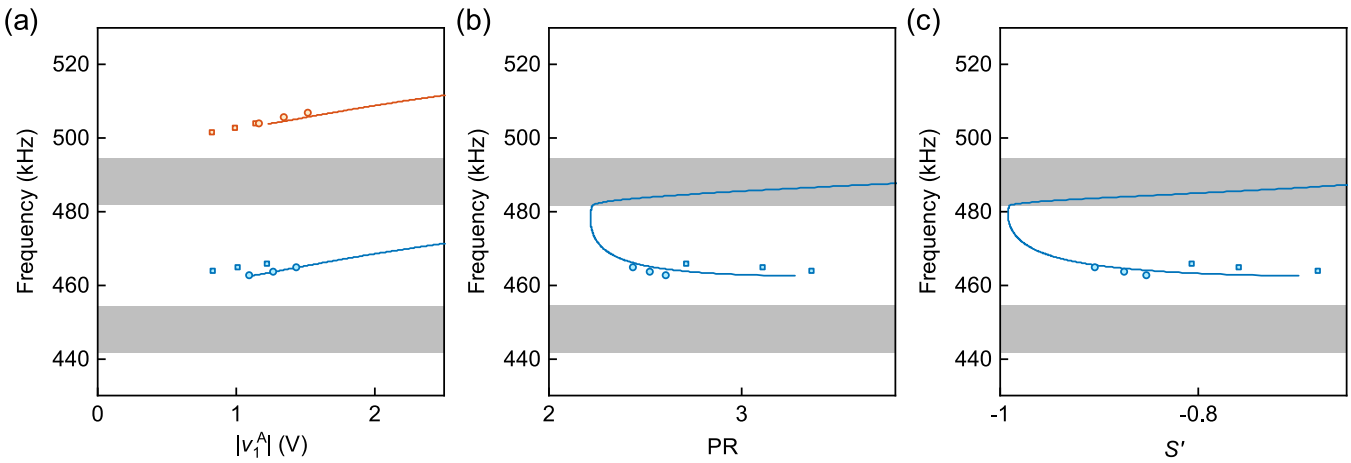

FIG. 40. Edge voltages $|v_1^A|$, participation ratios (PRs), and sublattice polarizations S' of the self-induced topological edge states. The squares and circles correspond to the experimental and theoretical results, respectively. The curves denote the result calculated from the GP equation without the driven-dissipative terms, and the gray areas correspond to the linear bulk bands. In panel (a), we also plot the results for the topologically trivial edge solitons (shown in orange).

APPENDIX K: CALCULATION OF THE NONLINEAR BERRY PHASE

Starting from Eqs. (B26) and (B27), under the periodic boundary condition, we assume that the solutions can still be expressed in the form of Bloch functions: $V_m^{\mathrm{A,B}} = \phi_{\mathrm{A,B}} \exp(\mathrm{i}km - \mathrm{i}\bar{\omega}T)$. Substituting this Bloch ansatz into Eqs. (B26) and (B27), we obtain

$$(J_1 + J_2 e^{-\mathrm{i}k})\phi_{\mathrm{B}} + g(\phi_{\mathrm{A}})\phi_{\mathrm{A}} = (\bar{\omega} - E_0)\phi_{\mathrm{A}}, \tag{K1}$$

$$(J_1 + J_2 e^{\mathrm{i}k})\phi_{\mathrm{A}} + g(\phi_{\mathrm{B}})\phi_{\mathrm{B}} = (\bar{\omega} - E_0)\phi_{\mathrm{B}}. \tag{K2}$$

These equations define the corresponding Bloch Hamiltonian of a nonlinear system, which depends on the wave functions $\phi_{\mathrm{A,B}}$. In addition to Eqs. (K1) and (K2), we impose the following constraint:

$$|\phi_{\mathrm{A}}|^2 + |\phi_{\mathrm{B}}|^2 = w, \tag{K3}$$

which is analogous to the normalization condition of eigenstates in linear systems, ensuring that the amplitudes of the wave functions remain constant regardless of the wavenumber k [81]. By numerically solving Eqs. (K1)–(K3), we obtain both the generally complex-valued $\phi_{\mathrm{A,B}}$ and the real-valued normalized frequency $\bar{\omega}$.

To provide better insight, we also present some analytical results. In the linear regime with $g = 0$, the eigenvalue problem has been solved, with Fig. 18(c) illustrating the band structure and Eq. (F1) giving the expression for $\bar{\omega}$. The corresponding eigenvectors are

$$(\phi_{\mathrm{A}}, \phi_{\mathrm{B}}) = \frac{1}{\sqrt{2}}\left(1, \frac{\bar{\omega} - E_0}{J_1 + J_2 e^{-\mathrm{i}k}}\right). \tag{K4}$$

For simplicity, we define $J_1 + J_2 e^{\pm \mathrm{i}k} = J_0 e^{\pm \mathrm{i}\theta}$, where $J_0 = |J_1 + J_2 e^{\pm \mathrm{i}k}|$ and $\theta = \arg(J_1 + J_2 e^{\mathrm{i}k})$. Then the eigenvalues and eigenvectors can be written as

$$\bar{\omega} = E_0 \pm J_0, \tag{K5}$$

$$(\phi_{\mathrm{A}}, \phi_{\mathrm{B}}) = \frac{1}{\sqrt{2}}(1, \pm e^{\mathrm{i}\theta}). \tag{K6}$$

In the nonlinear regime, using the same definitions of J_0 and θ, Eqs. (K1)–(K3) can be rewritten as

$$[\bar{\omega} - E_0 - g(\phi_{\mathrm{A}})]\phi_{\mathrm{A}} = J_0 e^{-\mathrm{i}\theta}\phi_{\mathrm{B}}, \tag{K7}$$

$$[\bar{\omega} - E_0 - g(\phi_{\mathrm{B}})]\phi_{\mathrm{B}} = J_0 e^{\mathrm{i}\theta}\phi_{\mathrm{A}}, \tag{K8}$$

$$|\phi_{\mathrm{A}}|^2 + |\phi_{\mathrm{B}}|^2 = w. \tag{K9}$$

Multiplying the left-hand side of Eq. (K7) by the right-hand side of Eq. (K8), and vice versa, one obtains

$$[\bar{\omega} - E_0 - g(\phi_{\mathrm{A}})]\phi_{\mathrm{A}}^2 = [\bar{\omega} - E_0 - g(\phi_{\mathrm{B}})]e^{-2\mathrm{i}\theta}\phi_{\mathrm{B}}^2. \tag{K10}$$

Note that this equation holds because $J_0 e^{\mathrm{i}\theta}$ is generally nonzero.

To match the arguments on both sides of Eq. (K10), the wave functions $\phi_{\mathrm{A,B}}$ can be expressed as

$$\phi_{\mathrm{A}} = r_{\mathrm{A}} e^{\mathrm{i}\phi}, \tag{K11}$$

$$\phi_{\mathrm{B}} = \pm r_{\mathrm{B}} e^{\mathrm{i}(\phi+\theta)}, \tag{K12}$$

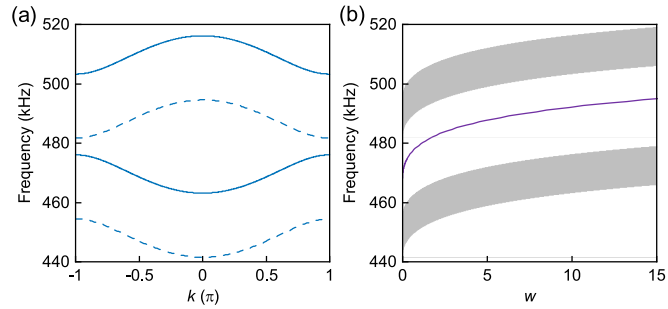

FIG. 41. Band structure in the nonlinear regime. (a) Band structure calculated at $w = 10$ (solid curves). For comparison, the band structure in the linear regime with $g = 0$ is shown as dashed curves. (b) Frequencies of the nonlinear topological edge states for various values of w. The gray shaded areas represent the corresponding nonlinear bulk bands.

where r_{A} and r_{B} are both real and positive. With these definitions, Eqs. (K11) and (K12) are further reduced to

$$[\bar{\omega} - E_0 - g(r_{\mathrm{A}})]r_{\mathrm{A}} = \pm J_0 r_{\mathrm{B}}, \tag{K13}$$

$$[\bar{\omega} - E_0 - g(r_{\mathrm{B}})]r_{\mathrm{B}} = \pm J_0 r_{\mathrm{A}}, \tag{K14}$$

$$r_{\mathrm{A}}^2 + r_{\mathrm{B}}^2 = w. \tag{K15}$$

Meanwhile, substituting Eqs. (K11) and (K12) into Eq. (K10) yields

$$[\bar{\omega} - E_0 - g(r_{\mathrm{A}})]r_{\mathrm{A}}^2 = [\bar{\omega} - E_0 - g(r_{\mathrm{B}})]r_{\mathrm{B}}^2, \tag{K16}$$

which admits two types of solutions: $r_{\mathrm{A}} = r_{\mathrm{B}}$ and $r_{\mathrm{A}} \neq r_{\mathrm{B}}$, respectively. For the case $r_{\mathrm{A}} = r_{\mathrm{B}}$, considering Eqs. (K13)–(K15) leads to

$$r_{\mathrm{A}} = r_{\mathrm{B}} = \sqrt{\frac{w}{2}}, \tag{K17}$$

$$\bar{\omega} = E_0 + g\left(\sqrt{\frac{w}{2}}\right) \pm J_0. \tag{K18}$$

Thus, the corresponding eigenvalues and eigenvectors are

$$\bar{\omega} = E_0 + g\left(\sqrt{\frac{w}{2}}\right) \pm J_0, \tag{K19}$$

$$(\psi_{\mathrm{A}}, \psi_{\mathrm{B}}) = \sqrt{\frac{w}{2}}(1, \pm e^{i\theta}). \tag{K20}$$

For the case $r_{\mathrm{A}} \neq r_{\mathrm{B}}$, Eq. (K16) yields an alternative expression for $\bar{\omega}$:

$$\bar{\omega} = E_0 + \frac{g(r_{\mathrm{A}})r_{\mathrm{B}}^2 - g(r_{\mathrm{B}})r_{\mathrm{A}}^2}{r_{\mathrm{A}}^2 - r_{\mathrm{B}}^2} + g(r_{\mathrm{A}}) + g(r_{\mathrm{B}}). \tag{K21}$$

However, obtaining explicit analytical forms for r_{A} and r_{B} is challenging. After numerically solving Eqs. (K1)–(K3), we find that solutions with $r_{\mathrm{A}} \neq r_{\mathrm{B}}$ are excluded due to the saturable nonlinearity inherent in our model.

We focus on the SSH lattice illustrated in Fig. 1(a), replacing its boundary condition with a periodic boundary. The intracell and intercell coupling capacitors are maintained as $C_1 = 180$ pF and $C_2 = 560$ pF, respectively. Figure 41(a) shows the band structure for $w = 10$. Compared to the linear

band structure presented in Fig. 18(c), the band structure in the nonlinear regime (denoted by the solid curves) displays a vertical shift, which is consistent with the prediction of Eq. (K19). For reference, the linear band structure with $g = 0$ is represented by dashed curves. However, differing from the results reported in Ref. [81], as w increases, the energy (frequency) shift of our nonlinear band structure saturates, and no nonlinearity-induced flat bands corresponding to Eq. (K21) emerge. These discrepancies arise because the nonlinear terms in Eqs. (K1) and (K2) describe saturable nonlinearity. We have verified that if the saturable nonlinearity is replaced by a non-saturable form, where the capacitance of the varactor diodes is modeled according to Eq. (A7), additional nonlinearity-induced flat bands indeed appear.

Following the definitions of the time-reversal and space-inversion operators introduced in Ref. [81], we find that our nonlinear SSH model, as given by Eqs. (K1) and (K2), also respects both time-reversal and space-inversion symmetries. Similarly, using the eigenvectors provided in Eq. (K20), the nonlinear Berry phase defined by

$$v(w) = -\frac{i}{w}\int_{-\pi}^{\pi}\left\langle u_k\left|\frac{\partial u_k}{\partial k}\right.\right\rangle dk \tag{K22}$$

equals π for any given value of w. Here, $|u_k\rangle = (\phi_A, \phi_B)^T$ denotes the Bloch state, and T is the transpose operator. According to the bulk-boundary correspondence formulated in Ref. [81], a nonzero Berry phase corresponds to the existence of localized gapless modes satisfying $|v_1^A|^2 + |v_1^B|^2 = w$. As shown in Fig. 41(b), the nonlinear topological edge states we identified (denoted by the solid curve) consistently lie within the mid-gap described by Eq. (K20). The gray shaded areas represent the corresponding nonlinear bulk bands. This implies that the nonlinear topological edge states presented in Figs. 3(a)–3(c) can be fully characterized within the theoretical framework proposed in Ref. [81].

By exchanging the values of the intracell and intercell couplings, we find that the nonlinear band structure remains identical to that shown in Fig. 41(a). However, the nonlinear Berry phase defined in Eq. (K22) becomes zero, indicating the absence of localized gapless modes. When two SSH lattices with $w = \pi$ and $w = 0$ are connected, a domain wall is formed, analogous to the linear regime. Consequently, the emergence of the nonlinear topological edge states observed in Figs. 3(d) and 3(e) can also be explained within this framework.

[1] M. Z. Hasan and C. L. Kane, Colloquium: Topological insulators, Rev. Mod. Phys. **82**, 3045 (2010).

[2] X.-L. Qi and S.-C. Zhang, Topological insulators and superconductors, Rev. Mod. Phys. **83**, 1057 (2011).

[3] G.-Q. Zhao, S. Li, W. B. Rui, C. M. Wang, H.-Z. Lu, and X. C. Xie, 3D quantum Hall effect in a topological nodal-ring semimetal, Quantum Front. **2**, 22 (2023).

[4] O. Breunig and Y. Ando, Opportunities in topological insulator devices, Nat. Rev. Phys. **4**, 184 (2022).

[5] F. Zhan, R. Chen, Z. Ning, D.-S. Ma, Z. Wang, D.-H. Xu, and R. Wang, Perspective: Floquet engineering topological states from effective models towards realistic materials, Quantum Front. **3**, 21 (2024).

[6] G. Ma, M. Xiao, and C. T. Chan, Topological phases in acoustic and mechanical systems, Nat. Rev. Phys. **1**, 281 (2019).

[7] H. Xue, Y. Yang, and B. Zhang, Topological acoustics, Nat. Rev. Mater. **7**, 974 (2022).

[8] N. R. Cooper, J. Dalibard, and I. B. Spielman, Topological bands for ultracold atoms, Rev. Mod. Phys. **91**, 015005 (2019).

[9] Z.-K. Lin, Q. Wang, Y. Liu, H. Xue, B. Zhang, Y. Chong, and J.-H. Jiang, Topological phenomena at defects in acoustic, photonic and solid-state lattices, Nat. Rev. Phys. **5**, 483 (2023).

[10] B. Xie, H.-X. Wang, X. Zhang, P. Zhan, J.-H. Jiang, M. Lu, and Y. Chen, Higher-order band topology, Nat. Rev. Phys. **3**, 520 (2021).

[11] T. Shah, C. Brendel, V. Peano, and F. Marquardt, Colloquium: Topologically protected transport in engineered mechanical systems, Rev. Mod. Phys. **96**, 021002 (2024).

[12] L. Lu, J. D. Joannopoulos, and M. Soljačić, Topological photonics, Nat. Photonics **8**, 821 (2014).

[13] A. B. Khanikaev and G. Shvets, Two-dimensional topological photonics, Nat. Photonics **11**, 763 (2017).

[14] X.-C. Sun, C. He, X.-P. Liu, M.-H. Lu, S.-N. Zhu, and Y.-F. Chen, Two-dimensional topological photonic systems, Prog. Quantum Electron. **55**, 52 (2017).

[15] T. Ozawa, H. M. Price, A. Amo, N. Goldman, M. Hafezi, L. Lu, M. C. Rechtsman, D. Schuster, J. Simon, O. Zilberberg, and I. Carusotto, and Topological Photonics, Topological photonics, Rev. Mod. Phys. **91**, 015006 (2019).

[16] M. Kim, Z. Jacob, and J. Rho, Recent advances in 2D, 3D and higher-order topological photonics, Light: Sci. Appl. **9**, 130 (2020).

[17] H. Yang, L. Song, Y. Cao, and P. Yan, Circuit realization of topological physics, Phys. Rep. **1093**, 1 (2024).

[18] H. Sahin, M. B. A. Jalil, and C. H. Lee, Topolectrical circuits—Recent experimental advances and developments, APL Electron. Dev. **1**, 021503 (2025).

[19] M. Yang, J.-S. Xu, C.-F. Li, and G.-C. Guo, Simulating topological materials with photonic synthetic dimensions in cavities, Quantum Front. **1**, 10 (2022).

[20] Y. Liu, K. Li, W. Liu, Z. Zhang, Y. Cheng, and X. Liu, Observation of chiral Landau levels in two-dimensional acoustic system, Quantum Front. **3**, 26 (2024).

[21] D. Smirnova, D. Leykam, Y. Chong, and Y. Kivshar, Nonlinear topological photonics, Appl. Phys. Rev. **7**, 021306 (2020).

[22] A. Szameit and M. C. Rechtsman, Discrete nonlinear topological photonics, Nat. Phys. **20**, 905 (2024).

[23] M. J. Ablowitz, C. W. Curtis, and Y.-P. Ma, Linear and nonlinear traveling edge waves in optical honeycomb lattices, Phys. Rev. A **90**, 023813 (2014).

[24] Y. Lumer, M. C. Rechtsman, Y. Plotnik, and M. Segev, Instability of bosonic topological edge states in the presence of interactions, Phys. Rev. A **94**, 021801(R) (2016).

[25] Y. V. Kartashov and D. V. Skryabin, Modulational instability and solitary waves in polariton topological insulators, Optica **3**, 1228 (2016).

[26] Y. V. Kartashov and D. V. Skryabin, Bistable topological insulator with exciton-polaritons, Phys. Rev. Lett. **119**, 253904 (2017).

[27] D. A. Dobrykh, A. V. Yulin, A. P. Slobozhanyuk, A. N. Poddubny, and Y. S. Kivshar, Nonlinear control of electromagnetic topological edge states, Phys. Rev. Lett. **121**, 163901 (2018).

[28] T. Tuloup, R. W. Bomantara, C. H. Lee, and J. Gong, Nonlinearity induced topological physics in momentum space and real space, Phys. Rev. B **102**, 115411 (2020).

[29] M. Guo, S. Xia, N. Wang, D. Song, Z. Chen, and J. Yang, Weakly nonlinear topological gap solitons in Su-Schrieffer-Heeger photonic lattices, Opt. Lett. **45**, 6466 (2020).

[30] N. Pernet, P. St-Jean, D. D. Solnyshkov, G. Malpuech, N. C. Zambon, Q. Fontaine, B. Real, O. Jamadi, A. Lemaître, M. Morassi, L. L. Gratiet, T. Baptiste, A. Harouri, I. Sagnes, A. Amo, S. Ravets, and J. Bloch, Gap solitons in a one-dimensional driven-dissipative topological lattice, Nat. Phys. **18**, 678 (2022).

[31] Y. V. Kartashov *et al.*, Observation of edge solitons in topological trimer arrays, Phys. Rev. Lett. **128**, 093901 (2022).

[32] Y.-P. Ma and H. Susanto, Topological edge solitons and their stability in a nonlinear Su-Schrieffer-Heeger model, Phys. Rev. E **104**, 054206 (2021).

[33] M. Ezawa, Nonlinearity-induced transition in the nonlinear Su-Schrieffer-Heeger model and a nonlinear higher-order topological system, Phys. Rev. B **104**, 235420 (2021).

[34] S. Xia, D. Jukić, N. Wang, D. Smirnova, L. Smirnov, L. Tang, D. Song, A. Szameit, D. Leykam, J. Xu, Z. Chen, and H. Buljan, Nontrivial coupling of light into a defect: The interplay of nonlinearity and topology, Light: Sci. Appl. **9**, 147 (2020).

[35] S. Xia, D. Kaltsas, D. Song, I. Komis, J. Xu, A. Szameit, H. Buljan, K. G. Makris, and Z. Chen, Nonlinear tuning of PT symmetry and non-Hermitian topological states, Science **372**, 72 (2021).

[36] R. Li, X. Kong, W. Wang, Y. Wang, Y. Jia, H. Tao, P. Li, Y. Liu, and B. A. Malomed, Observation of edge solitons and transitions between them in a trimer circuit lattice, Commun. Phys. **8**, 342 (2025).

[37] D. Leykam and Y. D. Chong, Edge solitons in nonlinear-photonic topological insulators, Phys. Rev. Lett. **117**, 143901 (2016).

[38] S. K. Ivanov, Y. V. Kartashov, A. Szameit, L. Torner, and V. V. Konotop, Vector topological edge solitons in Floquet insulators, ACS Photonics **7**, 735 (2020).

[39] Z. Zhang, R. Wang, Y. Zhang, Y. V. Kartashov, F. Li, H. Zhong, H. Guan, K. Gao, F. Li, Y. Zhang, and M. Xiao, Observation of edge solitons in photonic graphene, Nat. Commun. **11**, 1902 (2020).

[40] S. Mukherjee and M. C. Rechtsman, Observation of unidirectional solitonlike edge states in nonlinear Floquet topological insulators, Phys. Rev. X **11**, 041057 (2021).

[41] S. K. Ivanov, Y. V. Kartashov, M. Heinrich, A. Szameit, L. Torner, and V. V. Konotop, Topological dipole Floquet solitons, Phys. Rev. A **103**, 053507 (2021).

[42] Z. Shi, M. Zuo, H. Li, D. Preece, Y. Zhang, and Z. Chen, Topological edge states and solitons on a dynamically tunable domain wall of two opposing helical waveguide arrays, ACS Photonics **8**, 1077 (2021).

[43] M. Ezawa, Nonlinearity-induced chiral solitonlike edge states in Chern systems, Phys. Rev. B **106**, 195423 (2022).

[44] M. S. Kirsch, Y. Zhang, M. Kremer, L. J. Maczewsky, S. K. Ivanov, Y. V. Kartashov, L. Torner, D. Bauer, A. Szameit, and M. Heinrich, Nonlinear second-order photonic topological insulators, Nat. Phys. **17**, 995 (2021).

[45] Z. Hu, D. Bongiovanni, D. Jukić, E. Jajtić, S. Xia, D. Song, J. Xu, R. Morandotti, H. Buljan, and Z. Chen, Nonlinear control of photonic higher-order topological bound states in the continuum, Light: Sci. Appl. **10**, 164 (2021).

[46] R. Li, W. Wang, Y. Jia, Y. Liu, P. Li, and B. A. Malomed, Nonlinear quadrupole topological insulators, Chaos, Solitons Fractals **207**, 118044 (2026).

[47] Y. Lumer, Y. Plotnik, M. C. Rechtsman, and M. Segev, Self-localized states in photonic topological insulators, Phys. Rev. Lett. **111**, 243905 (2013).

[48] D. D. Solnyshkov, O. Bleu, B. Teklu, and G. Malpuech, Chirality of topological gap solitons in bosonic dimer chains, Phys. Rev. Lett. **118**, 023901 (2017).

[49] A. N. Poddubny and D. A. Smirnova, Ring Dirac solitons in nonlinear topological systems, Phys. Rev. A **98**, 013827 (2018).

[50] D. A. Smirnova, L. A. Smirnov, D. Leykam, and Y. S. Kivshar, Topological edge states and gap solitons in the nonlinear Dirac model, Laser Photonics Reviews **13**, 1900223 (2019).

[51] J. L. Marzuola, M. Rechtsman, B. Osting, and M. Bandres, Bulk soliton dynamics in bosonic topological insulators, Phys. Rev. A **113**, 033519 (2026).

[52] S. Mukherjee and M. C. Rechtsman, Observation of Floquet solitons in a topological bandgap, Science **368**, 856 (2020).

[53] R. Li, X. Kong, D. Hang, G. Li, H. Hu, H. Zhou, Y. Jia, P. Li, and Y. Liu, Topological bulk solitons in a nonlinear photonic Chern insulator, Commun. Phys. **5**, 275 (2022).

[54] Y. V. Kartashov, B. A. Malomed, and L. Torner, Solitons in nonlinear lattices, Rev. Mod. Phys. **83**, 247 (2011).

[55] F. Lederer, G. I. Stegeman, D. N. Christodoulides, G. Assanto, M. Segev, and Y. Silberberg, Discrete solitons in optics, Phys. Rep. **463**, 1 (2008).

[56] L. Wang, Z. Yan, Y. Zhu, and J. Zeng, Gap solitons and vortices in two-dimensional spin-orbit-coupled Bose-Einstein condensates loaded onto moiré optical lattices, Quantum. Front. **4**, 9 (2025).

[57] C. Jörg, M. Jürgensen, S. Mukherjee, and M. C. Rechtsman, Optical control of topological end states via soliton formation in a 1D lattice, Nanophotonics **14**, 769 (2025).

[58] W. P. Su, J. R. Schrieffer, and A. J. Heeger, Solitons in polyacetylene, Phys. Rev. Lett. **42**, 1698 (1979).

[59] Y. Hadad, J. C. Soric, A. B. Khanikaev, and A. Alù, Self-induced topological protection in nonlinear circuit arrays, Nat. Electron. **1**, 178 (2018).

[60] Y. Wang, L.-J. Lang, C. H. Lee, B. Zhang, and Y. D. Chong, Topologically enhanced harmonic generation in a nonlinear transmission line metamaterial, Nat. Commun. **10**, 1102 (2019).

[61] F. Zangeneh-Nejad and R. Fleury, Nonlinear second-order topological insulators, Phys. Rev. Lett. **123**, 053902 (2019).

[62] T. Kotwal, F. Moseley, A. Stegmaier, S. Imhof, H. Brand, T. Kießling, R. Thomale, H. Ronellenfitsch, and J. Dunkel, Active topolectrical circuits, Proc. Natl. Acad. Sci. USA **118**, e2106411118 (2021).

[63] H. Hohmann, T. Hofmann, T. Helbig, S. Imhof, H. Brand, L. K. Upreti, A. Stegmaier, A. Fritzsche, T. Müller, U.

Schwingenschlögl, C. H. Lee, M. Greiter, L. W. Molenkamp, T. Kießling, and R. Thomale, Observation of cnoidal wave localization in nonlinear topolectric circuits, Phys. Rev. Res. **5**, L012041 (2023).

[64] H. Sahin, H. Akgün, Z. B. Siu, S. M. Rafi-Ul-Islam, J. F. Kong, M. B. A. Jalil, and C. H. Lee, Protected chaos in a topological lattice, Adv. Sci. **12**, e03216 (2025).

[65] D. Bongiovanni, D. Jukić, Z. Hu, F. Lunić, Y. Hu, D. Song, R. Morandotti, Z. Chen, and H. Buljan, Dynamically emerging topological phase transitions in nonlinear interacting soliton lattices, Phys. Rev. Lett. **127**, 184101 (2021).

[66] P. Delplace, D. Ullmo, and G. Montambaux, Zak phase and the existence of edge states in graphene, Phys. Rev. B **84**, 195452 (2011).

[67] C. Poli, M. Bellec, U. Kuhl, F. Mortessagne, and H. Schomerus, Selective enhancement of topologically induced interface states in a dielectric resonator chain, Nat. Commun. **6**, 6710 (2015).

[68] T. Kitagawa, M. A. Broome, A. Fedrizzi, M. S. Rudner, E. Berg, I. Kassal, A. Aspuru-Guzik, E. Demler, and A. G. White, Observation of topologically protected bound states in photonic quantum walks, Nat. Commun. **3**, 882 (2012).

[69] O. Morsch and M. Oberthaler, Dynamics of Bose-Einstein condensates in optical lattices, Rev. Mod. Phys. **78**, 179 (2006).

[70] Y. V. Kartashov, G. E. Astrakharchik, B. A. Malomed, and L. Torner, Frontiers in multidimensional self-trapping of nonlinear fields and matter, Nat. Rev. Phys. **1**, 185 (2019).

[71] J. K. Asbóth, L. Oroszlány, and A. Pályi, *A Short Course on Topological Insulators* (Springer International Publishing, Cham, 2016), Vol. 919.

[72] Y. Hadad, A. B. Khanikaev, and A. Alù, Self-induced topological transitions and edge states supported by nonlinear staggered potentials, Phys. Rev. B **93**, 155112 (2016).

[73] D. Zhou, D. Z. Rocklin, M. Leamy, and Y. Yao, Topological invariant and anomalous edge modes of strongly nonlinear systems, Nat. Commun. **13**, 3379 (2022).

[74] J. Tang, F. Ma, F. Li, H. Guo, and D. Zhou, Strongly nonlinear topological phases of cascaded topoelectrical circuits, Front. Phys. **18**, 33311 (2023).

[75] K. Sone, M. Ezawa, Z. Gong, T. Sawada, N. Yoshioka, and T. Sagawa, Transition from the topological to the chaotic in the nonlinear Su-Schrieffer-Heeger model, Transition from the topological to the chaotic in the nonlinear Su-Schrieffer-Heeger model, Nat. Commun. **16**, 422 (2025).

[76] T. A. Loring, K-theory and pseudospectra for topological insulators, Ann. Phys. **356**, 383 (2015).

[77] A. Cerjan and T. A. Loring, An operator-based approach to topological photonics, Nanophotonics **11**, 4765 (2022).

[78] W. Cheng, A. Cerjan, S.-Y. Chen, E. Prodan, T. A. Loring, and C. Prodan, Revealing topology in metals using experimental protocols inspired by K-theory, Nat. Commun. **14**, 3071 (2023).

[79] K. Bai, J.-Z. Li, T.-R. Liu, L. Fang, D. Wan, and M. Xiao, Arbitrarily configurable nonlinear topological modes, Phys. Rev. Lett. **133**, 116602 (2024).

[80] K. Sone, M. Ezawa, Y. Ashida, N. Yoshioka, and T. Sagawa, Nonlinearity-induced topological phase transition characterized by the nonlinear Chern number, Nat. Phys. **20**, 1164 (2024).

[81] K. Sone and Y. Hatsugai, Topological-to-topological transition induced by on-site nonlinearity in a one-dimensional topological insulator, Phys. Rev. Res. **8**, L012045 (2026).

[82] W. Zhang, H. Yuan, H. Wang, F. Di, N. Sun, X. Zheng, H. Sun, and X. Zhang, Observation of Bloch oscillations dominated by effective anyonic particle statistics, Nat. Commun. **13**, 2392 (2022).

[83] T. Hofmann, T. Helbig, C. H. Lee, M. Greiter, and R. Thomale, Chiral voltage propagation and calibration in a topolectrical Chern circuit, Phys. Rev. Lett. **122**, 247702 (2019).

[84] W. Suh, Z. Wang, and S. Fan, Temporal coupled-mode theory and the presence of non-orthogonal modes in lossless multimode cavities, IEEE J. Quantum Electron. **40**, 1511 (2004).

[85] N. A. Olekhno, E. I. Kretov, A. A. Stepanenko, P. A. Ivanova, V. V. Yaroshenko, E. M. Puhtina, D. S. Filonov, B. Cappello, L. Matekovits, and M. A. Gorlach, Topological edge states of interacting photon pairs emulated in a topolectrical circuit, Nat. Commun. **11**, 1436 (2020).

[86] H. A. Gersch and G. C. Knollman, Quantum cell model for bosons, Phys. Rev. **129**, 959 (1963).

[87] L. Amico and V. Penna, Dynamical mean field theory of the Bose-Hubbard model, Phys. Rev. Lett. **80**, 2189 (1998).

[88] I. Bloch, J. Dalibard, and S. Nascimbène, Quantum simulations with ultracold quantum gases, Nat. Phys. **8**, 267 (2012).

[89] C. Chin, R. Grimm, P. Julienne, and E. Tiesinga, Feshbach resonances in ultracold gases, Rev. Mod. Phys. **82**, 1225 (2010).

[90] R. Li, B. Lv, H. Tao, J. Shi, Y. Chong, B. Zhang, and H. Chen, Ideal type-II Weyl points in topological circuits, Natl. Sci. Rev. **8**, nwaa192 (2021).

[91] G. Liu, J. Noh, J. Zhao, and G. Bahl, Self-induced Dirac boundary state and digitization in a nonlinear resonator chain, Phys. Rev. Lett. **129**, 135501 (2022).